EFFECTS OF ION IRRADIATION ON THE MECHANICAL PROPERTIES AND STRUCTURAL EVOLUTION OF SOL-GEL DERIVED HYBRID SILICATE THIN FILMS

By

YONGLI QI

Bachelor of Science
Tianjin University
Tianjin, China
2005

Master of Science
Tianjin University
Tianjin, China
2007

Submitted to the Faculty of the
Graduate College of the
Oklahoma State University
in partial fulfillment of
the requirements for
the Degree of
DOCTOR OF PHILOSOPHY
July, 2015

EFFECTS OF ION IRRADIATION ON THE MECHANICAL PROPERTIES AND STRUCTURAL EVOLUTION OF SOL-GEL DERIVED HYBRID SILICATE THIN FILMS

Thesis Approved:

Don A. Lucca

Dissertation Advisor

Daniel R. Grischkowsky

Prabhakar R. Pagilla

Matthew J. Klopfstein

ACKNOWLEDGMENTS

I would like to thank my adviser Prof. Don A. Lucca, a dedicated professor who devotes himself to seeking the nature of the science, for his encouragement, support and guidance. I would also like to thank my committee members, Prof. Daniel R. Grischkowsky, Prof. Prabhakar R. Pagilla and Prof. Matthew J. Klopfstein for their valuable comments and suggestions.

I extend my thanks to Dr. Andreas Mehner at Stiftung Institut für Werkstofftechnik (IWT) and Torsten Prenzel for their hard work to design and synthesize the thin films, to Dr. Yongqiang Wang at Los Alamos National Laboratory for his devoted time to perform the ion irradiation experiments and RBS/ERD measurements, and to Dr. Darrick Williams at Los Alamos National Laboratory for his efforts to perform XRD experiments and analyze the possible crystalline structures.

I would also like to thank my colleagues, Tres A. Harriman, Seyyed A. Shojaee, Arezoo Zare, Daniel S. Hildebrand, Kyle Ford, Golnaz Bassiri, and Benjamin Dvorak, for their help, comments and assistance.

The financial support by the National Science Foundation through Grant Nos. OISE-0352377 and OISE-0128050 is gratefully acknowledged. The funding for the Transregionaler Sonderforschungsbereich SFB/TR4 by the Deutsche Forschungsgemeinschaft is also gratefully acknowledged.

Finally, I would like to thank my family for their continuous support and encouragement.

Acknowledgments reflect the views of the author and are not endorsed by committee members or Oklahoma State University.

Name: Yongli Qi

Date of Degree: July, 2015

Title of Study: EFFECTS OF ION IRRADIATION ON THE MECHANICAL PROPERTIES AND STRUCTURAL EVOLUTION OF SOL-GEL DERIVED HYBRID SILICATE THIN FILMS

Major Field: Mechanical and Aerospace Engineering

Abstract:

A study of the effects of ion irradiation on the surface mechanical properties and structural evolution of sol-gel derived hybrid silicate thin films has been conducted. Green films were synthesized through a sol-gel process using tetraethoxysilane (TEOS) and methyltriethoxysilane (MTES) as precursors and acetic acid as a catalyst and spin-coated onto (100) Si wafers. Films were heat treated in ambient air or in vacuum at temperatures of 300 - 800 °C, or irradiated with 200 keV H^+, 400 keV N^{2+}, 1 MeV Cu^+, 4 MeV Cu^{2+} and 9 MeV Cu^{3+} with fluences of 1×10^{13} to 2×10^{17} ions/cm^2. The resultant films were investigated by atomic force microscopy (AFM), nanoindentation, Rutherford backscattering spectrometry (RBS), elastic recoil detection (ERD) and scanning electron microscopy (SEM).

In order to better understand the chemical structure of the green films, the theoretical chemical composition was obtained based on the starting materials and the chemical reactions during hydrolysis and condensation. The difference in the mechanical properties of the films heat treated in ambient air and in vacuum was attributed to the different thermal stability and decomposition path of the organic components in different environments, thus affecting the resulting microstructure.

Investigation of the film shrinkage and mechanical properties of the ion irradiated films led to a conclusion that the mechanical properties of the films had a noticeable increase when the films were irradiated at a fluence of 1×10^{14} ions/cm^2 or above. During irradiation, the majority of H was released and some O and C were also released, as evidenced by the decreasing H/Si, C/Si and O/Si ratios with increasing fluence. The Voigt and Reuss model was employed to evaluate the elastic modulus of the fully converted films by considering them as a composite. It was observed the reduced elastic modulus of the fully converted films after ion irradiation increased with increasing Si-C bond concentration, consistent with that of the silicon oxycarbide synthesized by heat treatment in Ar flow or by RF sputtering.

A plausible explanation of the structural evolution during ion irradiation was developed by analyzing the H/Si, O/Si, and C/Si ratios with increasing fluence, the difference in the stopping power, and the theoretical chemical composition of the green films. The possible schemes of forming CSi_4 were also discussed.

TABLE OF CONTENTS

LIST OF TABLES

LIST OF FIGURES

NOMENCLATURE

MTES	MethylTriEthoxySilane
TEOS	TetraEthOxySilane
PVP	PolyVinylPyrrolidone
SEM	Scanning Electron Microscopy
RBS	Rutherford Backscattering Spectrometry
ERD	Elastic Recoil Detection
XPS	X-ray Photoelectron Spectroscopy
AFM	Atomic Force Microscopy
XRD	X-ray Diffraction
SR350	methylhydroxylsioxae
SR355	phenylmethylhydroxylsioxane
PTES	phenyltriethoxysilane
HMDS	hexamethyldisilazane
PS	polysiloxanes
PCS	polycarbosilanes

Chapter 1

INTRODUCTION

1.1 Motivation

In 2001 the Transregional Collaborative Research Center SFB/TR4 Process Chains for the Replication of Complex Optical Components started a cooperative research project that involved a close collaboration between the University of Bremen, the Technical University of Aachen, and Oklahoma State University, with an overall goal of improving the accuracy of replicated complex optics while simultaneously reducing the number of required iterations and cost of the manufacturing process within the applied process chain. The focus of this joint research is the replication of complex high precision optical components (aspheric lenses, free-form lenses or lens arrays) in high volume at low cost. Well-developed direct machining technologies of these optics are expensive and time-consuming. In order to meet the demands of high quality complex-shaped optical components (i.e., camera lenses for mobile phones, lenses for DVD recorders, micro-lens arrays for LCD-displays and optical systems in automobiles), fully automated replication technologies for high volume production are essential and inevitable. These complex-shaped optical components are manufactured by injection molding of plastic. The traditional method for manufacturing such molds is multi-stage precision grinding and polishing of steel or nickel alloys [1]. High precision diamond machining is potentially much more efficient and economical than such a multi-stage process. However steel is not a desirable material for diamond machining because of the severe wear of the diamond tools, and other metallic materials (e.g., Cu or Al) lack of the needed hardness desired for optical molds. Thus, diamond turnable hard coatings with good adhesion are required.

Sol-gel derived hybrid films are a suitable material for replication molds. The incorporation of the selected organics (e.g., methyl groups) allows for lower sintering temperatures and better adhesion,

as well as reduced brittleness ensuring a good workability in the green state [2–4] and high hardness and wear resistance after conversion leading to a long lifetime for replicating optics. By selectively incorporating organic groups into an inorganic matrix, it is possible to preferentially modify the mechanical, optical and photonic properties of the materials in their final state.

The limiting factor of sol-gel derived films for optical mold applications is the critical thickness, which refers to the maximum crack-free thickness achievable after solvent evaporation in the sol-gel process [2]. Diamond machining requires films having a thickness of more than 5 μm for high machinability. Inorganic films like ZrO_2 have a critical thickness of less than 200 nm for a single layer and less than 2 μm for multi deposited layers [2, 5, 6]. Crack-free hybrid silicate films having a thickness of 5 μm for a single layer and up to 20 μm for multi layers have been synthesized at the Stiftung Institut für Werkstofftechnik (IWT) in Germany. These films have been successfully machined by diamond tools and used as molds for replication of complex optics.

The final ceramic state is achieved by either heat treatment or ion irradiation to increase hardness and wear resistance. Ion irradiation as an alternative to heat treatment has drawn considerable attention for converting these films from the green state to their ceramic state. [7–12]. Heat treatment of hybrid films usually leads to a pure SiO_2 phase with significant loss of carbon and hydrogen. Ion irradiation conserves carbon content and significantly reduces hydrogen [13–16], resulting in the formation of silicon oxycarbide. The presence of a high concentration of carbon makes it possible to create many novel secondary phases. In addition, synthesis of nanocrystalline phases using ion irradiation is also possible.

1.2 Objective

In a previous study [17], investigation focused on the effects of heat treatment and ion irradiation on acid catalyzed sol-gel derived hybrid silicate thin films. Films heat treated in ambient air at temperatures of 300 °C, 600 °C and 800 °C for 10 min exhibited an increase in hardness and reduced elastic modulus with increasing heat treatment temperature. The film heat treated at 800 °C had a hardness of 0.7 GPa and reduced elastic modulus of 10.0 GPa. By comparison, a film irradiated with 2 MeV He^+ ions at a fluence of 3×10^{15} ions/cm^2 exhibited a hardness of 1.9 GPa and reduced elastic modulus of 21.9 GPa. For the heat treated films, the atomic ratio of C/Si was seen to decrease from 1.25 for the green film to 0.1 for the film heat treated at the highest temperature. For the ion irradiated film, the atomic ratio of C/Si showed little change from that of the green film.

Ion irradiation was carried out on 600 nm thick films using 125 keV H^+ and 250 keV N^{2+} ions

with fluences ranging from 1×10^{14} to 5×10^{16} ions/cm^2 for H^+ and 1×10^{15} to 5×10^{16} ions/cm^2 for N^{2+}. The hardness and reduced elastic modulus was found to increase with increasing fluence for each ion species. At the highest fluence, the film irradiated with H^+ was found to exhibit a 4.5 fold increase in reduced elastic modulus (7.1 GPa to 32.1 GPa) with respect to the green film while the film irradiated with N^{2+} showed a 12 fold increase (7.1 GPa to 84.0 GPa).

Irradiation with 100 keV Si^+, O^+, and N^+ ions, in which Si^+ has similar electronic stopping power with O^+ and N^+ ions but different nuclear stopping power at the surface, was carried out on 3 μm thick films at a fluence of 3×10^{16} ions/cm^2. The projected range of the 100 keV Si^+, O^+, and N^+ ions was 260, 450, and 470 nm, respectively. Projected range less than the film thickness leads to partial irradiation of the films. Hardness and reduced elastic modulus of the films irradiated with 100 keV Si^+, O^+, and N^+ ions did not show any observable difference. It was argued that the electronic stopping is principally responsible for the film hardening while the role of nuclear stopping is minimal. However, due to the partial irradiation, determining the actual mechanical properties of the portion of the films that were irradiated is difficult, if not impossible.

Films irradiated with 115 keV H^+, 125 keV H^+, 115 keV He^+, 250 keV N^{2+} and 2 MeV Cu^{2+} exhibited significant differences in the measured hardness and reduced elastic modulus when similar electronic energy was deposited to the film. It was suggested that hardness is not simply related to the electronic energy deposited to the film, but also depends on the ion species.

Ion irradiation was also performed on films heat treated at 800 °C in ambient air using 250 keV N^{2+} with fluences from 1×10^{14} to 5×10^{16} ions/cm^2. It was found that the films heat treated at 800 °C had a higher hardness and reduced elastic modulus than the film heat treated at 300 °C when both films were irradiated at a fluence of 1×10^{15} ions/cm^2 or lower, and a similar hardness and reduced elastic modulus when irradiated at a fluence of 1×10^{16} ions/cm^2 or above. It was argued that C concentration had no influence on the maximum hardness achieved by ion irradiation. However, the reason the film irradiated with 250 keV N^{2+} at the highest fluence had a higher reduced elastic modulus than fused silica (84.0 GPa compared with 69.6 GPa) is unclear.

The current work presented here is a continuation of the previous study on the effect of heat treatment and ion irradiation on the mechanical properties, chemical composition, and structural evolution of the sol-gel derived hybrid silicate thin films. The objectives of this work are stated as follows.

1. Study the effects of heat treatment in ambient air and in vacuum on the mechanical properties, chemical composition, and the structural evolution.

Oxidization of the organic components in the film results in a similar structure as fused silica when heat treated in ambient air. When heat treated in vacuum or an inert atmosphere, the oxidization of the organic components is suppressed, and silicon oxycarbide (SiOC) glass could be produced through a pyrolysis process at temperatures above 800 °C. The mechanical properties of the films heat treated in ambient air and in vacuum were investigated. The chemical compositions of the films heat treated in vacuum as a function of heat treatment temperature were studied. The microstructure of the films heat treated in ambient air were also investigated.

2. Study the effects of ion irradiation on the mechanical properties, chemical composition, and the structural evolution.

   In the previous study, the films were irradiated with 125 keV H^+ with fluences ranging from 1×10^{14} to 5×10^{16} ions/cm^2 or 250 keV N^{2+} with fluences ranging from 1×10^{15} to 5×10^{16} ions/cm^2. The electronic stopping of 125 keV H^+ and 250 keV N^{2+} is dominant in the energy loss process, while the nuclear stopping is negligible. In order to study the effect of nuclear stopping, 1 MeV Cu^+, which has a comparable electronic and nuclear stopping power, was used in the current study. Other ions used in the current study include 200 keV H^+, 400 keV N^{2+}, 4 MeV Cu^{2+}, and 9 MeV Cu^{3+}. The projected range of all ions used in the current study is larger than the film thickness so that full irradiation is achieved.

   One remaining question in the previous study was what minimum fluence resulted in measurable change of the mechanical properties, film shrinkage and H loss. The minimum fluence used for all ion irradiations in the current study was 1×10^{13} ions/cm^2, one order of magnitude lower than that in the previous study.

   The mechanical properties and film shrinkage of the ion irradiated films were investigated and compared with the results of the previous study. Chemical composition of the irradiated films was also investigated and correlated with the change in the microstructure and the mechanical properties. The origin of the ion irradiated films having a higher reduced elastic modulus than fused silica was studied. The significance of the electronic and nuclear stopping in the mechanical properties was also compared.

3. Study the effects of the types of the sol-gel system on the mechanical properties, film shrinkage and H loss under heat treatment or ion irradiation.

   In addition to the acid catalyzed films, base catalyzed films were also investigated in the

current study. Base catalyzed films heat treated at 300 - 800 °C were compared with the acid catalyzed films from the point of the view of film shrinkage, hardness and reduced elastic modulus. Base catalyzed films irradiated with 125 keV H^+ and 250 keV N^{2+} were also studied and compared with that of the acid catalyzed films irradiated with the same ions species in the previous study.

Chapter 2

BACKGROUND

2.1 Hybrid Silica Based Sol-gel Films

Organic/inorganic silica films are synthesized through a so-called sol-gel process in which silicon alkoxides undergo hydrolysis and condensation resulting in a three dimension interconnected network. The basic concept of the sol-gel process is described as follows.

In the sol-gel process, the precursors for preparing a sol consist of a metal or metalloid surrounded by various organic or inorganic ligands. Metal or metalloid alkoxides that consist of a metal or metalloid atom surrounded by alkoxy ligands are the most widely used precursors in sol-gel research. The first metal alkoxide was prepared from $SiCl_4$ and alcohol by Ebelmen in the 1840s and was used to prepare oxide films using the sol-gel process in the 1930s [18–20]. Once the metal or metalloid alkoxides are mixed with water, hydrolysis occurs resulting in the replacement of a ligand with a hydroxyl group (-OH). These alkoxides may be partially or completely hydrolyzed depending on the concentration of water and the characteristics of the catalysts [18]. Hydrolysis and condensation reactions are not separated in time but take place simultaneously [19]. In a condensation reaction, partially hydrolyzed molecules link together by liberating water or alcohol molecules. Figures 2.1 and 2.2 show the chemical reactions of hydrolysis and condensation by using tetraethoxysilane (TEOS) as a starting precursor, respectively.

Monomers that are capable of forming at least two bonds could lead to a macromolecule by continuous condensation. If one molecule reaches macroscopic dimension so that it extends throughout the solution, it is called a gel [18]. Thus a gel is a substance that contains a continuous solid skeleton enclosing a continuous liquid phase. In the gelation process, the viscosity increases dramatically. The sol can be deposited onto the substrate when an appropriate viscosity is reached. The solvent is

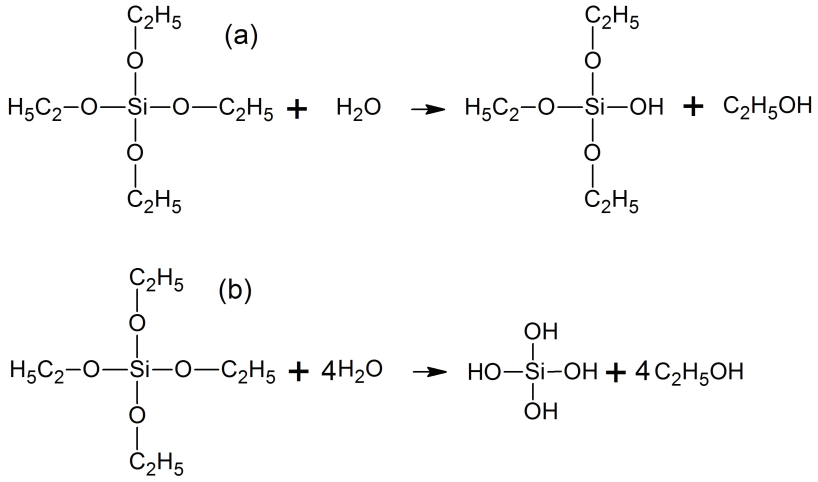

Figure 2.1: A schematic of partial (a) and complete (b) hydrolysis of TEOS.

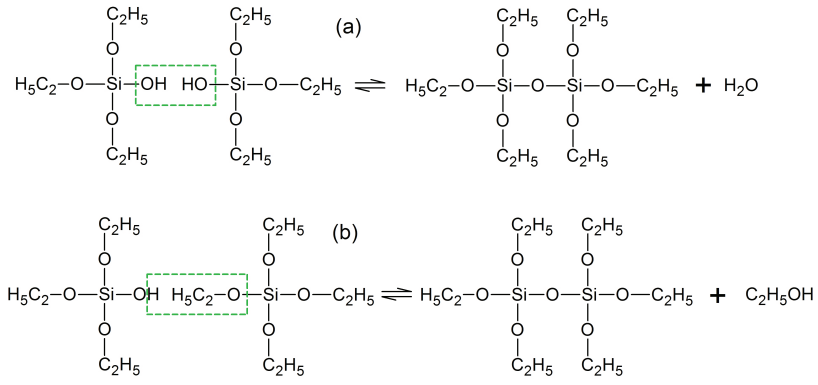

Figure 2.2: A schematic of water condensation (a) and alcohol condensation (b).

then removed by a drying process which takes place in several stages. The first stage is the constant rate period when the body shrinks by a volume equal to the volume of liquid that evaporates and the liquid-vapor interface remains at the exterior surface of the body. As liquid evaporates solid-liquid interfaces are replaced with solid-vapor interfaces gradually leading to an increase of the system energy. The main driving force of shrinkage of a silicate sol is the capillary force arising from the difference between the solid-vapor and solid-liquid interfacial energies. The critical point is the end of the first stage when the body becomes too stiff to shrink and the evaporation rate decreases. Due to the low permeability of the gel network, the tension of the liquid is greater near the drying surface, which produces differential shrinkage rate leading to cracking. Cracking mostly occurs at the critical point as the tension in the liquid reaches its maximum value [21]. It is observed that inorganic films with a thickness of less than 0.5 μm do not crack regardless of the drying rate whereas films thicker than 1 μm are mostly cracked [22–24]. Thicker crack-free films have been successfully produced by adding inactive organics to provide extra compliance [18, 21]. In the following stage, the falling rate period, liquid recedes into the interior, the rate of evaporation decreases and almost no shrinkage of the gel network occurs. Evaporation continues from the exterior of the body until liquid becomes isolated and evaporation can only take place within the body and vapor diffuses to the outside. Heat treatment at elevated temperature or ion irradiation are used to eliminate the residual organics and to increase the mechanical properties.

Incorporating inactive organic components into precursors has been proved to provide sufficient compliance for the production of crack-free films with a thickness up to 20 μm using the sol-gel process [6]. Methyltriethoxysilane (MTES, the product of replacing an ethoxy group in TEOS with a methyl group) is commonly used as inactive organic components donor to absorb the stress and provide more compliance. The alkyl groups (i.e., methyl), which are inactive in hydrolysis and condensation reactions, could also potentially increase the stability of positively charged transition state, leading to increased hydrolysis reaction [25] and alter the particle size during condensation [26].

Another approach to increase the compliance of the sol is directly adding inactive organic chemicals into the precursor solution. Polyvinylpyrrolidone (PVP), a water-soluble macromolecular compound, can be hybridized with polymers through strong hydrogen bonding between the C=O groups, present in PVP, and the OH groups in the polymers [27, 28]. It works as a binder providing more compliance and absorbing the generated stress during heat treatment thus thick crack-free films could be created [29–32].

Using precursors containing inactive organic components in the sol-gel process also has the potential of preferentially tailoring the resulting mechanical, optical and photonic properties in their

final state through the use of selected organic components. Good machinability in the green state and increased mechanical properties after ceramic conversion make hybrid silica films an appropriate candidate as molds for replication of plastic complex optics.

A literature review on the structural evolution under heat treatment and ion irradiation, the mechanical properties of the sol-gel derived hybrid silica and silicon oxycarbide, and the applications of sol-gel derived hybrid silica is reported below.

2.2 Structural Evolution of Sol-gel Derived Hybrid Silica Under Heat Treatment

Structural evolution of an amorphous gel under heat treatment is accompanied by shrinkage and weight loss. The shrinkage process consists of three stages that are defined by the weight loss behavior. In stage I, a small amount of shrinkage is accompanied by large weight loss which is the result of desorption of physically adsorbed water or residual solvent. In stage II, significant shrinkage and weight loss are primarily due to the removal of organics (principally weight loss), polymerization (shrinkage proportional to weight loss), and structural relaxation (shrinkage only). In stage III, only structural relaxation associated with densification by viscous flow occurs with no associated weight loss. Excess free volume is removed through diffusive motion of the network leading to a denser network.

As a consequence of incomplete hydrolysis of TEOS/MTES precursors and reversible condensation in the sol-gel process, some organic groups, such as methyl groups (-CH_3), residual ethoxyl (-O-CH_2CH_3) and hydroxyl groups (-OH) still remain in the gel. During heat treatment in air, most organic components are oxidized resulting in the carbon content being significantly lost. When heat treated in a vacuum or an inert gas atmosphere, pyrolysis of the organic components is processed through a different path where oxidization of the organic component is suppressed such that carbon is partially reserved and preparation of silicon oxycarbide could be achieved.

2.2.1 Thermal Stability of Sol-gel Derived Hybrid Silica

Remaining mutual solvent (ethanol) and water are evaporated during the heat treatment. Desorption of physically absorbed water (hydrogen bonded water) occurs between 150 °C and 200 °C [19]. Most ethoxyl groups bonded with Si react with water during hydrolysis resulting in the formation of ethanol (CH_3CH_2OH) which evaporates in the following drying process, while unhydrolyzed ethoxyl

groups remain stable up to around 250 °C and are then oxidized [33, 34]. Methyl groups in MTES are not affected by hydrolysis and could be oxidized at 350 - 450 °C and completely disappear after heat treatment at 500 - 600 °C [33, 35–37]. Silanol groups (Si-OH) are condensed starting at about 170 °C leading to dehydration [38]. The dehydration is reversible up to 400 °C and irreversible above 400 °C. After heat treatment above 800 °C only isolated hydroxyl groups remain on the surface [37], resulting in a similar structure to fused silica. Silica based sol-gel films retain an amorphous structure up to 1350 °C [39].

Pure PVP starts to decompose at about 380 °C [40] and degrades to amorphous carbon at ∼450 °C in vacuum or an inert atmosphere [41]. Under O_2 flow it may completely disappear through pyrolysis at about 500 °C [32]. Partial decomposition of PVP and formation of carbonaceous residue may start as low temperature as ∼230 °C in a gel [41, 42].

When heat treated in vacuum or an inert atmosphere, the oxidization of organic components is suppressed. Pyrolysis of ethoxyl groups starts at about 400 °C and result in the formation of hydrocarbons which might be the source of carbide or free carbon phase in the network. Pyrolytic cleavage of Si-CH_3 takes place around 700 °C by thermal cracking, instead of 500 °C by oxidation in air. Si-C bonds could be formed through condensation of two Si-CH_3 groups leading to a SiOC network. SiOC is not thermodynamically stable thus a mixture of stable phases, such as silicon carbide, amorphous carbon and silica can be formed instead during the heat treatment [7, 8].

2.2.2 Microstructures of Sol-gel Derived Silicon Oxycarbide Material

Silicon oxycarbide (SiOC) glass can be produced from preceramic silicone polymers that are formed through the sol-gel process using silicon based alkoxides as precursors. A desired ceramic can be converted from the preceramic polymers through a pyrolysis process in vacuum or an inert atmosphere at temperatures above 800 °C. The structure of the SiOC glass after pyrolysis at 800 - 1000 °C can be described as $SiC_xO_{2(1-x)}$ + yC_{free} [43, 44], where $SiC_xO_{2(1-x)}$ represents the stoichiometric silicon oxycarbide network and C_{free} is the excess free carbon. The formation of free carbon starts even as low as 600 °C through the redistribution of Si-O and Si-C bonds [45, 46]. An evidence is that the pyrolyzed material shows a coloration from transparency to brown after heat treated at 615 °C [46]. The free carbon contents of silicon oxycarbide glass derived from hydrolysis and condensation of alkoxide highly depends on the nature of the inactive side groups of the precursors: alkyl groups leading to moderate content of free carbon, unsaturated groups (vinyl, phenyl) leading to high content of free carbon [43]. In order to minimize the free carbon content,

replacing the side groups with H atoms practically creates oxycarbide with no free carbon phase [45].

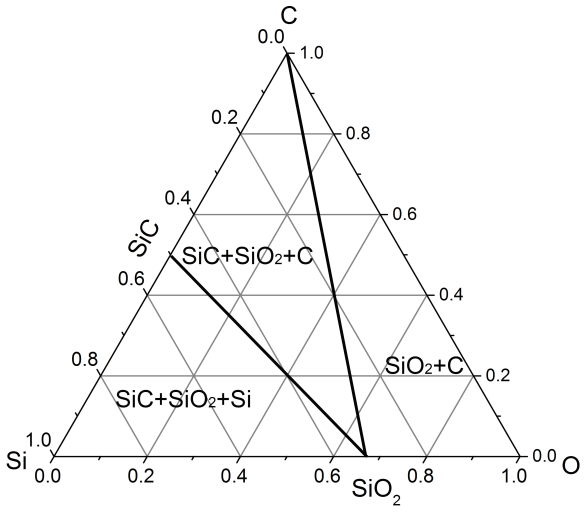

Figure 2.3: A schematic of possible phases after phase separation of silicon oxycarbide modified from [47].

Phase separation starts at ∼1200 °C, leading to the precipitation of nanosized crystalline SiC and graphitic carbon cluster embedded in an amorphous matrix [43,47–56]. A schematic of a silicon oxycarbide ternary phase diagram is shown in Fig. 2.3 representing all possible phases after phase separation based on the chemical composition [47]. At above 1300 °C, the number of Si-C bonds were observed to increase with a corresponding decrease of Si-O bonds, suggesting a carbothermal reduction of SiO_2 between the matrix and the free carbon resulting in the formation of SiC and volatile species through [43, 50, 57]:

$$SiO_2(s) + 3C(s) \rightarrow SiC(s) + 2CO(g) \tag{2.1}$$

Cristobalite, which usually forms at a temperature of ∼1200 °C, was not observed when the silicon oxycarbide materials were pyrolyzed at 1200 to 1400°C [55]. The excess free carbon is considered to inhibit the nucleation of cristobalite as the short-range diffusion is strongly impeded by the excess free carbon in the amorphous SiOC network. In contrast, pyrolysis in air which oxidizes the free carbon promotes the nucleation and growth of cristobalite. At 1400 °C, despite the fact numerous precipitations of SiC, there still exists a high amount of amorphous silicon oxycarbide. For Si-rich oxycarbide, the phase separation starts at a temperature ∼1000 °C with precipitation of crystalline silicon nanodomains, besides the formation of SiC and SiO_2 [44,55]. At above 1400 °C, generation of bubbles is a result of the interaction between the nanodomains of silica and silicon forming gaseous

SiO through [44]:

$$SiO_2(s) + Si(s) \rightarrow 2SiO(g) \tag{2.2}$$

2.3 Ion Irradiation of Sol-gel Derived Hybrid Silica

Ion irradiation is an alternative method to convert green state sol-gel films into their ceramic state. One of its major advantages in converting sol-gel films is the selective release of hydrogen while retaining carbon [58–60]. This is in contrast to traditional heat treatment which affects the entire organic components [35,61]. The resulting excess carbon is essential for the formation of nanophases, such as SiC and amorphous carbon.

Pivin's research group has investigated a variety of polymers derived from TEOS, MTES, triethoxysilan (TH), and polycarbosilan (PCS). These polymers were irradiated with He, C, Si, Cu, Au, Ag and Xe with different energies (200 keV - 3 MeV) at fluences of 1×10^{14} - 5×10^{16} ions/cm^2) [7,8]. Together with H release, a large portion of the carbon atoms segregate into clusters after ion irradiation forming diamond-like carbon clusters which could be the reason for higher hardness than that of conventionally heat treated specimens. Carbon also segregates in films heat treated in vacuum, but shows a lower degree of sp^3 hybridization than in irradiated films. The nature of cross-linking due to ion irradiation is completely different from heat treatment in air which occurs at thermodynamic equilibrium.

Regarding the origin of the selective H release and the formation of carbon clusters, electronic energy transfer by excitation and ionization of the target electron has been considered the primary cause for the conversion of green state sol-gel derived silica films. Nuclear energy transfer by direct atomic collisions with the target atoms may affect the conversion when heavy ions are used. Irradiation of methylhydroxylsiloxane (SR350) with 3 MeV Au shows a relative softening, (i.e., the measured hardness levels off at high fluences), compared to 500 keV C irradiation which causes a continuous increase in hardness with increasing fluence [7,8,62]. It is noted here that for irradiation of SR350, the electronic and nuclear stopping powers are 355 and 230 eV·cm^2/10^{15} atoms for Au, and 64 and 1.7 eV·cm^2/10^{15} atoms for C.

2.4 Mechanical Properties of Sol-gel Derived Hybrid Silica and Silicon Oxycarbide

The mechanical properties of hybrid sol-gel based silica have been widely reported. However the mechanical properties are highly affected by the sol-gel process (such as the type of precursors, type of catalyst, and the amount of water) and the condition of heat treatment or ion irradiation.

Yu et al. [63, 64] investigated the mechanical properties of hybrid silica films synthesized by mixing acid catalyzed TEOS sol with base catalyzed MTES sol. The films were surface-modified by 10% HMDS-toluene to replace residual surface silanol groups with methyl groups and then heat treated in air up to 450 °C. When the molar ratio of TEOS/MTES was decreased from 2.0 to 0.25, the porosity was observed to increase from 53% to 73% and hardness and reduced elastic modulus measured using a Berkovich diamond indenter decreased from 1.24 to 0.35 GPa and from 8.5 to 2.6 GPa, respectively. In spite of the ratio of TEOS/MTES, all films showed increased hardness and elastic modulus with increasing heat treatment temperature before cracks were observed [65, 66]. The increase in hardness and elastic modulus was attributed to the removal of the absorbed water, organic components and hydroxyl groups which eventually led to a denser Si-O-Si network.

Silicon oxycarbide pyrolyzed at 1000 °C in Ar from preceramic polymer through sol-gel process was determined to have an elastic modulus of 57 to 110 GPa and a hardness of 4.7 to 8.9 GPa, depending on the chemical composition [44, 67], from a 3-point bending test. After pyrolysis at 1200 °C, the elastic modulus and hardness were measured to be 82 to 113 GPa and 6.6 to 9.3 GPa, respectively. In general, the mechanical properties increase from low-carbon silicon oxycarbide to carbon-rich silicon oxycarbide.

Pivin's research group [7, 8, 68–72] has investigated the mechanical properties of various types of PS (polysiloxane), which is the general term for organic polymers containing a -Si-O-Si backbone, subjected to various ion irradiations. SiOC coatings obtained from methylhydroxylsiloxane (SR350), phenylmethylhydroxylsioxane (SR355) silicone resins and phenyltriethoxysilane (PTES) alkoxide solution show various hardness ranging from 15 GPa to 21 GPa under He, C and Au irradiation at maximum achievable fluence (5×10^{16} for He, 1×10^{16} for C and 1×10^{15} for Au).

2.5 Applications of Sol-gel Derived Hybrid Silica Materials

Hybrid sol-gel derived silica has been used for mechanical, optical and electrical applications. Such films have been used as metal corrosion inhibitors [73–76], abrasion resistance coatings on plastic

substrates [77–79] and as electrochemical biosensors [80–82]. Hybrid silica material could also be used in the production of monolithic columns which have been widely applied in capillary liquid chromatography separation, as well as sample pretreatment of solid-phase microextraction and immobilized enzyme reactors [83, 84]. Due to their high machinability in the green state, hybrid silica films were used as a mold coating for the replication of complex optical plastic components.

Regarding optical applications, hybrid sol-gel materials have been used as a host matrix for organic laser dyes [85, 86]. These hybrid solid state dye lasers exhibit lower threshold powers for laser action, laser slope efficiency close to theoretical values, long laser lifetimes, and could operate at much higher repetition rates than other polymer hosts.

Hybrid silica can be used a low dielectric constant material to replace the common used insulator material SiO_2 in semiconductor applications [87–89].

Chapter 3

EXPERIMENTAL APPROACH

3.1 Sol-gel Film Preparation

Sol-gel derived silica films from precursors TEOS/MTES were prepared at the Stiftung Institut für Werkstofftechnik (IWT) in Bremen, Germany. The chemicals used in the sol-gel process are presented in Table 3.1. Acetic acid (CH_3COOH) and sodium hydroxide (NaOH) were used as catalysts to increase the hydrolysis reactions, leading to two types of sol-gel films. The molecular structures of TEOS, MTES, and PVP are shown in Appendix A.

Table 3.1: Sol composition

Solution	TEOS (mol)	MTES (mol)	CH_3COOH (mol)	NaOH (mol)	H_2O (mol)	PVP (mol)	C_2H_5OH (mol)	Thickness (μm)
Acid catalyzed (EtOH/Si = 5)	0.4	0.6	4	-	1	0.25	5	$\leq$3.5
Acid catalyzed (EtOH/Si = 7.5)	0.4	0.6	1	-	1	0.25	7.5	$\leq$1
Base catalyzed	1	4	-	0.96	5.66	-	1	$\leq$4
Base catalyzed (ethanol diluted)	Base catalyzed sol diluted with ethanol 1:1 in Ar before deposition							$\leq$1

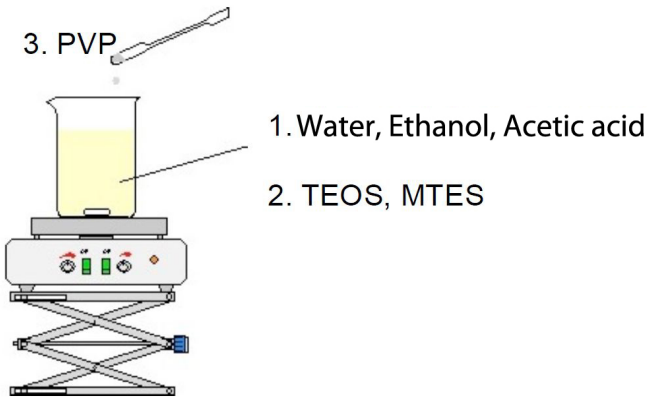

Figure 3.1: A schematic of the preparation of CH_3COOH-catalyzed sol [90].

3.1.1 Acid Catalyzed Sol

The acid catalyzed sol was synthesized starting from a solution of ethanol, diluted water and acetic acid in a beaker. A mixture of 0.4 mol TEOS and 0.6 mol MTES was then added drop by drop to the starting solution under vigorous stirring as shown in Figure 3.1. The resulting solution was stirred for 10 min before adding 0.25 mol PVP (polyvinylpyrrolidone) $(C_6H_9NO)_n$, after which the beaker was sealed to prevent evaporation of the ethanol and the solution was heated above 50 °C for 30 minutes. After cooling, the sol was stored in a glass bottle in an Ar atmosphere for 24 hours to achieve the proper viscosity before deposition. A schematic of the process is shown in Fig. 3.1.

3.1.2 Base Catalyzed Sol

The base catalyzed sol was prepared by dissolving NaOH in a solution of TEOS and MTES in a three-neck flask and stirring the solution for 24 hours in an Ar atmosphere. Then a mixture of water and ethanol was added drop by drop while keeping the solution temperature below 35 °C using a water bath. The sol was kept in an Ar atmosphere for 24 hours before deposition. A schematic of base catalyzed sol preparation is presented in Fig. 3.2.

3.1.3 Sol-gel Film Deposition

The solution was deposited by spin coating onto polished 50 mm diameter (100) Si wafers. After the films were allowed to dry at 80 °C for at least 10 minutes, the acid and base catalyzed films were heat treated in a pre-heated furnace at a temperature of 300 °C for 10 and 30 minutes, respectively.

The film thickness was initially estimated by ball grinding experiments performed at the IWT and later measured by a step-height technique using atomic force microscopy (AFM) at Oklahoma

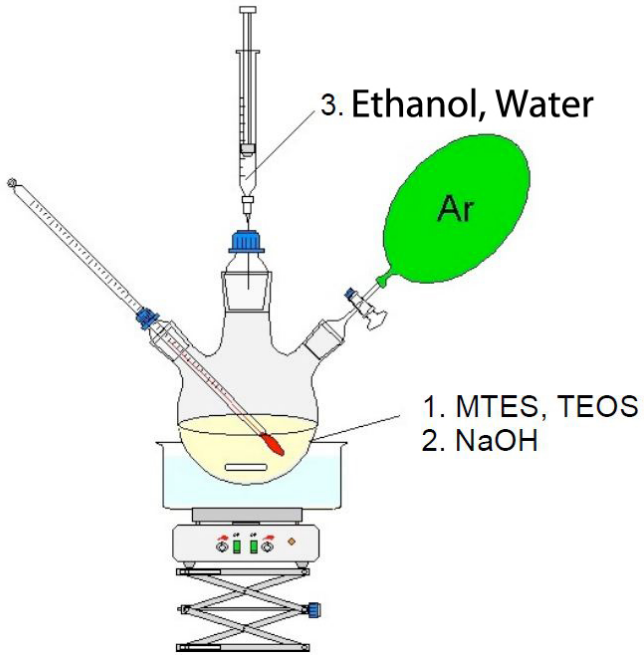

Figure 3.2: A schematic of the preparation of NaOH-catalyzed sol [90].

State University. For the acid catalyzed sol (EtOH/Si = 7.5), deposition at rotational speeds of 1000, 1500 and 2500 rpm resulted in a nominal film thickness of about 1000, 800 and 600 nm, respectively. A crack-free film with thickness up to 3.5 μm was obtained by depositing acid catalyzed sol (EtOH/Si = 5) at 1000 rpm. Base catalyzed film could have a thickness up to 4 μm by depositing base catalyzed sol at 1000 rpm and have a thickness of 1 μm by depositing diluted sol at 1500 rpm. Using the measured film thickness, the area of the film, and the measured weight gain after coating, the film density was estimated to be 1.3 g/cm^3 for both acid and base catalyzed films.

3.2 Film Modification

3.2.1 Heat Treatment

Acid catalyzed films having a thickness of 1 μm were heat treated at 300 - 800 °C in ambient air for 10 min or in vacuum for 30 min. 3 μm thick acid catalyzed films were also heat treated at 300 - 800 °C in ambient air for 10 min. Also 1 μm thick base catalyzed films produced from the diluted sol were heat treated at 300 - 800 °C in ambient air for 30 min. More details about the conditions of heat treatment are shown in Table 3.2. All heat treatments were performed at the IWT in Germany.

Table 3.2: Heat treatment conditions

Film	Heat Treatment Conditions
Acid catalyzed 3-μm thick	300 - 800 °C in air 10 min
Acid catalyzed 1-μm thick	300 - 800 °C in air 10 min
Acid catalyzed 1-μm thick	300 - 800 °C in vacuum 30 min
Base catalyzed 1-μm thick	300 - 800 °C in air 30 min

3.2.2 Ion Irradiation

Ion irradiation, as an alternative method to heat treatment, was used to convert the deposited sol into a ceramic state. As an energetic ion traverses a solid, it undergoes a series of collisions with the stationary target atoms, which deflect the ion from its initial trajectory, and with target electrons in the solid, which lead to electron excitation and ionization. As a result of nuclear and electronic collisions, the incident ions lose energy and eventually stop. The energy loss rate per travel distance ($\frac{dE}{dx}$) can be expressed as the summation of nuclear stopping power ($\frac{dE}{dx}\big|_n$) and electronic stopping power ($\frac{dE}{dx}\big|_e$):

$$\frac{dE}{dx} = \frac{dE}{dx}\bigg|_n + \frac{dE}{dx}\bigg|_e \tag{3.1}$$

where the subscripts n and e refer to nuclear and electronic stopping.

Nuclear collisions usually involve large energy transfer and significant angular deflection of an ion trajectory leading to the production of lattice disorder as shown in Fig. 3.3. Electronic collisions involve much smaller energy loss per collision, negligible deflection of the ion trajectory and negligible lattice disorder. However the importance of the two energy loss mechanisms varies with the energy (E) and atomic number (Z) of the incident ion. In general, electronic stopping dominates for high E and low Z while nuclear stopping takes over for low E and high Z.

In the area of ion irradiation, the projected range (R_p) is of great interest which is the projection of the travel distance normal to the surface of the target. In this study, proper ions were chosen such that the projected range calculated using SRIM [91] is larger than the film thickness.

Experimental

Individual specimens were cleaved approximately 8 mm × 8 mm or 25 mm × 25 mm in size from the 50 mm wafer for ion irradiation. Ion irradiation was carried out at room temperature with 200 keV

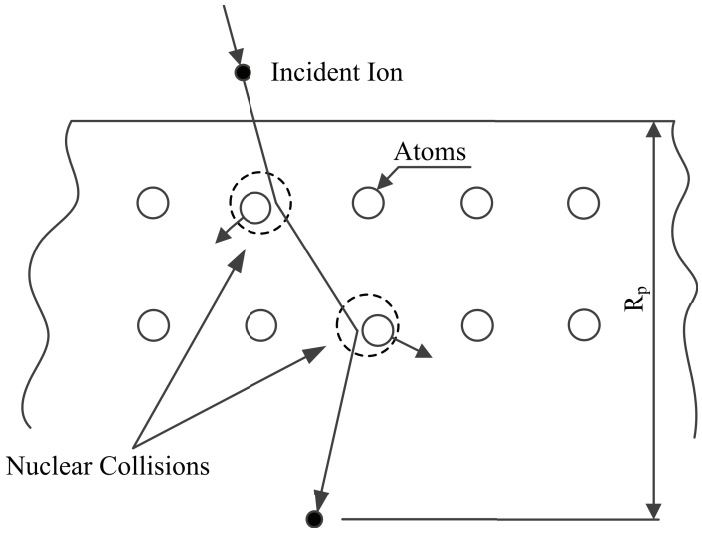

Figure 3.3: A schematic of nuclear collisions which deflect the trajectory of the incident ion.

H^+, 400 keV N^{2+}, 1 MeV Cu^+, 4 MeV Cu^{2+} and 9 MeV Cu^{3+} at fluences from 1×10^{13} up to 2×10^{17} ions/cm^2 of the acid catalyzed films with a nominal thickness of 1 μm. The base catalyzed films were irradiated with 125 keV H^+ and 250 keV N^{2+} ions at fluences ranging from 1×10^{14} to 1×10^{17} ions/cm^2. In a previous investigation of the acid catalyzed films by [17], the irradiations were performed using 125 keV H^+ and 250 keV N^{2+} ions at fluences ranging from 1×10^{14} to 1×10^{17} ions/cm^2. The detailed conditions of ion irradiation of the acid and base catalyzed films are presented in Table 3.3. The beam current was less than 0.5 μA/cm^2 for all irradiations in order to avoid the thermal effects arising from the ion irradiation.

Ion irradiation was carried out using a 200 kV Danfysik ion implanter for the H and N irradiations and a 3 MV tandem ion accelerator for the Cu irradiations at Los Alamos National Laboratory.

3.2.3 Secondary Heat Treatment

In an attempt to investigate the possibility of synthesizing nanostructures by ion irradiation, a secondary heat treatment at 1000 °C or 1350 °C in Ar for 2 hrs. after ion irradiation was performed on the base catalyzed films irradiated with 125 keV H^+ and 250 keV N^{2+} at fluences of 1×10^{15} and 1×10^{16} ions/cm^2, as well as on unirradiated acid and base catalyzed films for comparison. Details about the conditions of the secondary heat treatment are shown in Table 3.4.

Table 3.3: Ion irradiation conditions

Film	Ion	Fluence (10^{15} ions/cm^2)
Acid catalyzed 1-μm thick	200 keV H^+	0.01 - 200
	400 keV N^{2+}	0.01 - 5
	1 MeV Cu^{1+}	0.01 - 10
	4 MeV Cu^{2+}	0.01 - 10
	9 MeV Cu^{3+}	0.01 - 10
Base catalyzed 1-μm thick	125 keV H^+	0.1 - 15
	250 keV N^{2+}	0.1 - 10
Acid catalyzed 600-nm thick [17]	125 keV H^+	0.1 - 100
	250 keV N^{2+}	0.1 - 50

Table 3.4: Secondary heat treatment conditions

Type of sol-gel film	Ion irradiation condition	2nd heat treatment condition
Acid catalyzed	Unirradiated	1000 °C 2 hrs.
Base catalyzed	Unirradiated	1000 °C 2 hrs.
	125 keV H^+ 10^{15} ions/cm^2	1000 °C 2 hrs.
	125 keV H^+ 10^{16} ions/cm^2	1000 °C 2 hrs.
	250 keV N^{2+} 10^{15} ions/cm^2	1000 °C 2 hrs.
	250 keV N^{2+} 10^{16} ions/cm^2	1000 °C 2 hrs.
Acid catalyzed	Unirradiated	1350 °C 2 hrs.
Base catalyzed	Unirradiated	1350 °C 2 hrs.
	125 keV H^+ 10^{15} ions/cm^2	1350 °C 2 hrs.
	125 keV H^+ 10^{16} ions/cm^2	1350 °C 2 hrs.
	250 keV N^{2+} 10^{15} ions/cm^2	1350 °C 2 hrs.
	250 keV N^{2+} 10^{16} ions/cm^2	1350 °C 2 hrs.

3.3 Characterization Techniques

The investigations of this study involve measurements of the mechanical properties and identification and characterization of the chemical compositions and structural evolutions by utilizing the following techniques: atomic force microscopy (AFM) to investigate the surface topography and to measure the surface roughness and film thickness, nanoindentation to determine the mechanical properties, Rutherford backscattering spectrometry (RBS) and elastic recoil detection (ERD) to identify the chemical composition and to analyze the bulk density, X-ray diffraction (XRD) to detect any possible nanocrystalline phases, scanning electron microscopy (SEM) to study the surface structure and possible porosity.

3.3.1 Nanoindentation

Depth-sensing nanoindentation has become the standard technique used for nanomechanical characterization of materials. During nanoindentation, a force is applied by the transducer and the resulting displacement is recorded simultaneously to produce a force versus displacement curve which provides information on the elastic modulus and hardness [92–98], strain-hardening [99, 100], cracking [101, 102], phase transformation [103, 104] and creep behaviors [105–107]. The most common use of nanoindentation tests is to extract mechanical properties, i.e., elastic modulus and hardness, from the loading [108] or unloading [93, 109, 110] portion of the force-displacement curve. Unlike conventional indentation hardness measurements in which the residual plastic impression in the specimen is imaged as a function of applied load, the analysis method proposed by Oliver and Pharr [92, 93, 111] in 1992 for measuring hardness and elastic modulus by instrumented indentation techniques has been widely accepted and used in nanoscale mechanical behavior characterization. In this method, the projected contact area is evaluated using the equations for the elastic contact of an indenter of known geometry on a uniform and isotropic half space [93]. Thus the calculation of elastic modulus and hardness can be done without the necessity of imaging the indentation residual impression after the indentation.

Investigations in the early 1970s by Bulychev, Alekhin, Shorshorov, and co-works on the measurements of elastic modulus through indentation load-displacement data showed the elastic modulus could be related to the contact stiffness through equation [111, 112]:

$$S = \frac{dP}{dh} = \frac{2}{\sqrt{\pi}} E_m \sqrt{A} \tag{3.2}$$

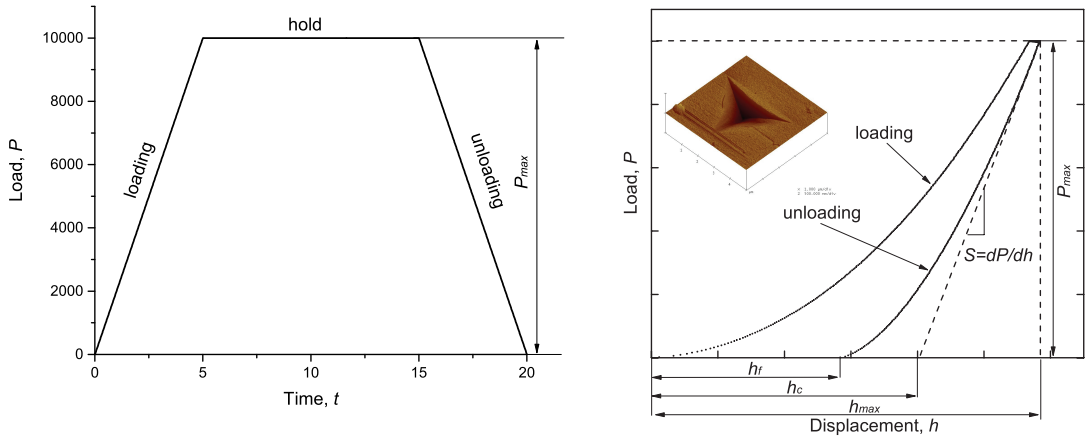

Figure 3.4: A typical loading function and recorded load-displacement curve showing: the maximum load, $P_{\max}$, the contact depth, h_c, the final depth, h_f, and the measured stiffness, S. An inset showing an indentation impression after load removal imaged by atomic force microscopy.

where $S = dP/dh$ is the experimentally measured stiffness determined from the slope of the initial portion of the unloading data as shown in Figure 3.4, A is the projected area of elastic contact, and E_m is the elastic modulus. If the indenter is non-rigid, the reduced elastic modulus, E_r, should be used to replace E_m in Eq. 3.2 with E_r defined as

$$\frac{1}{E_r} = \frac{\left(1-\nu^2\right)}{E} + \frac{\left(1-\nu_i^2\right)}{E_i} \tag{3.3}$$

where E and ν are the elastic modulus and Poisson's ratio for the specimen and E_i and ν_i are the same parameters for the indenter. Thus the reduced elastic modulus, E_r, is determined from:

$$E_r = \frac{\sqrt{\pi}}{2}\frac{S}{\sqrt{A}} \tag{3.4}$$

The projected contact area, A, could be related to a function of contact depth, $f(h_c)$, for an indenter with known geometry. A general form of the projected area function proposed by Oliver and Pharr [93] is

$$A = C_0 h_c^2 + C_1 h_c + C_2 h_c^{1/2} + C_3 h_c^{1/4} + C_4 h_c^{1/8} + ... + C_8 h_c^{1/128} \tag{3.5}$$

where $C_0, C_2, \cdots, C_8$ are constants obtained from the indenter area function calibration. Figure 3.5 shows a cross section of an indentation representing the contact profiles under load and after load removal and the parameters used in the analysis. The contact depth at peak load, h_c, is written as

$$h_c = h_{max} - h_s \tag{3.6}$$

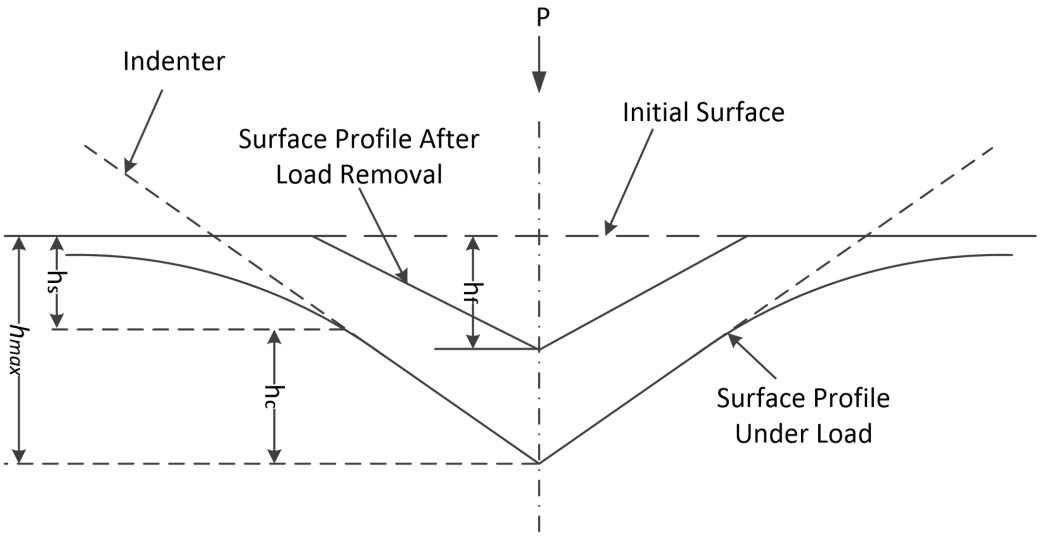

Figure 3.5: A schematic representation of a cross section through an indentation showing: contact profile under load and after load removal, the maximum depth under load, h_{max}, the contact depth, h_c, the final depth, h_f. (Figure recreated based on [93])

where h_{max} is the maximum depth at peak load and h_s is the elastic deflection of the surface at the perimeter of the contact. The elastic deflection of the surface depends on the indenter geometry through equation:

$$h_s = \epsilon \frac{P_{max}}{S} \tag{3.7}$$

where ϵ is a geometric constant, and equals 0.72 for a conical indenter, 0.75 for a paraboloid of revolution, and 1 for a flat punch.

In addition to the elastic modulus, the indentation hardness, a measure of resistance to plastic deformation, is defined as the mean pressure at peak load,

$$H = \frac{P_{max}}{A} \tag{3.8}$$

where A is the projected area of contact at peak load, P_{max}.

Calibration of the load frame compliance

When a load is applied to the indenter, an equal and opposite force is applied to the load frame. The deflection of the load frame which results from the opposite reaction force is captured by the displacement sensor. This introduces an error into the load-displacement curve as the recorded displacement is a combination of the displacement of the load frame and the displacement into the specimen. Treating the system of the load frame and the specimen as two springs in series, the total

compliance, C, can be written as

$$C = C_s + C_f \tag{3.9}$$

where C is the total measured compliance, C_s is the compliance of the specimen, and C_f is the compliance of the load frame. Since the compliance of the specimen, C_s, is given by the inverse of the contact stiffness, S, the total measured compliance, C, can be rewritten using Eq. 3.3 as

$$C = C_f + \frac{\sqrt{\pi}}{2E_r}\frac{1}{\sqrt{A}} \tag{3.10}$$

If the elastic modulus of the material is constant, a plot of C vs $1/\sqrt{A}$ is linear, with the intercept being a direct measure of the load frame compliance. It is important to note that the compliance referred to here doesn't apply to the non-rigidity of the indenter which is accounted for by using the reduced elastic modulus in the analysis procedure.

There are several possible methods existing for determining the load frame compliance, C_f, using reference specimens that are homogenous and isotropic and for which both elastic modulus and Poisson's ratio are known. Oliver and Pharr [93,113] proposed an iterative technique to calibrate both the load frame compliance and indenter area function. According to Eq. 3.5, the area function of a Berkovich indenter can be simplified as

$$A(h_c) = 24.5h_c^2 \tag{3.11}$$

at large depth to provide a first estimate of the contact area. The initial estimate of the load frame compliance is obtained by plotting C vs $\sqrt{A}$ for two large indentations. Then the contact areas are recalculated using the initial estimate of the load frame compliance, leading to an initial fitting of the indenter area function based on Eq. 3.5. Using the new area function the procedure is applied and iterated until convergence is achieved. Another approach involves reference specimens with known elastic modulus and hardness and an additional assumption of constant hardness with depth. Inserting Eq. 3.8 into Eq. 3.10 yields

$$C = C_f + \frac{\sqrt{\pi}}{2E_r}\frac{\sqrt{H}}{\sqrt{P_{max}}} \tag{3.12}$$

Thus the load frame compliance can be directly determined from a C vs $1/\sqrt{P_{max}}$ plot.

Once the compliance of the load frame is known, the displacement into the specimen under load could be calculated by subtracting the displacement of the load frame, which is the product of the load frame compliance and the indenter load at each load increment, from the recorded total displacement.

Calibration of the indenter area function

Accurately determining the indenter area function is crucial for the measurement of elastic modulus and hardness as this error directly transfers into errors of calculating contact area and hardness. The projected contact areas are calculated from a series of indentations on reference materials of which the elastic modulus is constant with depth and fitted as a function of contact depth using Eq. 3.5, a multi-term polynomial form proposed by Oliver and Pharr. For a Berkovich indenter, the lead term, $C_0 = 24.5$, describes a perfect geometry of the Berkovich indenter, the others describe deviations from the Berkovich geometry due to blunting at the tip. Unlike determining the load frame compliance in which nanoindentations are performed with large depth, it is necessary to perform nanoindentations with a broad range of depth.

Indentation size effect

In nanoindentation studies hardness is often observed to increase with decreasing indentation depth, which is referred to as the indentation size effect (ISE) [112, 114–117]. The ISE is most often observed for material on which the indentation is performed using geometrically self-similar indenters, like pyramids and cones. Another scale-dependent behavior is called the reverse indentation size effect [118] where the hardness is found to increase with the increasing penetration depth.

The widely used model to explain the normal ISE in crystals is that developed by Nix & Gao [114]. The model is based on the concept of geometrically necessary dislocations (GNDs). The basic principle is in addition to the usual statistically stored dislocations produced during uniform straining, the GNDs give rise to an extra hardening component that becomes larger as the penetration depth decreases. The flow stress (σ) is related to the dislocation density, ρ_T, with the assumption that ρ_T is the simple sum of ρ_S and ρ_G, through the Taylor relation,

$$\sigma = \sqrt{3}\alpha G b \sqrt{\rho_S + \rho_G} \tag{3.13}$$

where α is the Taylor factor, G is the shear modulus, b is the Burger's vector, ρ_S is the density of statistically stored dislocations and ρ_G is the density of geometrically necessary dislocations. An estimate of the density of GNDs is given by [119]:

$$\rho_G \approx \frac{4\gamma}{bD} \tag{3.14}$$

where D is the diameter of the residual indentation impression and γ is an average strain. Through the Taylor relation, the hardness H is related to the flow stress by

$$H = 3\sigma \tag{3.15}$$

Combing Eqs 3.13, 3.14 and 3.15, it yields

$$H \approx \sqrt{3}\alpha G b \sqrt{\rho_S + \frac{4\gamma}{bD}} \tag{3.16}$$

Thus the hardness is inversely proportional to the square root of the mean diameter of the indentation residual impression.

Determining the elastic modulus and hardness of a thin films on a substrate

The analysis method proposed by Oliver and Pharr [93] in 1992 has become the standard for determining the indentation hardness and elastic modulus from the load-displacement curve for bulk materials. The main difficulty of nanoindentation on thin films is to avoid the unintentional probing of the properties of the substrate. In general, the effect of the substrate increases with increasing indentation depth and with increasing elastic mismatch between film and substrate. One common rule of thumb is to keep the indentation depth in a test to less than 10% of the film thickness [120] to avoid the substrate effects. This empirical rule is experimentally feasible for films that are greater than about 1 μm thick, but not reliable for very thin films. For example, nanoindentation on a 0.1 μm thick film requires a maximum indentation depth less than 10 nm according to this rule. Accurate measurements at this scale are difficult due to the uncertainties in the indenter geometry, environmental vibrations, and the effects of surface roughness.

Several approaches to model the substrate effects and to extract intrinsic material properties of thin films have been reported [94, 121–123]. The simplest empirical expression for determining the elastic modulus of a thin film on a substrate is linear [94]:

$$E = E_f + (E_s - E_f)(x) \tag{3.17}$$

$$\frac{1}{E_r} = \frac{\left(1-\nu^2\right)}{E} + \frac{\left(1-\nu_i^2\right)}{E_i} \tag{3.18}$$

where E, E_s and E_f are the elastic moduli of the film-substrate system, the substrate and the thin film, ν and ν_i are Poisson's ratio for the film-substrate system and the indenter. Parameter x is defined as $\frac{a_c}{t}$, where a_c is the mean radius of the contact area, and t is the film thickness. A severe problem with this linear model is that it gives unrealistic values when it is used to extrapolate to large depths of penetration.

Gao et al., [123] developed an analytical solution using an approximate first-order perturbation method for the contact of a rigid cylindrical punch with a homogenous half space with a surface layer of a different material. The effective modulus of the film-substrate system is determined in

closed form as the averaged indentation moduli of the film and the substrate with a weight function, ϕ_{Gao}, with x being defined as a_c/t,

$$E = E_s + (E_f - E_s)(\phi_{Gao}) \tag{3.19}$$

$$\phi_{Gao} = \frac{2}{\pi} arctan\frac{1}{x} + \frac{1}{2\pi(1-\nu)} \times \left[(1-2\nu)\frac{1}{x} ln(1+x^2) - \frac{x}{1+x^2}\right] \tag{3.20}$$

$$\nu = 1 + \left[\frac{(1-\nu_s)(1-\nu_f)}{1-(1-\phi_1)\nu_f - \phi_1\nu_s}\right] \tag{3.21}$$

$$\phi_1 = \frac{2}{\pi} arctan\frac{1}{x} + \frac{1}{x\pi} ln(1+x^2) \tag{3.22}$$

This approach overestimates the substrate effect when the film is stiffer than the substrate and underestimates the substrate effect when the film is more compliant than the substrate [124]. This error significantly increases with the increase of elastic mismatch between the film and the substrate.

By treating the film-substrate system as two springs in series, Doerner and Nix [121] proposed an empirical solution to determine the elastic modulus of thin films , namely,

$$\frac{1-\nu^2}{E} = \frac{1-\nu_f^2}{E_f} + \left(\frac{1-\nu_s^2}{E_s} - \frac{1-\nu_f^2}{E_f}\right) e^{-\alpha x} \tag{3.23}$$

where $x = t/h_c$, and α is an empirically constant determined using the method of least squares. This solution has been modified by King [122] with the replacement of $x = t/h_c$ by $x = t/a_c$ with a_c being the mean radius of contact area and then updated by Saha and Nix [125] with replacement of $x = t/h_c$ by $(t - h_c)/a_c$, where $t - h_c$ describes the effective thickness of the film beneath the indenter because of plastic flow during loading.

The hardness of a thin film on a substrate is more difficult to quantify than the elastic modulus because of the complex nature of the plastic zone as it interacts with the substrate material. Buckle [126] proposed the effective hardness of a film-substrate system is linearly related with the hardness of the film and the substrate, and expressed as,

$$H_{eff} = \alpha H_f + (1-\alpha) H_s \tag{3.24}$$

where α is an empirical parameter. Jonsson and Hogmark [127] modified the expression with replacement of the parameter α with A_f/A, where A_f is the relative part of the contact contributed by the film, and A is the total contact area. Rather than using the projected contact area as a measure of the relative contribution to the effective hardness from the film and the substrate, Burnett and

Rickerby [128] updated parameter α with a relative volume ratio of the plastic zones (V_f/V) based on a volume law of mixtures.

With all the efforts and investigations into all kinds of film substrate configurations by previous researchers, there is no one relationship proposed which covers a wide range of material behaviors. The 10% of the thickness rule seems to be the most generally used.

Experimental

In this study, nanoindentation experiments were performed using a load-controlled commercial nanoindenter. A diamond Berkovich indenter was used for all the experiments. Before performing nanoindentation, the machine and the specimens were allowed to thermally equilibrate for 12 hrs in a thermal enclosure. Indentation on the specimens were separated with a spacing 50 μm in order to avoid the interference from the previous indentation. The frame compliance and area function of the indenter were calibrated following the procedure discussed in the previous section. The reference specimen used in the calibration is fused silica having a hardness of 9.25 GPa and a reduced elastic modulus of 69.6 GPa. It is noted that when the contact depth approaches the value R/3, with R being the radius of the indenter curvature, the hardness values become unreliable which is a normal effect due to tip roundness. The values for reduced modulus stay relatively constant because the values was defined as 69.6 GPa when the area function was calibrated. However hardness is a computed value that is dependent on the projected contact area between the indenter and the specimen. As the contact depth approaches R/3, the projected contact area described by the indenter area function starts deviating from the true projected contact area. This deviation becomes significant when the contact depth is less than R/3. It is recommended to perform nanoindentation with contact depth larger than R/3 ($\sim$30 nm for the Berkovich indenter we used). The calibrated range is from $\sim$30 nm up to 190 nm using fused silica as a reference, However it is reasonable to extend this range to higher depth given the indenter is not damaged as the area function calibrated will imitate the ideal shape of the indenter at deeper depths.

Thermal drift, referring to a change in dimension of the indenter, the specimen and the instrument from a temperature change is vital in performing shallow indentations as it directly affects the calculation of the hardness by affecting the contact depth. It also affects the measurements of the reduced elastic modulus because it affects the slope of the unloading curve. In order to reduce the effects of thermal drift, the instrument is placed in a insulated cabinet. As a further step to eliminate the effects of thermal drift, the thermal drift is monitored for 40 s at the preloading stage when a setpoint force of approximately 2 μN is maintained between the tip and the specimen before the

indentation or calculated by setting up a holding section at the end of the unloading part of the test cycle. The drift rate, in nm/s, is then used to correct the displacement reading by subtracting the product of the drift rate and the time at which the displacement reading was recorded. The loading function used in this study has three segments as shown in Fig. 3.4: 10 s loading, 20 s holding of the maximum load and 10 s unloading. The drift rate was monitored to be less than 0.05 nm/s.

Surface roughness has a negative influence on the nanoindentation test results, especially at shallow depth of penetration as it brings large uncertainty in the determination of the contact area. In order to obtain an uncertainty of the indentation depth less than 5% of the indentation depth, the indentation depth should be at least 20 times the arithmetic roughness Ra of the specimen surface [129]. The root mean square surface roughness Rq measured by AFM for all specimens was found to be approximately 1 nm for the acid-catalyzed films and 3 nm for the base catalyzed films over a scan size of 1 μm $\times$ 1 μm. For a given surface, Rq is larger than Ra by approximately 10%.

Therefore for shallow indentations, the contact depth is required to be larger than $\sim$30 nm) to minimize the effects of the tip roundness. Also it needs to be larger than the 20 times of the surface roughness, which is 20 nm for the acid catalyzed-films and 60 nm for the base catalyzed films, in order to reduce the uncertainty of the depth measurements.

3.3.2 Rutherford Backscattering Spectrometry

Rutherford backscattering spectrometry (RBS) is an ion scattering technique. It has been widely used for compositional analysis of thin films, including detection of impurities and quantitative identification of elemental composition and depth profiling of individual elements. RBS is unique in that it allows quantification without the use of reference standards. The theory of Rutherford scattering is briefly discussed below.

Considering a simple elastic collision between an incident ion and a stationary target atom, the energy after collision can be determined by applying the principles of conservation of energy and momentum. A schematic of an elastic collision between an incident ion of mass M_1, atomic number Z_1, velocity v_0, and energy E_0 and a stationary target atom of mass M_2 and atomic number Z_2 is shown in Fig. 3.6. After the collision, the incident ion and the target atom have velocities and energies v_1, E_1 and v_2, E_2, respectively. The scattering angle θ and recoil angle ϕ are defined as shown in Fig. 3.6.

Conservation of energy and momentum are express by the equations:

$$\frac{1}{2}M_1v_0^2 = \frac{1}{2}M_1v_1^2 + \frac{1}{2}M_2v_2^2 \tag{3.25}$$

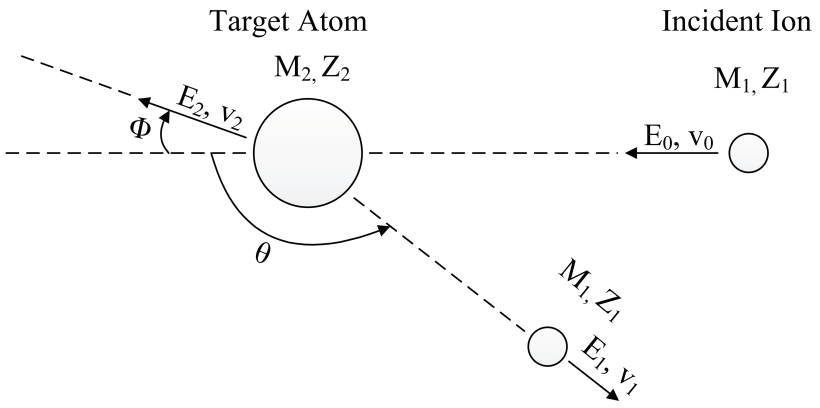

Figure 3.6: A schematic of an elastic collision between an incident ion of mass M_1, velocity v_0, and energy E_0 and a stationary target atom of mass M_2 ($\geq M_1$).

$$M_1 v_0 = M_1 v_1 cos\theta + M_2 v_2 cos\phi \tag{3.26}$$

$$0 = M_1 v_1 sin\theta - M_2 v_2 sin\phi \tag{3.27}$$

The energy of the incident ion after elastic collision is solved by eliminating ϕ and v_2 in Eqs. 3.25, 3.26 and 3.27. Now define the ratio of the energy of the incident ion after the elastic collision to that before the collision as the kinematic factor K,

$$K = E_1/E_0 \tag{3.28}$$

Therefore, one obtains

$$K = \left[\frac{\pm(M_2^2 - M_1^2 sin^2\theta)^{1/2} + M_1 cos\theta}{M_1 + M_2}\right]^2 \tag{3.29}$$

where the plus sign is taken when $M_1 \leq M_2$, otherwise the minus sign is taken. If the primary energy E_0 of the incident ion and its mass M_1 are known, and the energy E_1 after the collisions could be measured at a known scattering angle θ, the mass M_2 of the target atom that caused the scattering can be determined from Eq. 3.29.

While the kinematic equation determines the mass of the unknown target, it does not describe the probability of observing such an event. Therefore, the differential scattering cross section of the backscattering event ($\frac{d\sigma}{d\Omega}$) is needed and was given first in laboratory coordinates by Darwin in 1914 [130],

$$\frac{d\sigma}{d\Omega} = \left(\frac{Z_1 Z_2 e^2}{4E}\right)^2 \frac{4}{sin^4\theta} \frac{\{[1 - ((M_1/M_2)sin\theta)^2]^{1/2} + cos\theta\}^2}{[1 - ((M_1/M_2)sin\theta)^2]^{1/2}} \tag{3.30}$$

where σ is the scattering cross section, Ω is the detector solid angle. The Rutherford cross section is calculated based on the assumption that the forces acting during the collision between the projectile and the target atom are well described by the Coulombic repulsion of the two nuclei. When the energy of the incident ion is so high that the ion starts penetrating the Coulomb barrier of the target atom, the so called non-Rutherford cross section must be considered. As the distance of closet approach during collision is close to the nuclear dimensions, nuclear resonance becomes significant causing considerable deviation of the scattering cross section from Rutherford cross section. There have been attempts to model the threshold energy for non-Rutherford scattering [131–133], and over the past ten years non-Rutherford cross sections have been measured and evaluated, which could be used in ion beam analysis for precise analysis.

A Rutherford backscattering system generally includes three essential components: an ion source, a particle accelerator and a detector capable of measuring the energies of backscattered ions at the scattering angle. The energy of the scattered ions is detected and the yield of the scattered ions at the detected energy is also recorded. Therefore a RBS spectrum is generated as a plot of the yield vs. the scattered energy.

A schematic of backscattering events in a specimen consisting of a monoisotopic element and the resultant RBS spectrum is shown in Fig. 3.7. The incident beam, the direction of detection, and the specimen normal are coplanar. A collimated ion beam with energy E_0 impinges the specimen at an incident angle θ_1. The backscattered ions are collected at scattering angle θ. Considering the specimen consisted of slabs with thickness τ_i from which all the backscattering events are recorded, the number of atoms in each slab is given by $N\tau_i$, where N is the atomic density of the specimen. The thickness of each slab is corresponding to the energy width of the detector ϵ (in keV/channel). The total number of particles detected (H_i) corresponding to slab i is expressed as

$$H_i = \sigma(E_i)\Omega Q N \tau_i / cos\theta_1 \tag{3.31}$$

where $\sigma(E_i) = \frac{d\sigma}{d\Omega}$ is the differential cross section evaluated at energy E_i and Q is the total number of particles incident on the specimen. When the incident beam interacts with a compound target at the surface, the yield from each element is shown as a surface peak in the spectrum at different detected energies defined by the kinematic factor (K). The areal density (a measure of thickness used in ion beam analysis) can be obtained by the integral of $N\tau_i$ from Eq. 3.31. Thus the depth profile of each element in the specimen can be determined.

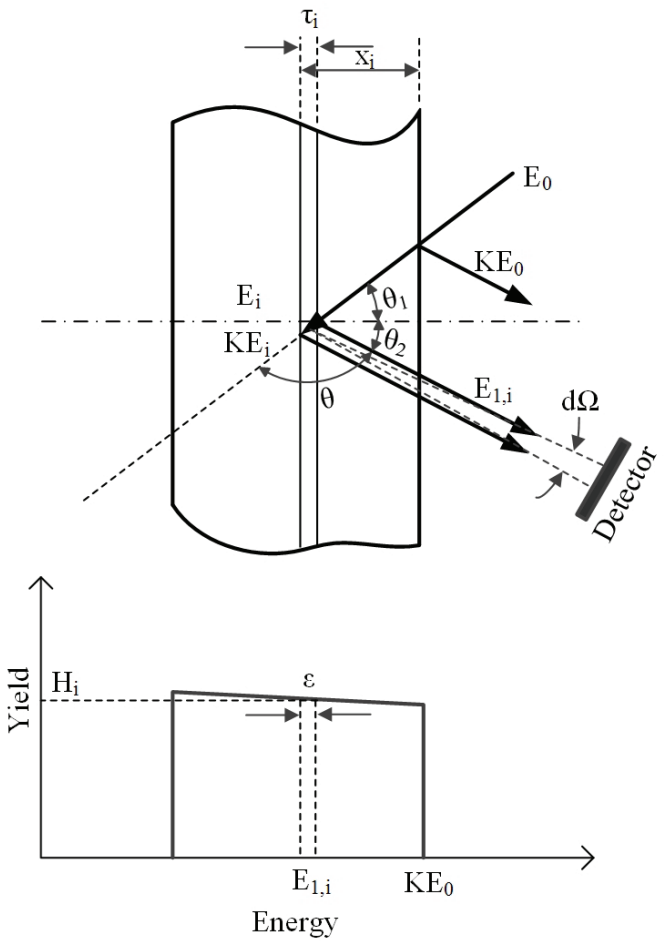

Figure 3.7: A schematic of backscattering events in a specimen consisting of a monoisotopic element and the resultant RBS spectrum. The incident beam, the direction of detection, and the specimen normal are coplanar.

Experimental

In this study, a collimated beam of 3.83 MeV $^4He^+$ ions was produced by a NEC Pelletron tandem accelerator in the Ion Beam Materials Laboratory at Los Alamos National Laboratory. In a tandem accelerator negative ions produced by an appropriate ion source are accelerated from ground to the positively charged high voltage terminal where the electrons from the incoming ions are stripped resulting in desired positively charged ions. The incident ions experience a second time acceleration when traveling to the ground at the other end of the machine. The resulting kinetic energy (E) of the beam is given by:

$$E = (e + q)U \tag{3.32}$$

where, e is the absolute value of the charge of an electron, q is the desired charge of the incident ion, and U is the terminal voltage.

The backscattered ions are detected at a scattering angle of 167° in the Cornell geometry in which the incident beam, the exit beam and the specimen rotation axis are in the same plane. The incident angle is 0° in this study while the exit angle is defined as

$$cos\theta = -cos\theta_1 cos\theta_2 \tag{3.33}$$

Each spectrum was obtained with accumulated beam charge of 12 μC.

3.3.3 Elastic Recoil Detection

Similar to RBS, elastic recoil detection (ERD) is also an ion beam spectroscopic technique, but it is capable of detecting light elements. As an energetic ion beam is directed at the specimen at a grazing angle, electronic and nuclear interactions between incident ions and target atoms occurs causing the lighter target atoms to recoil, which are collected by a detector. In most cases, a proper absorber, typically a Mylar foil, is placed in front of the detector which blocks the backscattered incident ions and allows lighter target atoms passing through to the detector.

A schematic of an ERD experiment is shown in Fig. 3.8. An incident ion with energy E_0, mass M_1, and atomic number Z_1 penetrates into the specimen at an incident angle θ_1. At the projected depth x_i, the projectile has an energy $E_0^{'}$ just before scattering with a target atom with mass M_2 and atomic number Z_2. The recoiled atom is scattered at a scattering angle defined as $\theta = \pi - (\theta_1 + \theta_2)$.

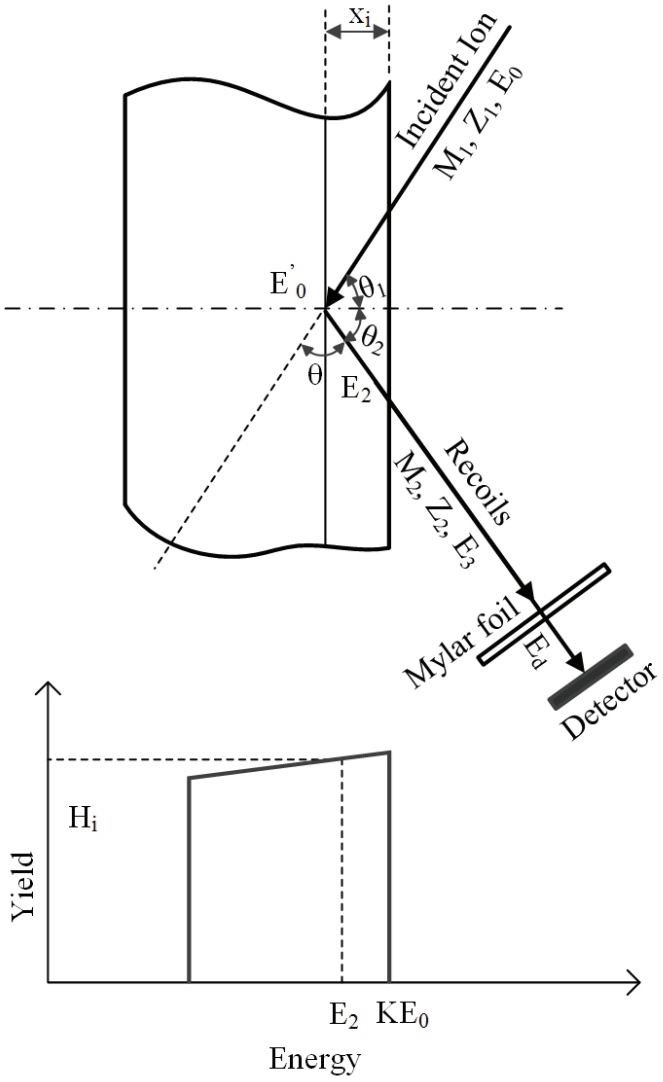

Figure 3.8: A schematic of an ERD experiment showing: the incident and exit angles (θ_1 and θ_2), the energy loss (E_0-$E_0^{'}$) of the incident beam at depth x_i, the energy (E_2) of the recoiled atom at depth x_i, the energy (E_3) of the recoiled atom after it exits the specimen, and the energy (E_d) of the recoiled atom passing through a mylar foil detected by a surface barrier detector.

The yield (Y_r) for the recoil atoms detected at energy E_d with an energy width δE_d is given by

$$Y_r(E_d) = \frac{\phi N_r(x_i)\sigma_r(E_0^{'},\theta)\Omega\delta E_d}{cos\theta_1 dE_d/dx} \tag{3.34}$$

where ϕ is the fluence of the projectile, $N_r(x_i)$ is the atomic number density of the recoiled atom at depth x_i, $\sigma_r(E_0^{'},\theta)$ is the recoil differential scattering cross section in laboratory coordinates, and dx is the increment of depth at x_i corresponding to an increment of energy dE_d. In order to obtain a concentration profile ($N_r(x_i)$) from the yield (Y_r), analytical expressions for $\sigma_r(E_0^{'},\theta)$, δE_d and dE_d/dx must be determined as ϕ, Ω and θ_1 are fixed in the experimental configuration.

The recoil differential cross section is governed by Coulombic scattering and was given by Marison and Young (1968) [134] as:

$$\sigma_r(E_0^{'},\theta) = \frac{[Z_1 Z_2 e^2(M_1+M_2)]^2}{[2M_2 E_0^{'}]^2 cos^3\theta} \tag{3.35}$$

The energy width δE_d is determined using a reference specimen which has a well known H concentration profile. The energy scale dE_d/dx varies with the projected depth x_i and is solved by considering the specimen consisted of many thin slabs similar to the RBS analysis.

Experimental

ERD was performed at Los Alamos National Laboratory. A 2.85 MeV $^4He^+$ ion beam was incident at an angle of 75° in the IBM geometry. The recoiled atoms were detected at a scattering angle of 30° while the exit angle is given by

$$\theta = 180 - \theta_1 - \theta_2 \tag{3.36}$$

In IBM geometry the incident beam, exit beam and the surface normal are in the same plane. A 12 μm thick Mylar foil was placed in front of the ERD detector to block the backscattered projectiles.

3.3.4 X-ray Diffraction

X-ray diffraction is an analytical technique primarily used for phase identification of a crystalline material. The interaction of the incident X-rays with the crystalline material produces constructive interferences if the conditions satisfy Bragg's Law [135] which relates the wavelength of the incident X-ray to the diffraction angle and the interplanar spacing in a crystal. By comparing the interplanar spacings with standard reference patterns, the material is identified and crystalline orientations are determined.

The XRD experiments were performed at Los Alamos National Laboratory and in the Helmerich Research Center in Tulsa.

3.3.5 Scanning Electron Microscopy

Scanning electron microscope uses electrons as the source of illumination, and produces images from the secondary electrons resulting from the interactions of the incident electrons and atoms in the specimen. SEM is commonly used to study the surface structures.

SEM experiments were performed using a FEI Quanta 600 Field-Emission SEM located in the Oklahoma State University (OSU) Microscopy Laboratory at the Oklahoma Technology & Research Park with a maximum resolution of 1.2 nm at the maximum accelerating voltages of 30 kV.

Chapter 4

RESULTS AND DISCUSSION

4.1 Surface Characterization of Heat Treated and Ion Irradiated Acid Catalyzed Sol-gel Films

4.1.1 Surface Topography Characterization

The surfaces of the green films and the films after heat treatment or ion irradiation were investigated using atomic force microscopy. Surface topography of the films measured by AFM over a scan size of 10 μm $\times$ 10 μm up to 40 μm $\times$ 40 μm did not show any signs of surface cracks on the green films, the films heat treated at 300 - 800 °C in ambient air or in vacuum, and the film heat treated at 1100 °C in an Ar flow. The film heat treated at 1350 °C in Ar flow for 2 hrs exhibited numerous bubbles as shown in Fig. 4.1(a) observed with an optical microscope with a 20X objective. The observed bubbles might result from the interaction between the silica film and the silicon substrate at the interface forming gaseous SiO, through [44]:

$$SiO_2(s) + Si(s) \rightarrow 2SiO(g) \tag{4.1}$$

Surface topography measured by AFM at bubble-free areas over a scan size of 10 μm $\times$ 10 μm revealed surface cracks indicated by the red arrows in Fig. 4.1 (b). The thermal expansion mismatch between the films and the substrate might be responsible for the cracking as a result of releasing high residual compressive stress upon cooling [136]. Another possible reason for the cracks was the generation of bubbles as a result of chemical reactions between the films and the Si substrate forming gaseous SiO [44]. Compared with heat treatment, ion irradiations with 125 keV H^+, 200 keV H^+, 250 keV N^{2+}, 400 keV N^{2+}, 1 MeV Cu^+, 4 MeV Cu^{2+} and 9 MeV Cu^{3+} at varying fluences from

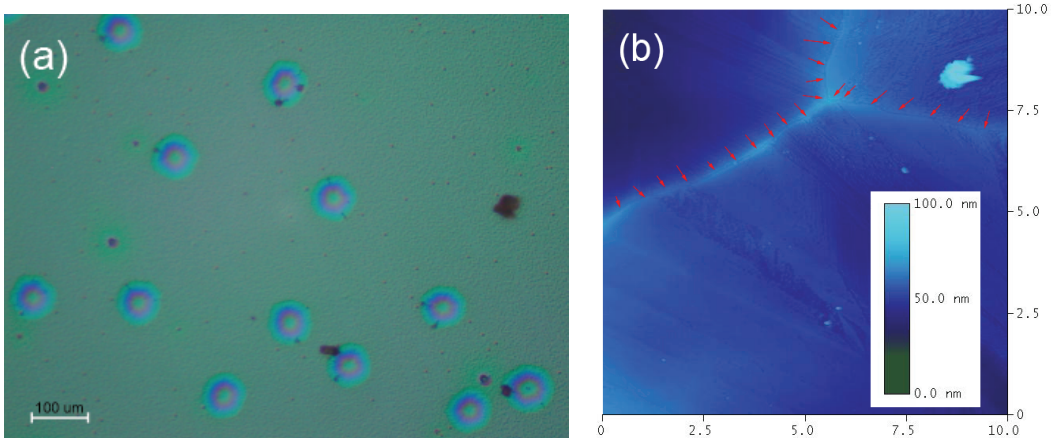

Figure 4.1: (a) A microscopic image of the acid catalyzed film heat treated at 1350 °C in Ar for 2 hrs showing numerous bubbles, and (b) surface topography measured by AFM at bubble-free areas over a scan size of 10 μm × 10 μm showing surface cracks.

10^{13} up to 2 × 10^{17} ions/cm^2 did not introduce any surface cracks.

Selected films were also prepared and investigated by scanning electron microscopy (SEM). Figure 4.2 shows the SEM images taken from: 600 nm thick acid catalyzed films (a) heat treated at 300 °C for 10 min, (b) heat treated at 800 °C for 10 min, and (c) irradiated with 250 keV N^{2+} at a fluence of 10^{15} ions/cm^2. SEM images were taken near scratches created for thickness measurements deliberately such that both the films and the substrate were imaged. There was no sign of cracks observed on the investigated films, consistent with the AFM results. Also there was no visible porosity observed on the investigated surfaces which could be due to pores being smaller than the resolution of the SEM or no open pores on the surface.

Surface buckling was observed on some ion irradiated films after being stored in the laboratory at room temperature for about one month. The films irradiated with H^+ at a fluence of 1 × 10^{16} ions/cm^2 exhibited localized fishbone-like buckling while the films irradiated at a fluence of 1 × 10^{17} ions/cm^2 or above were completely delaminated as a result of overwhelming buckling. There was no buckling observed on the films irradiated with 400 keV N^{2+}, 1 MeV Cu^+, 4 MeV Cu^{2+} and 9 MeV Cu^{3+} at fluences up to 1 × 10^{16} ions/cm^2 and the films after heat treatment at 300 - 800 °C in ambient air or in vacuum, even at 1100 °C in Ar for 2 hrs. The buckling defects were attributed to the high residual compressive stress resulting from ion irradiation [137, 138].

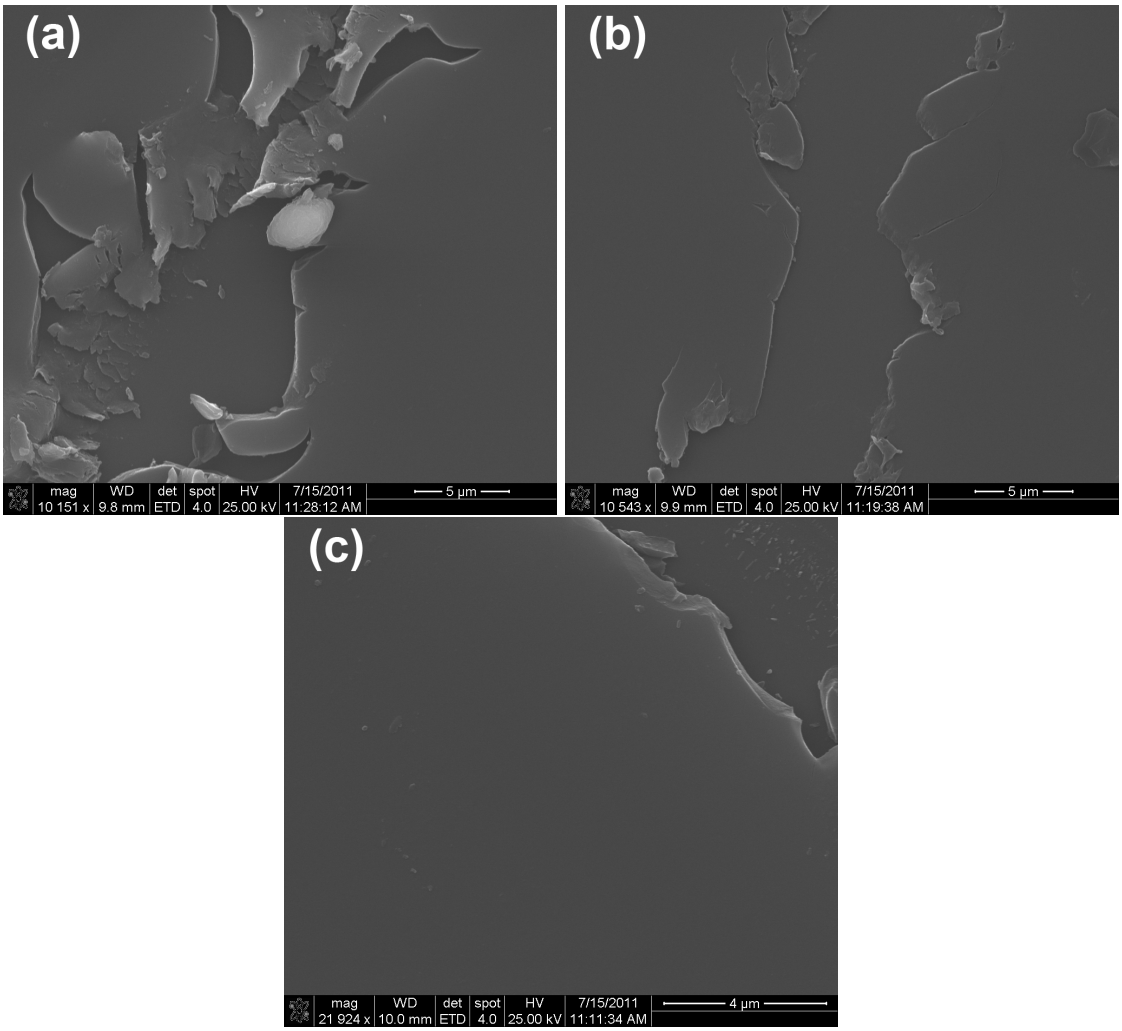

Figure 4.2: SEM images of the surface of 600 nm thick acid catalyzed films (a) heat treated at 300 °C for 10 min, (b) heat treated at 800 °C for 10 min, and (c) irradiated with 250 keV N^{2+} at a fluence of 10^{15} ions/cm^2.

4.1.2 Surface Roughness Measurements

Surface roughness of the specimens investigated was measured by AFM over a scan size of 1 μm $\times$ 1 μm. Prior to heat treatment and ion irradiation, the acid catalyzed films had a surface roughness Rq (defined as the root mean square height of the surface) of approximately 1 nm. Neither heat treatment in ambient air or in vacuum at the temperatures 300 - 800 °C, nor ion irradiation had a noticeable influence on the measured surface roughness. Surface roughness of the film heat treated at 1100 °C in Ar for 2 hrs was measured to be 1.2 nm Rq, comparable with the other heat treated and ion irradiated films.

4.2 The Effects of Heat Treatment on the Acid Catalyzed Sol-gel Films

4.2.1 Thickness and Mechanical Properties Characterization

The change in the film thickness as a result of heat treatment was measured by AFM using a step height technique [17]. By creating a scratch with a razor blade, a step is formed between the exposed substrate and the remaining film. Error in the measurement of the film thickness could result if the films are not completely removed from the substrate, the cut goes into the substrate, and/or material builds up along the edge of the scratch. The surface roughness of the scratched area was measured to be $\sim$1 nm over a scan size of 1 μm $\times$ 1 μm, suggesting the films are completely removed from the Si substrate and there is no measurable surface damage to the substrate as a result of the scratch. An AFM scan size of 40 μm $\times$ 40 μm has proven to be sufficient to successfully measure the topography of the scratch edge, a large portion of the scratched area, and an extended area of the film (consisting of the area where the material builds up along the edge and a large area of flat surface). The scratches were made on each green film before heat treatment or ion irradiation to avoid the situation that the converted film is too hard to scratch. Figure 4.3 shows film thickness and shrinkage of the acid catalyzed films heat treated in ambient air and in vacuum as a function of heat treatment temperature. All reported data represent the average of five experiments with the error bars representing the maximum and minimum values obtained. Film thickness was observed to monotonically decrease with increasing heat treatment temperature in the range of temperatures investigated as a result of the organic components oxidation (or decomposition), polymerization and structural relaxation [18]. The green films used in the ambient air heat treatment showed thicknesses about 70 nm higher than those used in the vacuum heat treatment due to the repeatability of the

film production in different batches. Therefore a better way to evaluate the change of thickness after heat treatment is using shinkage, a change of thickness divided by the green film thickness. The shrinkage of the film heat treated in ambient air was constantly ∼20% higher than the film heat treated in vacuum when compared at the same temperature above 400 °C. At 400 °C, heat treatment in air introduced a 34% shrinkage while heat treatment in vacuum caused a 10% shrinkage. This is mainly due to the fact that decomposition of the organic groups requires a higher temperature in vacuum than the oxidization of the same organics in ambient air. For example, oxidation of the methyl groups in MTES starts at ∼350 °C in air while thermal cleavage of Si-CH_3 bonds in vacuum requires a temperature above 650 °C [36,139]. The film heat treated at 800 °C in ambient air had a thickness of 250 nm, a shrinkage of 68% with respect to the green film, while the film heat treated at the same temperature in vacuum had a thickness of 370 nm, a shrinkage of 48%.

The effect of heat treatment on the hardness and reduced elastic modulus was investigated using nanoindentation. Figure 4.4 shows the hardness and reduced elastic modulus of the acid catalyzed films as a function of heat treatment temperature after heat treatment in ambient air and in vacuum. All reported data represent the average of five indentations at a contact depth/film thickness ratio of 10%, and the error bars represent the maximum and minimum values obtained. The films heat treated in ambient air showed a gradual increase in hardness with increasing temperature from 0.3 GPa at 300 °C to 1.2 GPa at 800 °C. Unlike the shrinkage behavior, the measured hardness of the films heat treated in vacuum remained relatively constant up to 600 °C and then increased. At 800 °C, the effect of heat treatment environment (ambient air or vacuum) on the measured hardness was negligible. The measured reduced elastic modulus of the films heat treated in vacuum exhibited a continuous decrease up to 500 °C and then increased with increasing temperature while the reduced elastic modulus of the films heat treated in ambient air remained relatively constant up to 500 °C after which it increased.

The increase of hardness and reduced elastic modulus with increasing temperature in ambient air was supported by FT-IR experiments performed on the same specimens by Prenzel [90]. It was found that with increasing temperature in ambient air the organic components were gradually oxidized and a stronger network was formed through polymerization and decreasing film porosity [140, 141]. Compared with heat treatment in ambient air, the decomposition of the organic components was completed at higher temperature (800 °C compared to 600 °C in air) consistent with the abrupt increase in the measured hardness and reduced elastic modulus of the film heat treated in vacuum at 800 °C.

Further increasing the mechanical properties can be achieved by performing heat treatment at

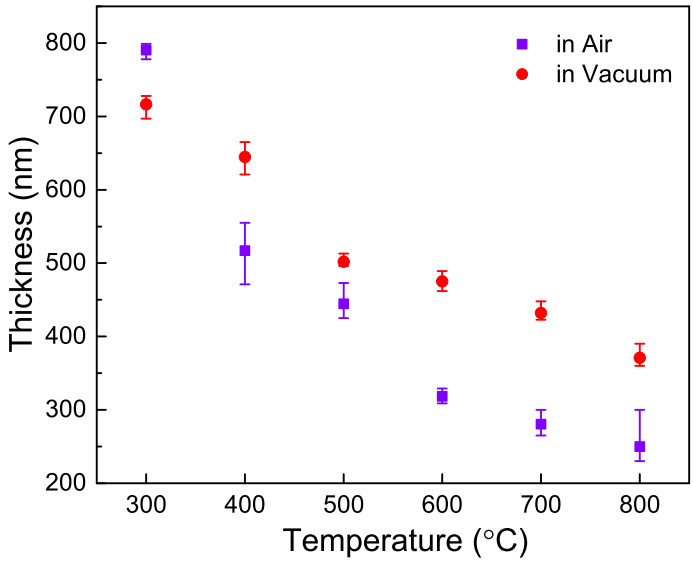

(a) Thickness

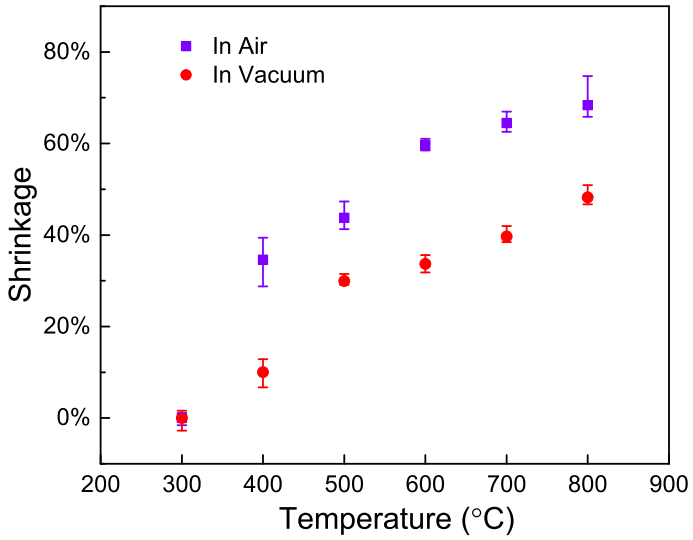

(b) Shrinkage

Figure 4.3: Plots of (a) film thickness and (b) shrinkage of the acid catalyzed films heat treated in ambient air and in vacuum as a function of temperature.

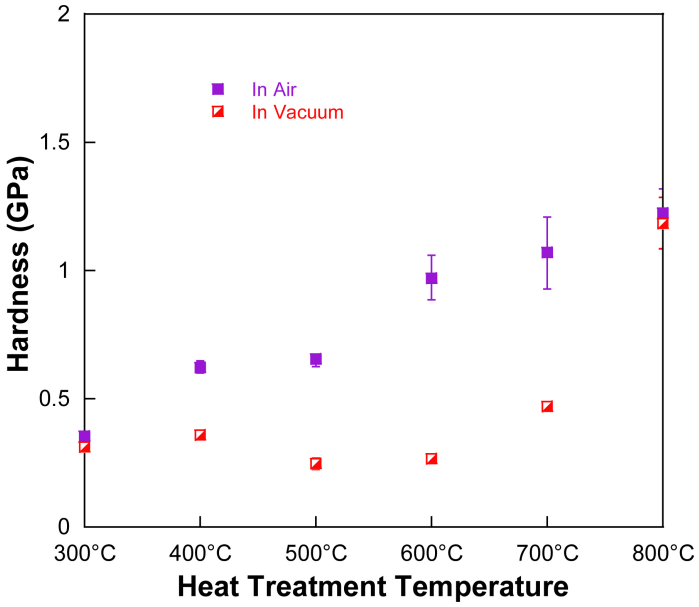

(a) Hardness

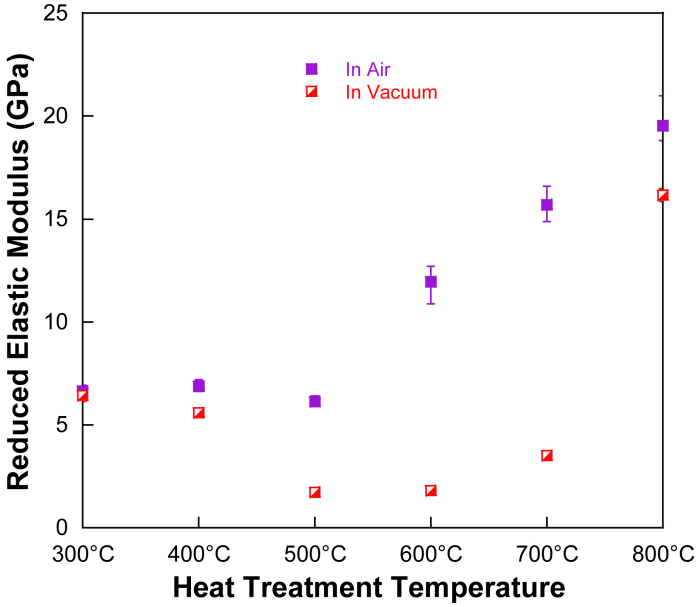

(b) Reduced elastic modulus

Figure 4.4: Plots of (a) hardness and (b) reduced elastic modulus of the acid catalyzed films heat treated in ambient air and in vacuum as a function of temperature.

even higher temperature in vacuum or an inert gas. The film heat treated at 1100 °C in Ar for 2 hrs had a thickness of ∼100 nm. The hardness and reduced elastic modulus depth profiles obtained by nanoindentation are shown in Fig. 4.5. The hardness was determined to be 8.7 GPa at a contact depth of 30 nm and the reduced elastic modulus was extracted based on the model proposed by Doerner and Nix [121] to be 68.7 GPa. The measured hardness and reduced elastic modulus were in good agreement with amorphous fused silica (a hardness of 9.2 GPa and reduced elastic modulus of 69.6 GPa), suggesting the microstructure of the heat treated film is similar to amorphous silica.

4.2.2 Chemical Structure of the Green Films

The changes in film shrinkage and mechanical properties were attributed to the structural evolution during heat treatment. The chemical nature of the green film is described next. The acid catalyzed sols were prepared with precursors of 0.4 mol TEOS, 0.6 mol MTES and 1 mol H_2O, which were all involved in the hydrolysis and condensation reactions in the sol-gel process. The content of H_2O significantly affects the progress of the chemical reactions therefore affecting the chemical structure of the final product after the drying process [142]. The most obvious effect of the increased H_2O/Si ratio is the acceleration of the hydrolysis reactions [18]. Lower concentration of H_2O leads to large fractions of the unhydrolyzed monomers existing in the gel. For a sol starting with 0.4 mol TEOS and 0.6 mol MTES, the theoretical minimum requirement of the H_2O in order to fully eliminate all ethoxyl groups through hydrolysis and condensation is 1.7 mol, leading to a theoretical chemical composition with formula $SiO_{1.7}(CH_3)_{0.6}$. Calculation was based on the chemical reactions in the hydrolysis and condensation detailed in Figs. 2.1 and 2.2 that 1 mol TEOS requires 2 mol H_2O and 1 mol MTES needs 1.5 mol H_2O to completely hydrolyze all the ethoxyl groups. In the process of preparing the sols used in this study, the H_2O content was 1 mol, which is less than the theoretical minimum value, resulting unhydrolyzed ethoxyl groups . The theoretical chemical composition is described as $SiO(OC_2H_5)_{1.4}(CH_3)_{0.6}$ with the assumption that all H_2O was consumed in the chemical reactions and no hydroxyl groups was left for further condensation. In reality, the condensation is reversible up to 400 °C such that there are always hydroxyl groups existing in the sols prepared at 50 °C after the condensation process. This adds hydroxyl components into the theoretical formula and increases the ethoxyl content. The ethoxyl groups were reported to start degradation at ∼250 °C [33, 142] while methyl groups in MTES were thermally stable up to 350 - 450 °C in ambient air [33, 35–37]. PVP started partial decomposition at a low temperature of ∼230 °C in a gel network and still existed up to ∼510 °C [41]. Therefore the green films which were produced after heat treatment

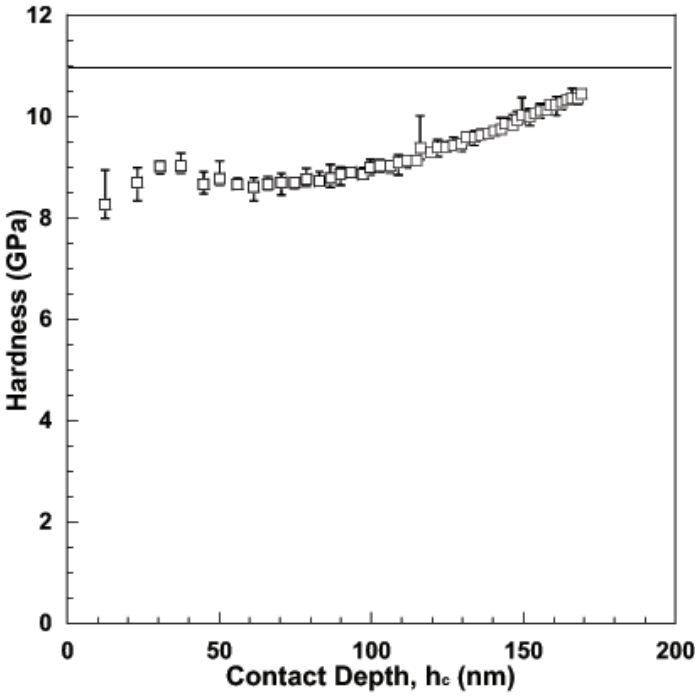

(a) Hardness

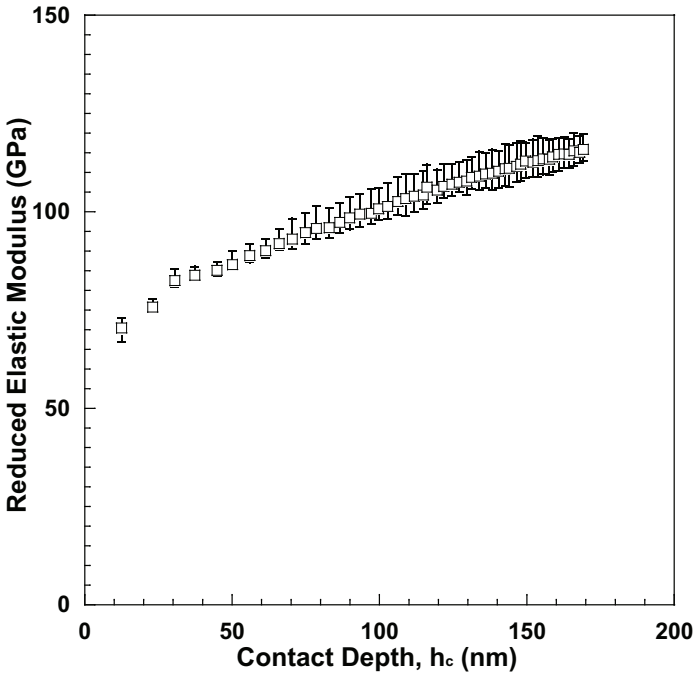

(b) Reduced elastic modulus

Figure 4.5: Depth profiles of (a) hardness and (b) reduced elastic modulus obtained by nanoindentation for the acid catalyzed film heat treated at 1100 °C in Ar for 2 hrs. A horizontal line shows the hardness of the (100) Si substrate.

at 300 °C in ambient air for 30 min had a complex chemical structure consisting of unhydrolyzed ethoxyl groups, methyl groups, hydroxyl groups and partially degraded PVP.

4.2.3 Change of Chemical Composition During Heat Treatment

The analysis of the chemical composition from RBS/ERD data was accomplished by using the SIMNRA software [143]. Figure 4.6 shows a schematic of a SIMNRA RBS spectrum representing the Si, O, C and N related peaks. The probing ion is 3.83 MeV $^4He^+$ with a scattering angle of 167° for RBS, and 2.85 MeV $^4He^+$ with a scattering angle of 30° for ERD. In the RBS spectrum as shown in Fig. 4.6, the Si, O and C associated peaks are easily distinguished but the N associated peak is weak. This is due to the fact that the differential cross section of a He-N collision is significantly lower than the others, and the low concentration of N in the film. As a consequence of the low sensitivity of detecting N content, the analysis of N content is disregarded in this study. Details of the differential cross sections of He-N, He-O, He-C, and He-Si collisions are generated from the Ion Beam Analysis Nuclear Data Library (IBANDL) [144] and listed in Appendix *B*.

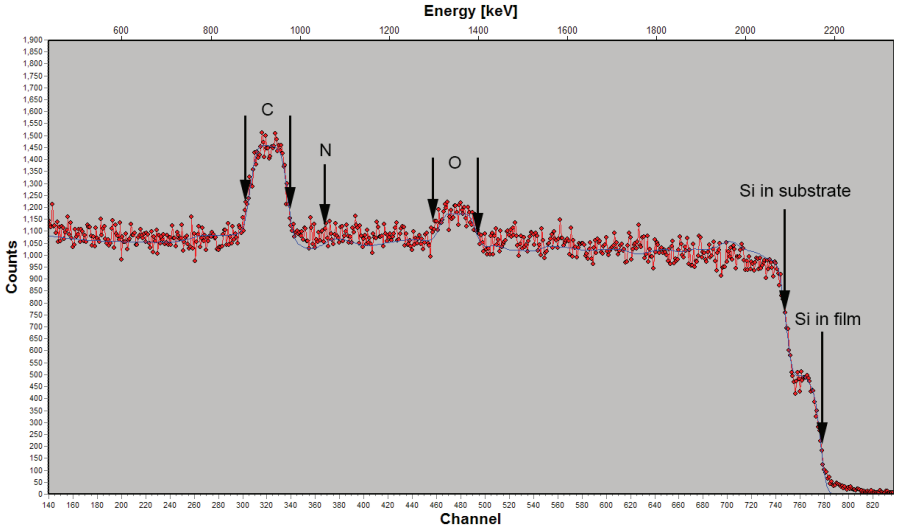

Figure 4.6: A schematic of a SIMNRA RBS spectrum showing the Si, O, C and N related peaks.

The chemical composition of the films heat treated in vacuum are shown in Table 4.1. The chemical composition of the green film is $SiC_{3.4}O_{2.4}H_{8.8}$ from the theoretically analyzed formula $SiO(OC_2H_5)_{1.4}(CH_3)_{0.6}$ discussed above while the chemical composition was determined to be $SiC_{4.4}O_{2.89}H_{5.11}$ from RBS/ERD. Atomic ratios of C/Si, O/Si agree with the theoretical analysis if considering the effects of incomplete hydrolysis and condensation which lead to an increase of

ethoxyl (-OC_2H_5) content. A considerable decrease in the measured H/Si is attributed to the partial decomposition of PVP and other organic components which continues at higher temperature leading to the formation of free carbon. With increasing heat treatment temperature, H content gradually decreased consistent with the decomposition of the organic components observed from FT-IR. In the process of analyzing the chemical composition using SIMNRA, the total number of the specific elemental atoms in the films was also calculated. Knowing the thickness measured by AFM, density of the film can be calculated. Table 4.1 shows the calculated densities of the films heat treated in vacuum at different temperatures. It was shown that the green film had a density of ∼1.0 g/cm^3 while the density estimated from weight gain after coating was reported to be ∼1.3 g/cm^3 [90]. The difference is due to the inaccuracy of the weight gain measurement. As the film was deposited onto the (100) Si wafer, the sol also went to the backside of the Si wafer such that the weight gain and thus film density were overestimated. From Table 4.1 it was seen that the density of the films heat treated below 800 °C was relatively constant. At 800 °C, the density of the film increased by ∼50% in accordance with the decomposition of the organic components and the abrupt increase in the measured hardness and reduced elastic modulus.

Table 4.1: Chemical compositions and densities of the acid catalyzed films heat treated in vacuum at 300 - 800 °C

Temperature (°C)	Si	H	C	N	O	density (g/cm^3)
300.00	1.00	5.11	4.44	0.44	2.89	1.04
400.00	1.00	2.90	2.67	0.39	2.13	1.07
600.00	1.00	1.61	1.30	0.18	1.46	1.07
800.00	1.00	1.62	1.40	0.18	1.86	1.51

4.2.4 Microstructure of Heat Treated Films

The hardness depth profiles as shown in Fig. 4.7 for the 3 μm thick acid catalyzed films heat treated at 300 °C, 700 °C and 800 °C show a decrease with increasing contact depth which might indicate a change in microstructure along the depth. XRD was used to study the microstructure after heat treatment. The depth dependent microstructure can not be quantified with a standard geometry. In the standard geometry the absorption length for X-rays is around 10 μm so that an XRD pattern contains information on the entire thickness of the sol-gel films. As a consequence, the

depth profiles can not be determined with standard geometry configuration [145]. Depth resolved XRD experiments with depth resolution of about 50 nm were performed at Los Alamos National Laboratory. The specimen and the source positions were held fixed while the detector performed 10° - 90° scanning. The investigated depth can be adjusted by rotating the specimen at a small angle, which leads to an increase of about 50 - 75 nm in depth with each degree rotation. For simplicity, 1° rotation of the specimen was considered to be corresponding to a change of about 60 nm in depth (by taking the average). Depth resolved XRD was performed on the 3 μm thick acid catalyzed thick films which had thicknesses of 1713 nm, 727 nm and 706 nm after heat treatment at 300 °C, 700 °C and 800 °C, respectively. The depth resolved XRD patterns are shown in Figs. 4.8, 4.9 and 4.10, in which XRD data were collected at different depths by rotating the specimen 1°, 2°, 3°, 4° and 5°. With the standard geometry XRD patterns with 1 hour scanning only showed a peak at 69.9° which was attributed to the Si substrate for all three specimens. For the specimen heat treated at 300 °C, completely amorphous phases were observed at all the investigated depths. As depth was increased, two small amorphous peaks appeared at 20° - 30° and at 50° - 60°. For the specimens heat treated at 700 and 800 °C, different levels of crystalline phases between 50° - 60° were observed as investigated depth increases. A sharp peak was observed between 56° - 58° when the specimen was fixed at 3° representing an approximate depth of 180 nm. An amorphous peak between 80° - 90° began to grow as depth increased. The observed peaks at different depths might be an indication of a change in microstructure along the depth resulting from heat treatment. However at this point, it was not possible to obtain reliable information about the crystalline phases due to the lack of enough crystalline peaks. As seen in Fig. 4.7, there was a significant decrease in hardness measured at a contact depth of about 150 nm while the sharp peak was observed from the glancing angle XRD collected at a depth of about 180 nm. The decrease in hardness with increasing contact depth can not be attributed to the substrate effect, as the (100) Si substrate had a much higher hardness ($\sim$11 GPa) than these investigated films. There might be a correlation between the development of crystalline phases at this depth and the measured low hardness at the same depth.

XRD experiments performed at glancing angle at OSU [146] on the films heat treated at 1100 and 1350 °C in Ar showed that heat treatment at 1350 °C led to the formation of crystalline silica (cristobalite), and at 1100 °C resulted in an amorphous structure of silica. However, there was no crystalline SiC phase detected from either film which is inconsistent with the observation that crystalline SiC was formed above 1200 °C as a result of phase separation [43, 47–56]. This indicates the free carbon has been oxidized before phase separation despite the Ar flow. The speculation of carbon oxidation also supports that there were no carbon related peaks in the XRD pattern.

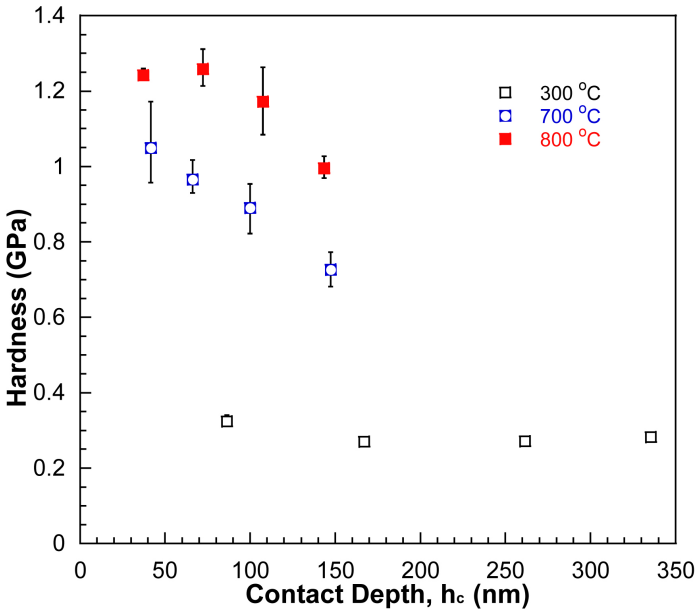

Figure 4.7: Hardness of the acid catalyzed thick films heat treated at 300 °C, 700 °C and 800 °C obtained by nanoindentation.

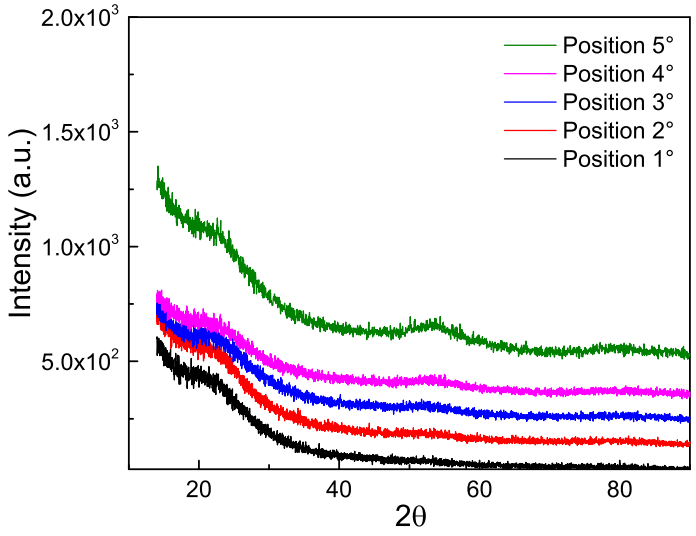

Figure 4.8: Depth resolved XRD patterns collected at different depths by rotating specimen 1°, 2°, 3°, 4° and 5°, corresponding to depths of approximately 60, 120, 180, 240, and 300 nm, for the film heat treated at 300 °C. The intensity is plotted on an absolute scale.

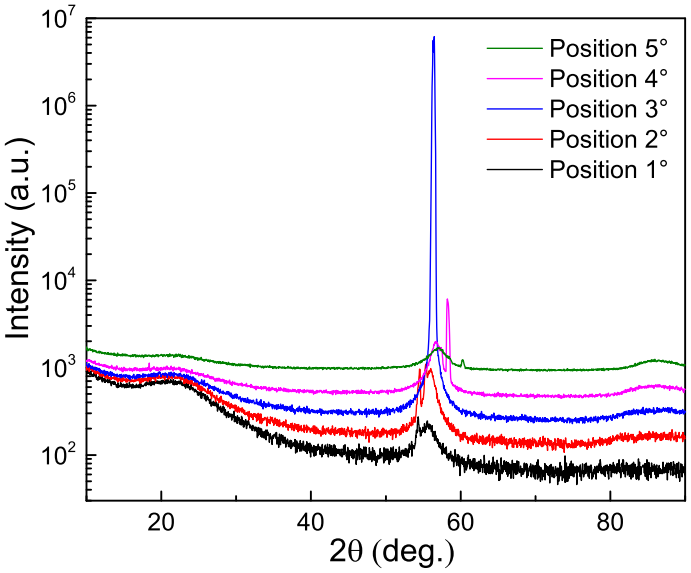

Figure 4.9: Depth resolved XRD patterns collected at different depths by rotating specimen 1°, 2°, 3°, 4° and 5°, corresponding to depths of approximately 60, 120, 180, 240, and 300 nm, for the film heat treated at 700 °C. The intensity is plotted on a logarithmic scale.

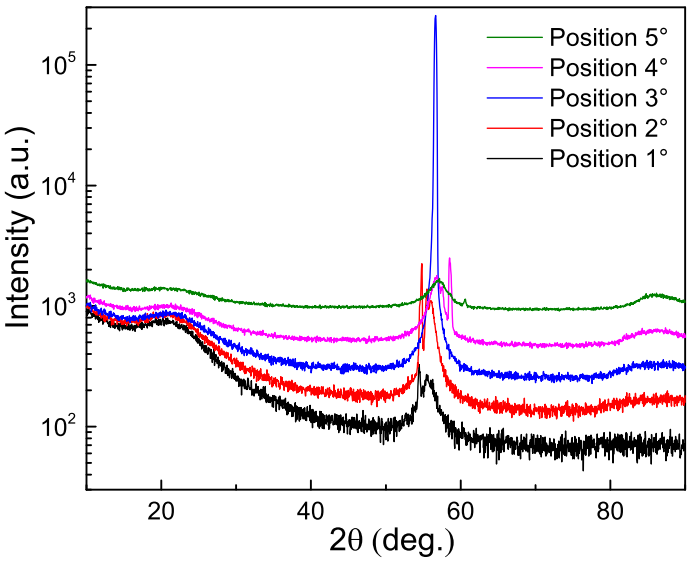

Figure 4.10: Depth resolved XRD patterns collected at different depths by rotating specimen 1°, 2°, 3°, 4° and 5°, corresponding to depths of approximately 60, 120, 180, 240, and 300 nm, for the film heat treated at 800 °C. The intensity is plotted on a logarithmic scale.

4.3 The Effects of Ion Irradiation on the Acid Catalyzed Sol-gel Films

Ion irradiation was carried out at room temperature using 200 keV H^+, 400 keV N^{2+}, 1 MeV Cu^+, 4 MeV Cu^{2+} and 9 MeV Cu^{3+} with fluences from 1×10^{13} to 2×10^{17} ions/cm^2. The film thicknesses of the green films before ion irradiation were measured to be $\sim$1 μm. The detailed conditions of the ion irradiations are presented in Table 3.3. The beam current was adjusted to be less than 0.5 μA/cm^2 for all irradiations in order to avoid thermal effects.

As an energetic ion traverses a solid, it undergoes a series of collisions with the stationary target atoms in which nuclear collisions (elastic collisions) deflect the ion from its initial trajectory, and electronic collisions (inelastic collisions) lead to electron excitation and ionization. As a result of nuclear and electronic collisions, the incident ions lose energy and eventually come to rest. However, the importance of the two energy loss mechanisms varies with the energy (E) and atomic number (Z) of the incident ion. In general, electronic stopping dominates for high E and low Z, while nuclear stopping takes over for low E and high Z. The energy loss rate per distance traveled ($\frac{dE}{dx}$) can be expressed as the summation of the nuclear stopping power ($\frac{dE}{dx}\big|_n$) and the electronic stopping power ($\frac{dE}{dx}\big|_e$). It is noted here that all discussion of the electronic and nuclear stopping powers below is limited to the energy transfer during the collisions between the incident ions and the target atoms and electrons. From the point of view of the whole system, a target atom which obtains a sufficiently high energy from the collision with the incident ion is able to make further interactions with other target atoms and electrons until it comes to rest in the solid. The target atoms during the collisions are called recoiled target atoms or recoils, which also contribute to the electron excitation and ionization.

Simulation of the electronic and nuclear collisions between the energetic incident ion and the film/substrate system is accomplished using SRIM [91]. The target in the simulation is considered to be a 1 μm thick film on a 250 μm thick silicon substrate with an estimated density of 1.0 and 2.3 g/cm^3, respectively. Ions were selected such that there is a broad distribution of electronic and nuclear stopping powers and the projected range is larger than the film thickness in order to fully irradiate the investigated films. Figures 4.11 - 4.15 show simulated depth distributions of electronic and nuclear stopping powers of 200 keV H^+, 400 keV N^{2+}, 1 MeV Cu^+, 4 MeV Cu^{2+} and 9 MeV Cu^{3+} in the investigated thin film/substrate system. A simple approximation of the electronic and nuclear stopping is reported as follows. There are two regimes of the electronic stopping, high-energy

electronic energy loss regime and low-energy electronic energy loss regime, which are determined by the effective charge of the incident ion Z^* defined by

$$\frac{Z^*}{Z_1} = \frac{v}{v_0 Z_1^{2/3}} \tag{4.2}$$

where Z is the atomic number of the incident ion, v is the incident ion velocity, and v_0 is the Bohr velocity. In the high-energy electronic energy loss regime, where the ion velocity is greater than $v_0 Z_1^{2/3}$, the incident ion is a bare nucleus and its interactions with target electrons can be accurately described by a pure Coulomb interaction potential. Considering an incident ion with atomic number Z_1, mass M_1, and velocity v passing through a solid with atomic number Z_2 and mass M_2, the electronic stopping power is described as [134]:

$$\left.\frac{dE}{dx}\right|_e = \frac{4\pi Z_1^2 e^4 N Z_2}{m_e v^2} ln \frac{2 m_e v^2}{10 Z_2} \tag{4.3}$$

where N is the atomic density of the solid, e is the charge of an electron and m_e is the mass of an electron. In the current study, 200 keV H^+ is fully stripped of electrons and is a bare nucleus based on the effective charge defined in Eq. 4.2. The electronic stopping of 200 keV H^+, as shown in Fig. 4.11, exhibits a slight increase with increasing depth in the film consistent with the electronic stopping power being proportional to $ln\frac{2m_e v^2}{10 Z_2}/(m_e v^2)$. At the film-substrate interface, the electronic stopping power increases dramatically as a result of Z_2 changing from the atomic number of the film (5.2 on average) to that of the substrate (14). In the low-energy electronic energy loss regime, where the incident ion moves with velocity $v < v_0 Z_1^{2/3}$, the electronic stopping is described in Eq. 4.4 from the work involved in the transfer of momentum by the Firsov and Lindhard-Scharff models [134]

$$\left.\frac{dE}{dx}\right|_e = 8\pi e^2 a_0 N \frac{Z_1^{7/6} Z_2}{(Z_1^{2/3} + Z_2^{2/3})^{3/2}} \left(\frac{v}{v_0}\right) \tag{4.4}$$

where a_0 is the Bohr radius. The electronic stopping power of all ions except 200 keV H^+ could be described by the Firsov and Lindhard-Scharff models in which the electronic stopping is proportional to the incident ion velocity. As the incident ion passes through the solid, the stopping power decrease with depth as a result of energy loss. At the film-substrate interface, the electronic stopping power increases dramatically due to the difference in Z_2 values of the film and the substrate. The numerical analysis of the nuclear stopping power could be described as [134] :

$$\left.\frac{dE}{dx}\right|_n = \frac{8.462 \times 10^{-15} N Z_1 Z_2 M_1 S_n(\epsilon)}{(M_1 + M_2)(Z_1^{0.23} + Z_2^{0.23})} \frac{\text{eV-cm}^2}{\text{atom}} \tag{4.5}$$

where the nuclear stopping cross section in reduced notation $S_n(\epsilon)$ is given by

$$S_n(\epsilon) = \frac{0.5 ln(1 + 1.1383\epsilon)}{\epsilon + 0.01321\epsilon^{0.21226} + 0.19593\epsilon^{0.5}} \tag{4.6}$$

and the reduced energy ϵ is calculated by

$$\epsilon = \frac{32.53 M_2 (0.5 M_1 v^2)}{Z_1 Z 2 (M_1 + M_2)(Z_1^{0.23} + Z_2^{0.23})} \tag{4.7}$$

The nuclear stopping power of all the ions increase with depth until a maximum, then quickly decrease. The averaged electronic and nuclear stopping powers summarized in Table 4.2 are calculated by taking the average of the electronic and nuclear stopping powers over the film thickness. The projected range of each investigated ion is also shown. For 200 keV H^+ and 400 keV N^{2+}, the electronic stopping power is dominant. The electronic stopping power of 1 MeV Cu^+ is about 10 eV/Å-ion higher than that of 400 keV N^{2+} while the nuclear stopping is about 30 eV/Å-ion higher. With increasing energy of the Cu ions, the nuclear stopping power decreases but the electronic and total stopping power (electronic + nuclear stopping) increases, representing an energy loss process dominated by electronic stopping.

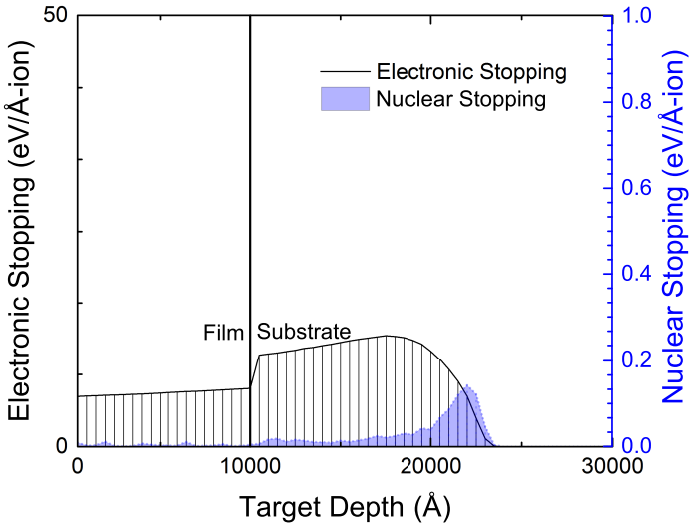

Figure 4.11: Depth distribution of the electronic stopping and nuclear stopping of 200 keV H^+ in the investigated thin film/substrate system.

4.3.1 Effects of Ion Fluence on Film Shrinkage and Mechanical Properties

The film shrinkage from ion irradiation was measured as a function of fluence for the different ions used in this study. Figure 4.16 shows the film shrinkage of the acid catalyzed films after irradiations with 200 keV H^+, 400 keV N^{2+}, 1 MeV Cu^+, 4 MeV Cu^{2+} and 9 MeV Cu^{3+} at fluences of 1×10^{13} to 2×10^{17} ions/cm^2. For each ion species, film shrinkage increased with increasing fluence and approached a relative constant value at high fluence. Ion irradiations at a fluence of

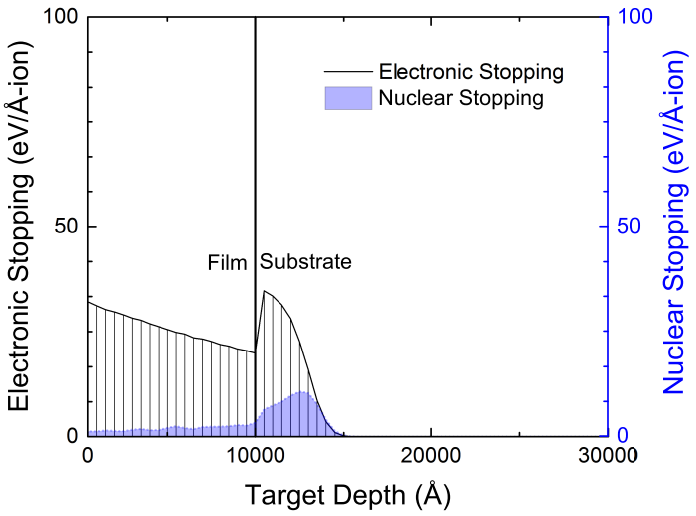

Figure 4.12: Depth distribution of the electronic stopping and nuclear stopping of 400 keV N^{2+} in the investigated thin film/substrate system.

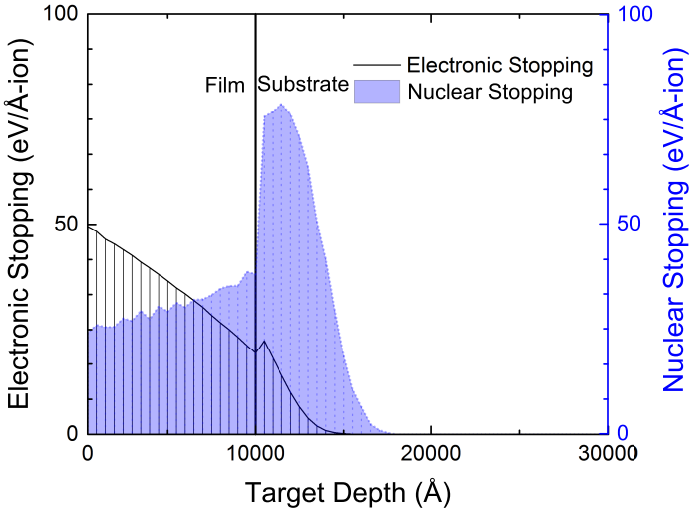

Figure 4.13: Depth distribution of the electronic stopping and nuclear stopping of 1 MeV Cu^{+} in the investigated thin film/substrate system.

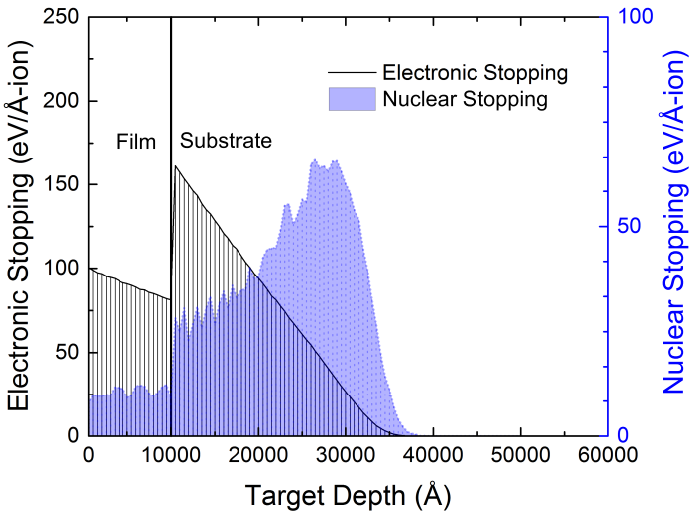

Figure 4.14: Depth distribution of the electronic stopping and nuclear stopping of 4 MeV Cu^{2+} in the investigated thin film/substrate system.

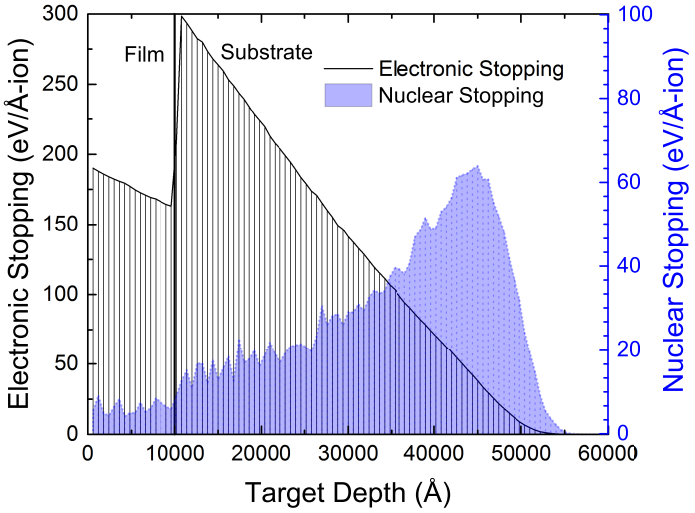

Figure 4.15: Depth distribution of the electronic stopping and nuclear stopping of 9 MeV Cu^{3+} in the investigated thin film/substrate system.

Table 4.2: Average electronic and nuclear stopping powers, and the projected ranges of 200 keV H^+, 400 keV N^{2+}, 1 MeV Cu^+, 4 MeV Cu^{2+} and 9 MeV Cu^{3+} in the acid catalyzed sol-gel films.

	200 keV H^+	400 keV N^{2+}	1 MeV Cu^{1+}	4 MeV Cu^{2+}	9 MeV Cu^{3+}
Electronic Stopping (eV/Å-ion)	6.2	25.5	35.3	90.5	234.0
Nuclear Stopping (eV/Å-ion)	0	2.0	30.8	10.5	8.9
Electronic + Nuclear (eV/Å-ion)	6.2	27.5	66.1	101.0	242.9
Projected Range (μm)	2.20	1.28	1.30	3.06	4.70

1×10^{13} ions/cm^2 resulted in a negligible change in the film thickness regardless of the ion species and the electronic and nuclear stopping powers. At fluences of 10^{14} ions/cm^2 or above, the shrinkage was observed to increase with the increasing stopping power (in the order of 200 keV H^+, 400 keV N^{2+}, 1 MeV Cu^+, 4 MeV Cu^{2+} and 9 MeV Cu^{3+}). A maximum of ~80% shrinkage was obtained with 9 MeV Cu^{3+} at fluences of 1×10^{15} and 1×10^{16} ions/cm^2, and with 4 MeV Cu^{2+} at a fluence of 1×10^{16} ions/cm^2. This suggests the conversion from the polymer to a ceramic state is complete and any further increase in fluence would have no further effect on the film shrinkage. For the other ions, it is unclear if a maximum shrinkage was achieved with the highest fluence used. A further increase in the fluence may result in additional film shrinkage. As a comparison, the film heat treated at 800 °C in vacuum had a shrinkage of 48%.

In addition, the film shrinkage was compared with similar films which were synthesized with the same starting materials and irradiated with 125 keV H^+ and 250 keV N^{2+} [17]. The nominal thickness of the green films used in the previous study was 600 nm. The electronic and nuclear stopping powers were reported to be 6.4 and 0 eV/Å-ion for 125 keV H^+, and 24.9 and 1.9 eV/Å-ion for 250 keV N^{2+} [17]. Figure 4.17 shows film shrinkage of the 1 μm thick acid catalyzed films irradiated with 200 keV H^+ and 400 keV N^{2+}, and the 600 nm thick acid catalyzed films irradiated with 125 keV H^+ and 250 keV N^{2+} as a function of fluence. Despite the energy difference, there was no difference in the stopping powers of the same ion species. There was also no distinct difference observed in the film shrinkage for the 600 nm thick and 1 μm thick films irradiated with the same

ions at the same fluence regardless of the energy difference.

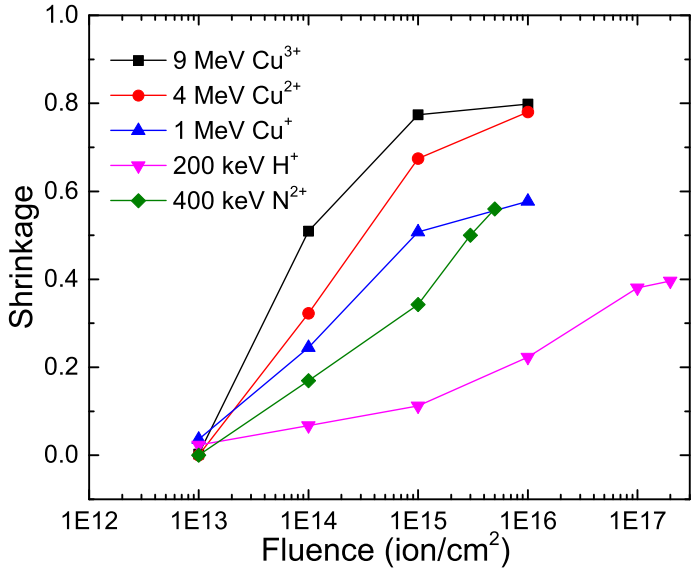

Figure 4.16: Film shrinkage of the acid catalyzed films irradiated with 200 keV H^+, 400 keV N^{2+}, 1 MeV Cu^+, 4 MeV Cu^{2+} and 9 MeV Cu^{3+} as a function of fluence.

Characterization of the mechanical properties of such thin films converted by ion irradiation is difficult as the measured hardness and reduced elastic modulus can be significantly affected by the Si substrate. Figure 4.18 shows the hardness and reduced elastic modulus of the acid catalyzed films irradiated with 200 keV H^+, 400 keV N^{2+}, 1 MeV Cu^+, 4 MeV Cu^{2+} and 9 MeV Cu^{3+} at fluences of 1×10^{13} to 2×10^{17} ions/cm^2 as a function of contact depth. Also shown are the measured properties of the green film and the (100) Si substrate. It can be seen that as the film thickness decreases the reduced elastic modulus significantly increases with increasing contact depth which indicates a strong substrate effect. The effect of the substrate on the measured hardness at the same contact depth may not be as pronounced as for the reduced elastic modulus which shows a significant effect as a result of the elastic field under the indenter not being confined to the film itself but extending into the substrate [125]. In order to validate the 10% rule on the elastic modulus measurements, the Doerner and Nix's model [121] detailed in Chapter 3 was employed to extract the elastic modulus. Since the Poisson's ratio of the thin film is unknown, a modified elastic modulus (M) defined as $\frac{E_f}{1-\nu_f^2}$ was obtained by fitting the experimental data using the discussed model, where E_f and ν are the elastic modulus and Poisson's ratio of the thin film. The properties of the (100) Si substrate used in this approach were 0.32 for Poissons ratio and an elastic modulus of 169 GPa [147]. In order to compare with the experimental results, the modified elastic modulus

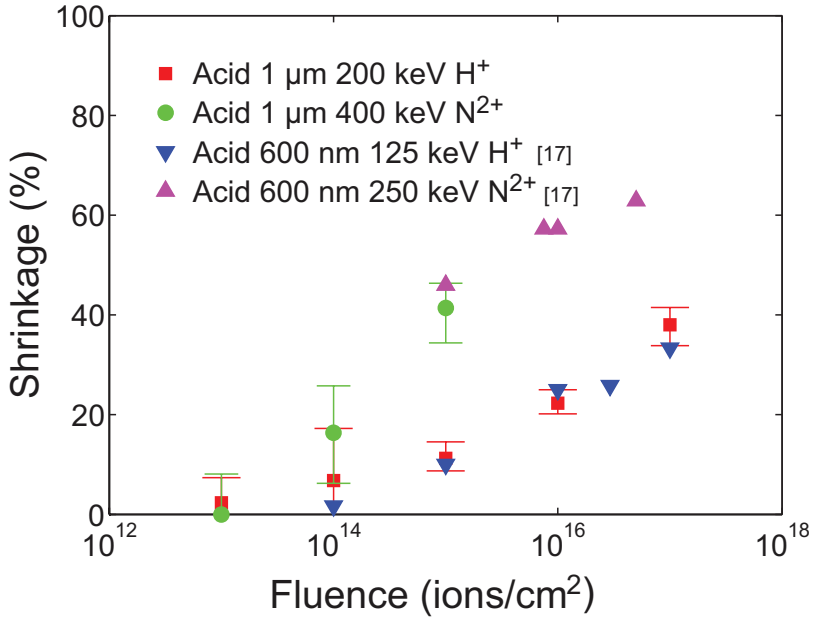

Figure 4.17: Film shrinkage of 1 μm thick acid catalyzed films irradiated with 200 keV H^+ and 400 keV N^{2+}, and 600 nm thick acid catalyzed films irradiated with 125 keV H^+ and 250 keV N^{2+} as a function of fluence.

is converted to the reduced elastic modulus through Eq. 3.3. Figure 4.19 shows a direct comparison of the reduced elastic modulus measured at a contact depth/thickness ratio of 10% and the reduced elastic modulus obtained from the model for all the ion irradiated films. The maximum error observed is ~10% therefore it is reasonable to evaluate the reduced elastic modulus with the 10% rule. For the evaluation of indentation hardness, the 10% rule is still the most commonly used methodology in determining the hardness of the thin films.

The measured hardness and reduced elastic modulus of the acid catalyzed films irradiated with 200 keV H^+, 400 keV N^{2+}, 1 MeV Cu^+, 4 MeV Cu^{2+} and 9 MeV Cu^{3+} as a function of fluence are shown in Fig. 4.20. The dashed line indicates the mechanical properties of fused silica having a nanoindentation hardness of 9.2 GPa and reduced elastic modulus of 69.6 GPa. Ion irradiation at a fluence of 1×10^{13} ions/cm^2 had a negligible effect on the increase of the measured hardness and reduced elastic modulus regardless of the ion species and electronic and nuclear stopping powers. After irradiation with a fluence of 1×10^{14} ions/cm^2, there was a slight increase in the hardness and reduced elastic modulus over that of the green film. At this fluence, hardness and reduced elastic modulus both increased with increasing total stopping power, which became more pronounced at higher fluence. For each specific ion, the hardness and reduced elastic modulus increased with the

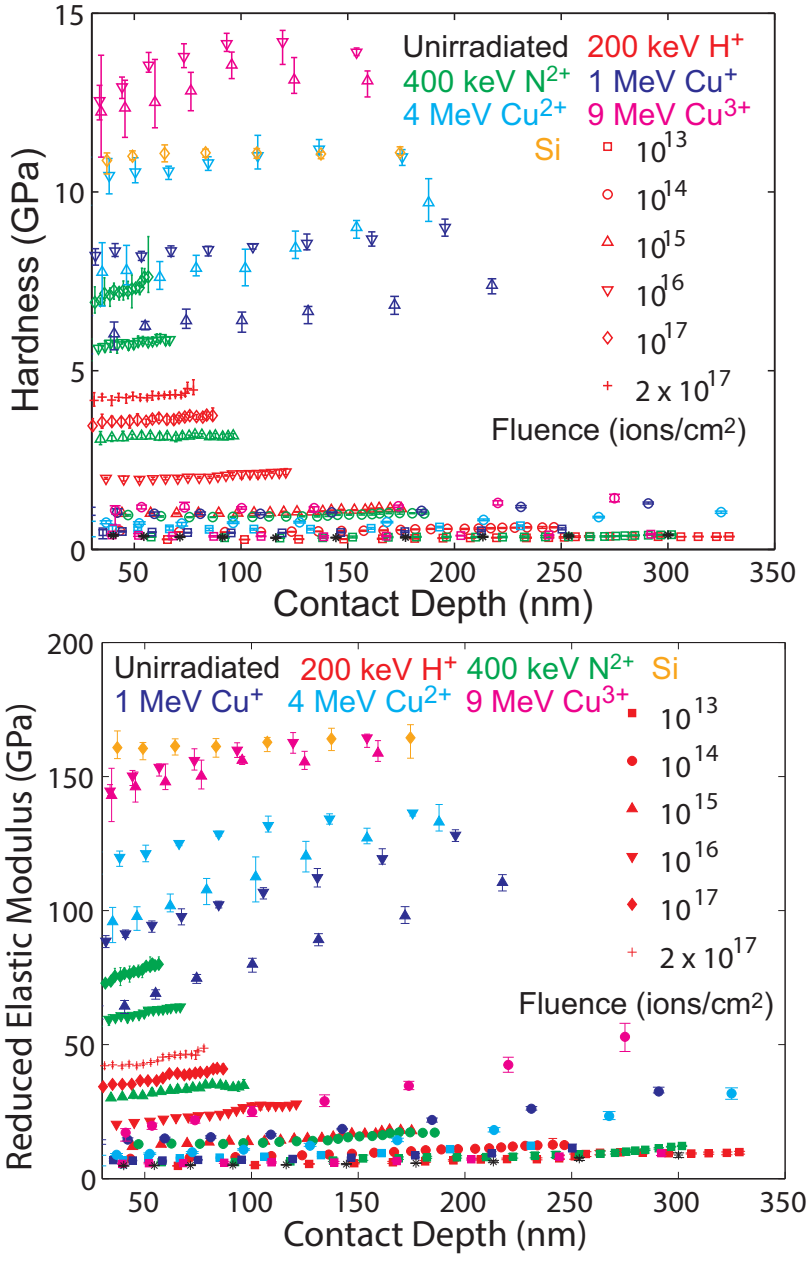

Figure 4.18: Hardness and reduced elastic modulus of the acid catalyzed films irradiated with 200 keV H^+, 400 keV N^{2+}, 1 MeV Cu^+, 4 MeV Cu^{2+} and 9 MeV Cu^{3+} at fluences of 1×10^{13} to 2×10^{17} ions/cm^2 as a function of contact depth. Also shown are the properties of the green film and the (100) Si substrate.

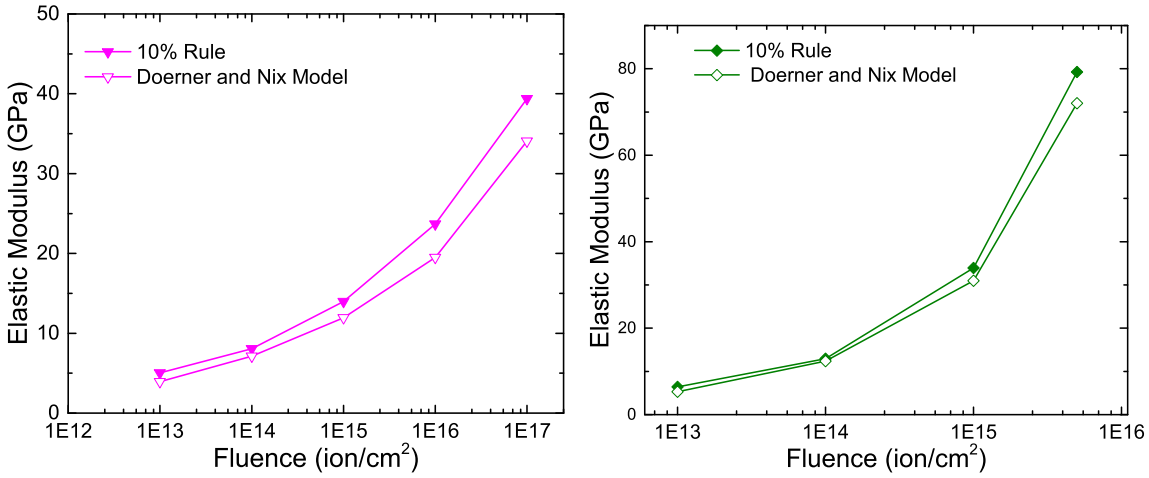

(a) 200 keV H^+

(b) 400 keV N^{2+}

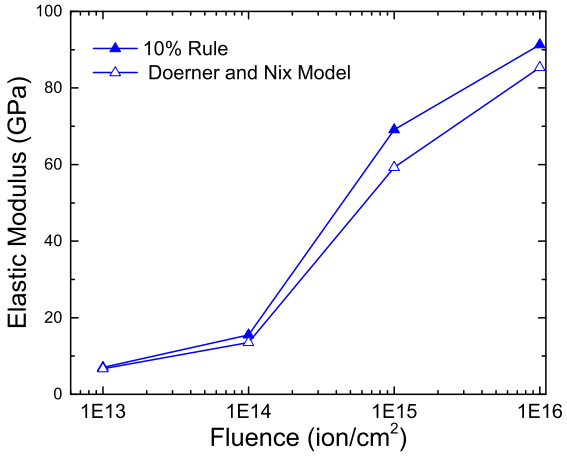

(c) 1 MeV Cu^+

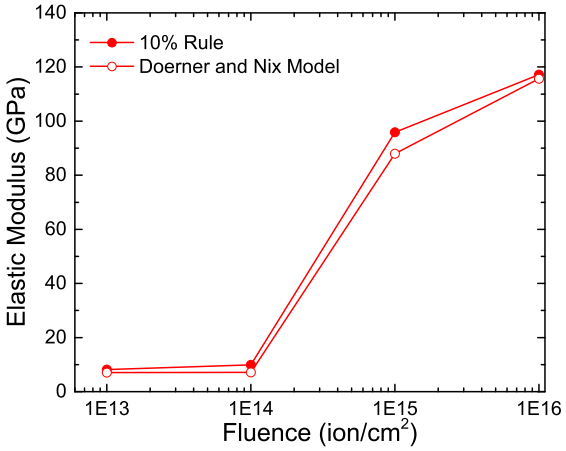

(d) 4 MeV Cu^{2+}

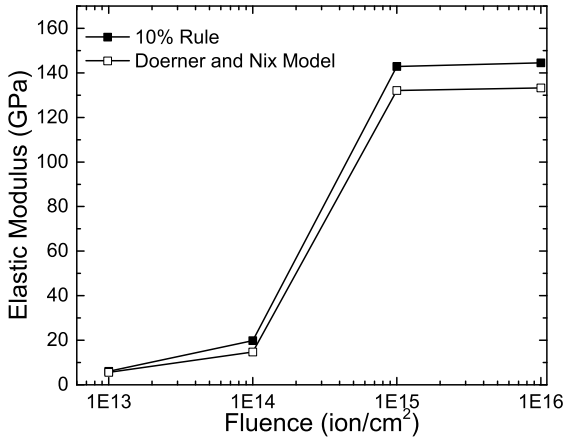

(e) 9 MeV Cu^{3+}

Figure 4.19: Direct comparison of the reduced elastic modulus of the acid catalyzed films irradiated with 200 keV H^+, 400 keV N^{2+}, 1 MeV Cu^+, 4 MeV Cu^{2+} and 9 MeV Cu^{3+} obtained from the 10% rule and the Doerner and Nix's Model.

increasing fluence, except for the film irradiated with 9 MeV Cu^{3+}, which reached a maximum hardness of ~12 GPa and reduced elastic modulus of ~142 GPa at a fluence of 1×10^{15} ions/cm^2, and remained constant with further increase in fluence. This agreed with the results for the shrinkage. Films irradiated at a fluence above 1×10^{14} ions/cm^2 showed increases in hardness and reduced elastic modulus depending on the fluence and stopping power. Films irradiated with a fluence above 1×10^{14} ions/cm^2 (or 1×10^{15} ions/cm^2 for H^+) had a higher hardness and reduced elastic modulus than the film heat treated at 800 °C in ambient air or in vacuum, which had a hardness of 1.2 GPa and reduced elastic modulus of 19 GPa. The film heat treated in Ar had a comparable reduced elastic modulus with fused silica while the film irradiated with 9 MeV Cu^{3+} at a fluence of 1×10^{15} ions/cm^2 or above exhibited a two-fold increase over that for fused silica.

As mentioned previously, irradiations with H^+, N^{2+} and Cu^{2+} were performed on 600 nm thick films in the previous study [17]. There was a negligible difference in the measured hardness and reduced elastic modulus resulting from H^+ (or N^{2+}) irradiation at the same fluence in the previous and current study as shown in Fig. 4.21. However, this was not the case for Cu irradiation. The measured hardness and reduced elastic modulus of the films irradiated with 1 MeV Cu^+, 2 MeV Cu^{2+}, 4 MeV Cu^{2+} or 9 MeV Cu^{3+} as a function of fluence are shown in Fig. 4.22. Films irradiated with 4 MeV Cu^{2+} or 9 MeV Cu^{3+} exhibited a higher hardness and reduced elastic modulus than those irradiated with 1 MeV Cu^+ or 2 MeV Cu^{2+} at the same fluence. Films irradiated with 2 MeV Cu^{2+} showed a slightly lower hardness and reduced elastic modulus than those irradiated with 1 MeV Cu^+ when irradiated at low fluences (1×10^{15} ions/cm^2 or lower), and comparable hardness and higher reduced elastic modulus when irradiated at high fluences (above 3×10^{15} ions/cm^2). The electronic stopping of 2 MeV Cu^{2+} in the 600 nm thick films was calculated to be 61.2 eV/Å-ion (~75% higher than that of 1 MeV Cu^+ in the present study) while the total stopping was 76.7 eV/Å-ion (only ~15% higher than that of 1 MeV Cu^+) [17]. It is expected that the film irradiated with 2 MeV Cu^{2+} would have similar or even a higher hardness and reduced elastic modulus as a result of slightly higher total stopping power. The reason for lower hardness and reduced elastic modulus when irradiated with 2 MeV Cu^{2+} at low fluence is unclear. The difference in the chemical composition and film thickness of the green films can not be excluded.

Although the increase in hardness and reduced elastic modulus of the ion irradiated films was accompanied by an increase of film shrinkage, the relationship between film shrinkage and the measured hardness and reduced elastic modulus is still unclear. Pivin's group investigated the hardness of several polysiloxanes after various ion irradiations and stated that the hardness was linearly dependent on the film shrinkage [7,8]. However this conclusion is not consistent with the results of the

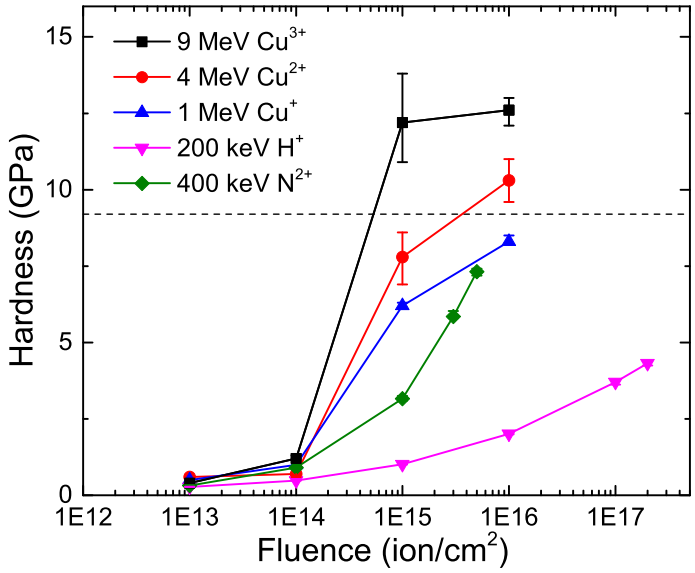

(a) Hardness

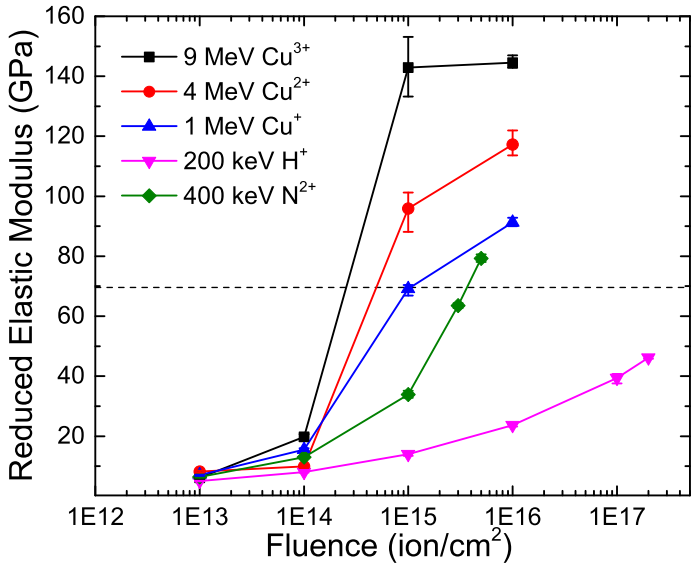

(b) Reduced elastic modulus

Figure 4.20: Plots of (a) hardness and (b) reduced elastic modulus of the acid catalyzed films irradiated with 200 keV H^+, 400 keV N^{2+}, 1 MeV Cu^+, 4 MeV Cu^{2+} and 9 MeV Cu^{3+} as a function of fluence.

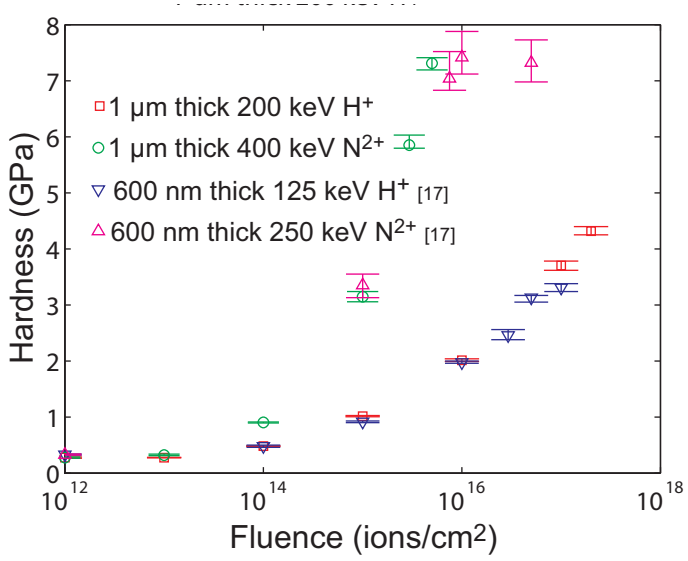

(a) Hardness

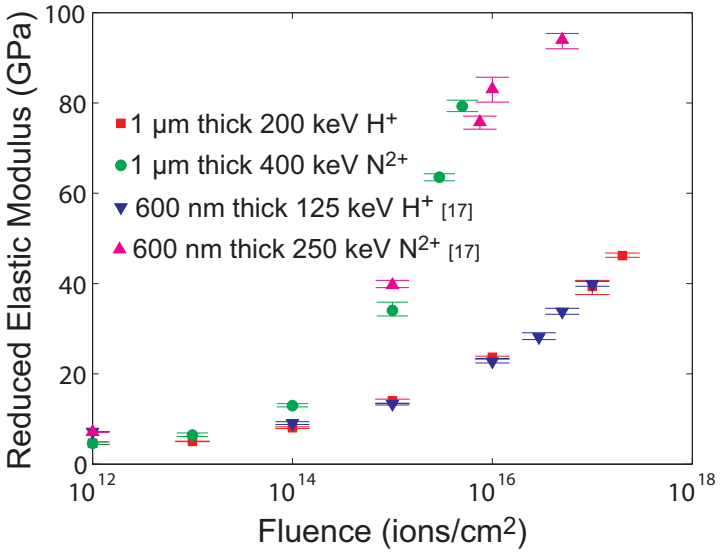

(b) Reduced elastic modulus

Figure 4.21: Plots of (a) hardness and (b) reduced elastic modulus of 1 μm thick acid catalyzed films irradiated with 200 keV H^+ and 400 keV N^{2+}, and 600 nm thick acid catalyzed films irradiated with 125 keV H^+ and 250 keV N^{2+} as a function of fluence.

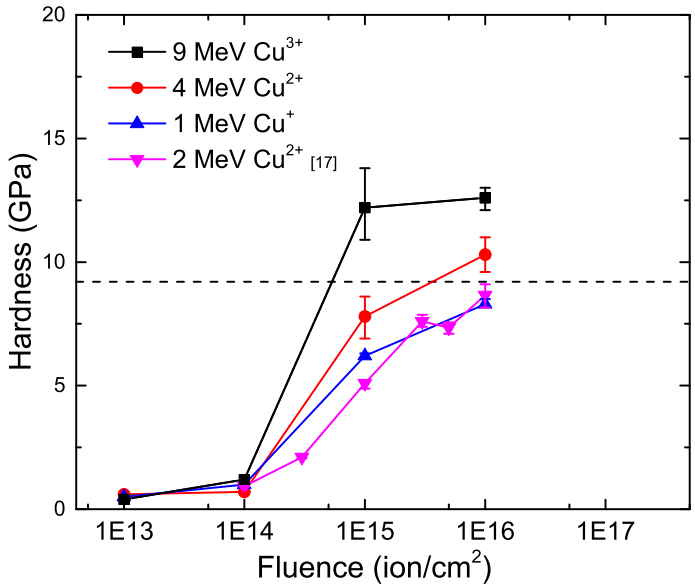

(a) Hardness

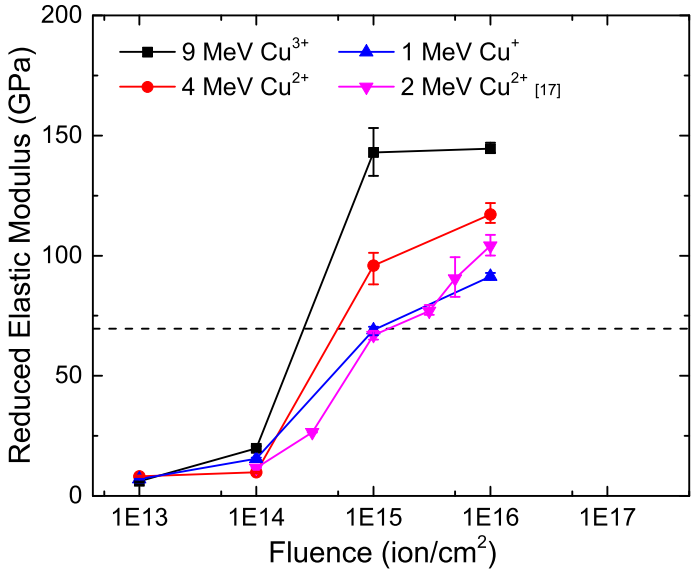

(b) Reduced elastic modulus

Figure 4.22: Plots of (a) hardness and (b) reduced elastic modulus of 1 μm thick acid catalyzed films irradiated with 1 MeV Cu^{+}, 4 MeV Cu^{2+}, or 9 MeV Cu^{3+}, and 600 nm thick acid catalyzed films irradiated with 2 MeV Cu^{2+} as a function of fluence.

present study. Because of the lack of details regarding the preparation process and the treatment of the green films in their experiments, it is not possible to explain this disagreement. A possible explanation might include the difference in the degree of the hydrolysis and condensation, and the nature of the chemical structure of the green films. Figure 4.23 shows the hardness and reduced elastic modulus of the acid catalyzed films irradiated with 200 keV H^+, 400 keV N^{2+}, 1 MeV Cu^+, 4 MeV Cu^{2+} and 9 MeV Cu^{3+} as a function of film shrinkage. Ion irradiation with a fluence of 1×10^{13} ions/cm^2 resulted in no measurable change in the film shrinkage and mechanical properties as previously stated. At a fluence of 1×10^{14} ions/cm^2, there was a wide distribution of film shrinkage from 7% to 51% while there was a minor change in the mechanical properties. The film irradiated with 9 MeV Cu^{3+} at a fluence of 1×10^{14} ions/cm^2 had a film shrinkage of 51% and a hardness of 1.2 GPa compared with 0.3 GPa for the green film. At higher fluences, the increase in the mechanical properties was strongly associated with film shrinkage. For example, with increasing fluence from 1×10^{14} to 1×10^{15} ions/cm^2, irradiation with 9 MeV Cu^{3+} resulted in an increase in film shrinkage from 51% to 77%, and an increase of ∼11 GPa in measured hardness and ∼123 GPa in reduced elastic modulus. When irradiated at a fluence above 1×10^{14} ions/cm^2, the measured hardness and reduced elastic modulus was consistent with the stopping power of the incident ions at the same fluence. In general the significance of ion irradiation on the increase of the mechanical properties started at a fluence of 1×10^{14} ions/cm^2.

4.3.2 Ion Irradiation Induced Changes of Chemical Composition

As discussed the increase in mechanical properties as a result of ion irradiation varies with ion species and stopping power. Figure 4.24 shows hydrogen atomic concentration of the acid catalyzed films irradiated with 200 keV H^+, 400 keV N^{2+}, 1 MeV Cu^+, 4 MeV Cu^{2+} and 9 MeV Cu^{3+} as a function of fluence. Also shown is the hydrogen atomic concentration of the films heat treated in vacuum as a function of temperature. Hydrogen concentration was observed to decrease with increasing fluence for each ion species while the H release rate per fluence increased with increasing the electronic stopping power. The H concentration of the film irradiated with 9 MeV Cu^{3+}, which resulted in the highest H release rate, reached a minimum of ∼4% at a fluence of 1×10^{15} ions/cm^2. Further increase in the fluence led to a negligible change in the H concentration. The films irradiated with other ions were considered to approach a similar final H concentration with different H release rates determined by the stopping power. In addition to ion irradiation, vacuum heat treatment at 800 °C for 30 min led to a H concentration of 27%, a 10% decrease from that of the green film.

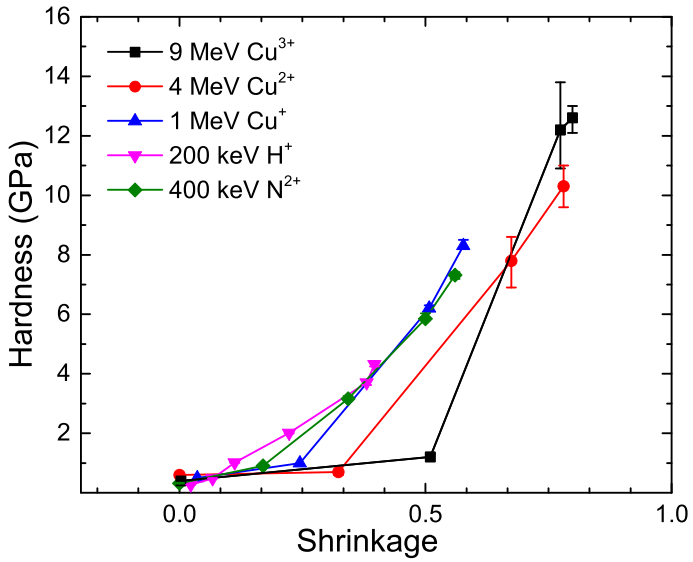

(a) Hardness

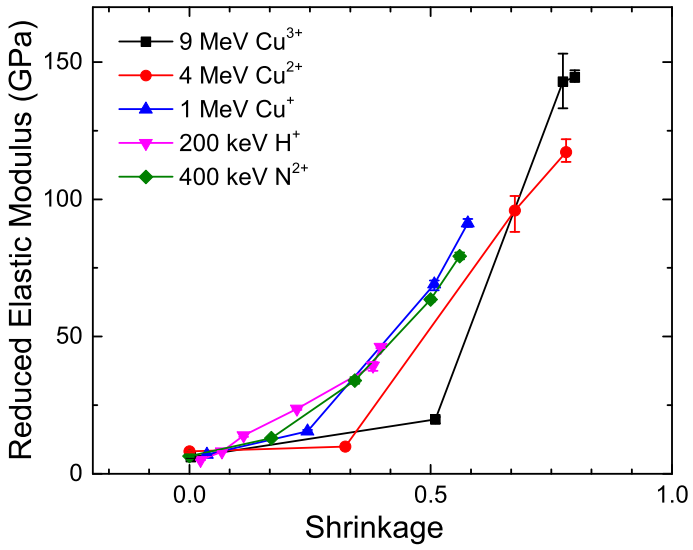

(b) Reduced elastic modulus

Figure 4.23: Plots of (a) hardness and (b) reduced elastic modulus of the acid catalyzed films irradiated with 200 keV H^+, 400 keV N^{2+}, 1 MeV Cu^+, 4 MeV Cu^{2+} and 9 MeV Cu^{3+} as a function of film shrinkage.

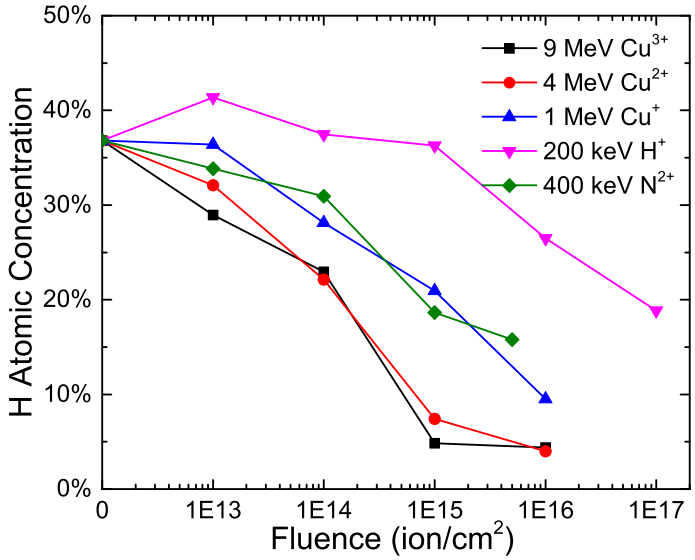

(a) Ion irradiated films

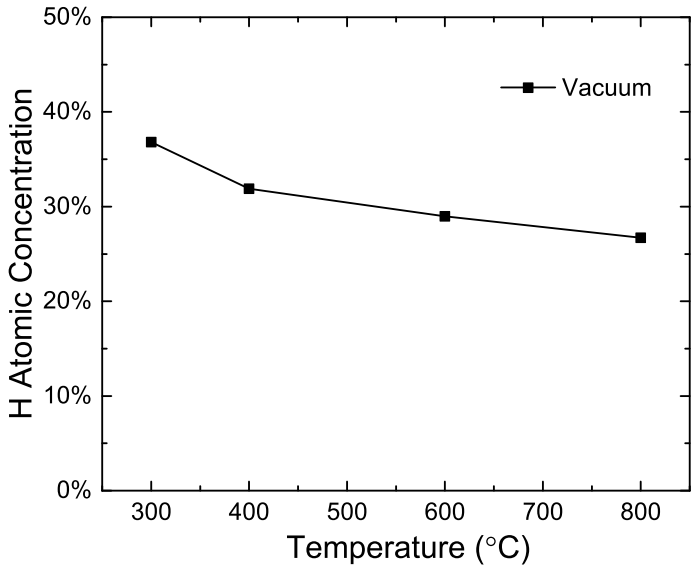

(b) Vacuum heat treated films

Figure 4.24: Hydrogen concentration of the acid catalyzed films (a) irradiated with 200 keV H^+, 400 keV N^{2+}, 1 MeV Cu^+, 4 MeV Cu^{2+} and 9 MeV Cu^{3+} as a function of fluence, and (b) heat treated in vacuum as a function of temperature.

H_2 release was reported in the literature as a result of the ion irradiation of polymers [148–150]. However, H_2 may not be the only outgoing gas from ion irradiation, since other volatile species are also possible. It was reported that the chemical nature of the gases from the ion irradiation of polymers corresponded to the chemical nature of the side groups in the chain. No side group led to mainly a release of H_2, CH_3-groups led to the release of CH_4 and H_2, and chains containing heteroatoms in the side groups may also release gases like CO, CO_2 [151]. Figure 4.25 shows atomic ratios of the acid catalyzed films irradiated with 200 keV H^+, 400 keV N^{2+}, 1 MeV Cu^+, 4 MeV Cu^{2+} and 9 MeV Cu^{3+} as a function of fluence, and the films heat treated in vacuum as a function of temperature. It can be seen that not only the H/Si ratio, but also the C/Si and O/Si ratios decreased with increasing fluence consistent with gas release corresponding to the chemical nature of the side groups. Side groups of -O-C_2H_5 and -CH_3 were present in our investigated green films. To the best of our knowledge, the loss of O in silicon-based polymers under ion irradiation has not been reported. A possible explanation might be the rich H_2O content significantly reduced the amount of -O-C_2H_5 through hydrolysis resulting in the elimination of -O-C_2H_5 in the green films. The ratio of H/Si decreased faster with increasing fluence than C/Si and O/Si and approached a lower final value. Figure 4.26 shows H/Si, C/Si and O/Si ratios as a function of fluence for different ions used. The ratio of H/Si approached a constant of ∼0.14 with 4 MeV Cu^{2+} at a fluence of 1×10^{16} ions/cm^2 and 9 MeV Cu^{3+} at a fluence of 1×10^{15} ions/cm^2 or above, while the ratio for the other ion irradiations showed a continuous decrease with increasing fluence towards the final value. This indicates that the final H concentration may be solely dependent on the chemical nature of the films. In contrast with the final H content, C/Si approached a constant of about ∼3.0 for irradiations with 200 keV H^+, 400 keV N^{2+} and 1 MeV Cu^+, and of about ∼1.0 for irradiations with 4 MeV Cu^{2+} and 9 MeV Cu^{3+}. The ratio of O/Si remained relatively constant for irradiations with 200 keV H^+ and 400 keV N^{2+}, and kept decreasing for Cu ions approaching a minimum of ∼0.7.

Chemical composition and calculated densities for the green film and all of the ion irradiated films are shown in Table 4.3. A plot of density as a function of ion fluence for all used ions is shown in Fig. 4.27. In general, the film density increased with increasing fluence for each ion species. The films irradiated at a fluence of 1×10^{13} ions/cm^2 had no change in density compared to the green film which had a density of ∼1.0 g/cm^3. The film irradiated with 200 keV H^+ had a much slower increase in density with increasing fluence when compared to the other ions. Films irradiated with 4 MeV Cu^{2+} and 9 MeV Cu^{3+} at the highest fluence had a density of 2.3 - 2.5 g/cm^3.

Figure 4.28 shows the hardness and reduced elastic modulus of the acid catalyzed films irradiated

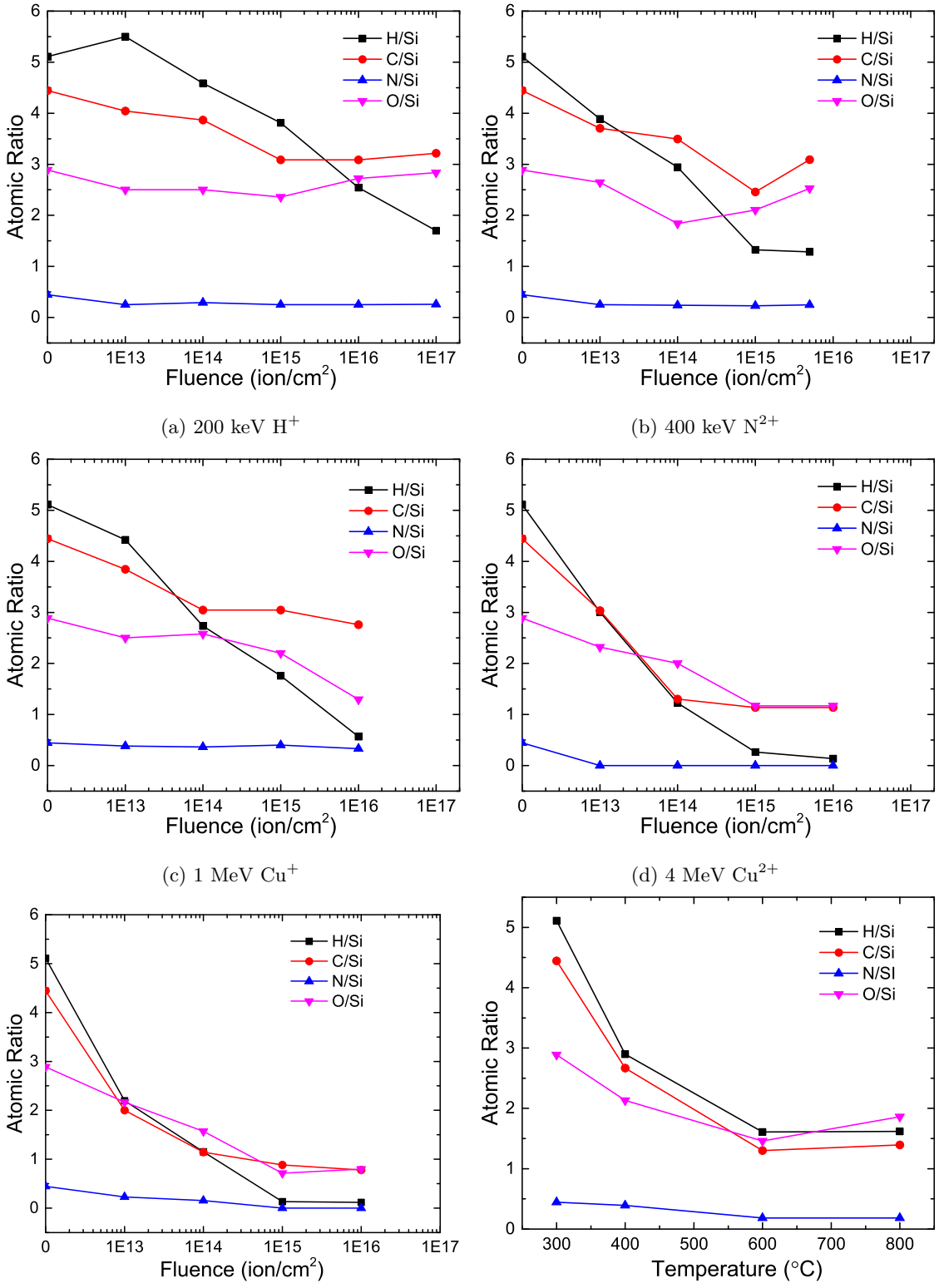

(a) 200 keV H^+

(b) 400 keV N^{2+}

(c) 1 MeV Cu^+

(d) 4 MeV Cu^{2+}

(e) 9 MeV Cu^{3+}

(f) Vacuum Heat Treatment

Figure 4.25: Atomic ratios of the acid catalyzed films (a) irradiated with 200 keV H^+, (b) 400 keV N^{2+}, (c) 1 MeV Cu^+, (d) 4 MeV Cu^{2+} and (e) 9 MeV Cu^{3+} as a function of fluence, and (f) heat treated in vacuum as a function of temperature.

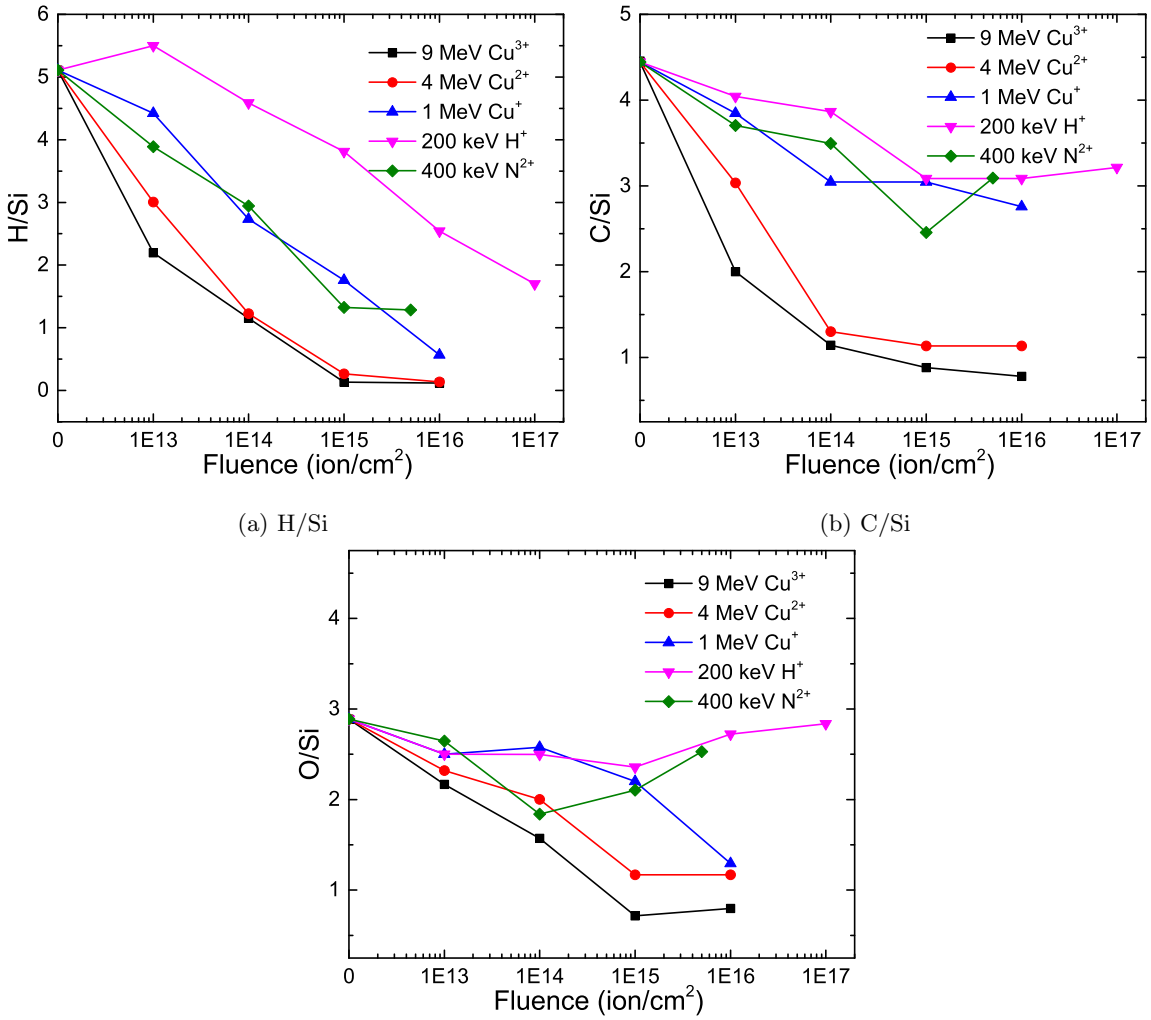

(a) H/Si

(b) C/Si

(c) O/Si

Figure 4.26: Atomic ratios of (a) H/Si, (b) C/Si and (c) O/Si of the acid catalyzed films irradiated with 200 keV H^+, 400 keV N^{2+}, 1 MeV Cu^+, 4 MeV Cu^{2+} and 9 MeV Cu^{3+} as a function of fluence.

Table 4.3: Chemical composition and density of the acid catalyzed films irradiated with 200 keV H^+, 400 keV N^{2+}, 1 MeV Cu^+, 4 MeV Cu^{2+} and 9 MeV Cu^{3+} at varying fluences.

Ion	Fluence	Si	H	C	N	O	Density (g/cm^3)
Unirradiated	0	1.00	5.11	4.44	0.44	2.89	1.04
9 MeV Cu^{3+}	1.0E+13	1.00	2.20	2.00	0.23	2.17	0.99
	1.0E+14	1.00	1.15	1.14	0.16	1.57	1.51
	1.0E+15	1.00	0.13	0.88	0.00	0.72	2.34
	1.0E+16	1.00	0.12	0.78	0.00	0.80	2.29
4 MeV Cu^{2+}	1.0E+13	1.00	3.00	3.04	0.00	2.32	1.00
	1.0E+14	1.00	1.22	1.30	0.00	2.00	1.22
	1.0E+15	1.00	0.26	1.14	0.00	1.17	2.00
	1.0E+16	1.00	0.14	1.14	0.00	1.17	2.47
1 MeV Cu^+	1.0E+13	1.00	4.42	3.85	0.38	2.50	1.11
	1.0E+14	1.00	2.73	3.05	0.36	2.58	1.37
	1.0E+15	1.00	1.76	3.05	0.40	2.20	1.85
	1.0E+16	1.00	0.57	2.76	0.33	1.29	2.06
400 keV N^{2+}	1.0E+13	1.00	3.89	3.70	0.25	2.65	1.11
	1.0E+14	1.00	2.94	3.49	0.24	1.84	1.06
	1.0E+15	1.00	1.33	2.46	0.23	2.11	1.47
	5.0E+15	1.00	1.29	3.09	0.25	2.53	2.09
200 keV H^+	1.0E+13	1.00	5.50	4.04	0.25	2.50	1.12
	1.0E+14	1.00	4.59	3.87	0.29	2.50	1.21
	1.0E+15	1.00	3.81	3.09	0.25	2.36	1.10
	1.0E+16	1.00	2.54	3.09	0.25	2.72	1.31
	1.0E+17	1.00	1.70	3.21	0.26	2.84	1.51

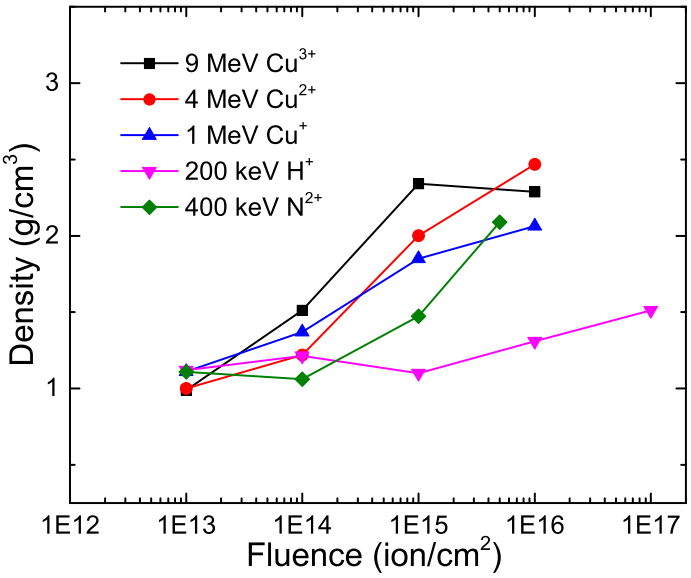

Figure 4.27: Density of the acid catalyzed films irradiated with 200 keV H^+, 400 keV N^{2+}, 1 MeV Cu^+, 4 MeV Cu^{2+} and 9 MeV Cu^{3+} as a function of fluence.

with 200 keV H^+, 400 keV N^{2+}, 1 MeV Cu^+, 4 MeV Cu^{2+} and 9 MeV Cu^{3+} as a function of film density. Also shown are the films heat treated in vacuum. In general, the hardness and reduced elastic modulus increased with increasing film density. This is because the film density indicates the progress of the conversion of the polymer to a ceramic.

4.3.3 Effects of Stopping Power and Deposited Energy on the Mechanical Properties and Hydrogen Concentration

It has been claimed and is generally accepted that the improvements in the surface mechanical properties of polymer are largely due to the formation of a three-dimensionally connected network formed through cross-linking of polymer chains [152]. Cross-linking produces chemical bonds, increase the interconnectivity, thus improving the hardness and reduced elastic modulus. Chain scission reduces the mechanical properties. However, during ion irradiation both cross-linking and scission occur simultaneously. Both electronic and nuclear stopping contribute to cross-linking, as well as chain scission, thus affecting the resulting mechanical properties [153, 154]. Pivin stated that electronic stopping is more efficient than nuclear stopping for increasing the mechanical properties, and the latter does not have the detrimental effect at least for the studied polymers [71]. Some investigations have shown that hardness increased with increasing electronic stopping, but decreased with increasing nuclear stopping [155, 156].

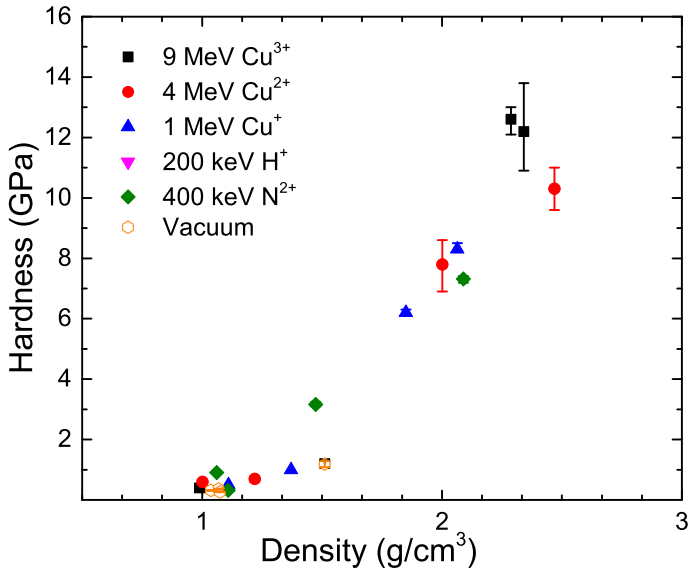

(a) Hardness

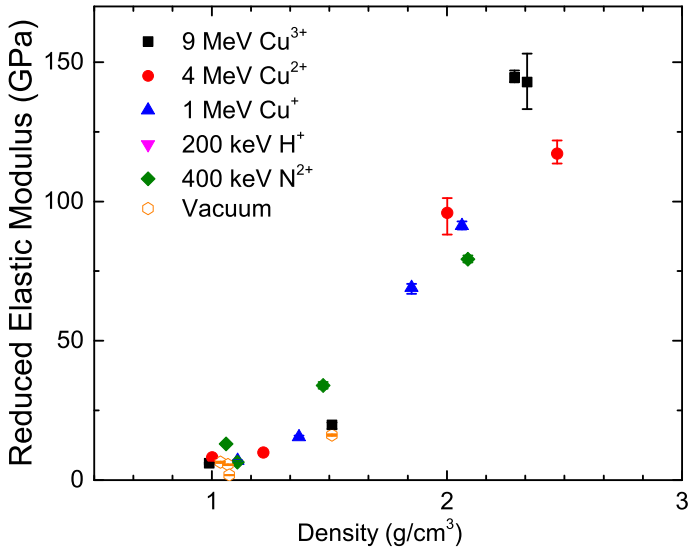

(b) Reduced elastic modulus

Figure 4.28: Plots of (a) hardness and (b) reduced elastic modulus of the acid catalyzed films irradiated with 200 keV H^+, 400 keV N^{2+}, 1 MeV Cu^+, 4 MeV Cu^{2+} and 9 MeV Cu^{3+} as a function of film density. Also shown are the films heat treated in vacuum.

The resulting hardness and reduced elastic modulus of the ion irradiated films as a function of electronic stopping and total stopping are shown in Figs. 4.29 - 4.32 for different irradiation fluences. Hardness and reduced elastic modulus were observed to increase with increasing electronic and total stopping for a given fluence, except for the film irradiated with 9 MeV Cu^{3+} at a fluence of 1×10^{13} ions/cm^2 and the film irradiated with 4 MeV Cu^{2+} at a fluence of 1×10^{14} ions/cm^2.

The electronic stopping powers of 1 MeV Cu^+ and 400 keV N^{2+} are 35.3 and 25.5 eV/Å-ion, respectively, as shown in Table 4.2. The nuclear stopping power of 1 MeV Cu^+ is 30.8 eV/Å-ion, comparable with its electronic stopping, while the nuclear stopping of 400 keV N^{2+} is negligible. The film irradiated with 1 MeV Cu^+ exhibited a higher hardness and reduced elastic modulus than the film irradiated with 400 keV N^{2+} at the same fluence. For example, at a fluence of 1×10^{13} ions/cm^2, the film irradiated with 1 MeV Cu^+ had a hardness of 0.5 GPa and reduced elastic modulus of 7.0 GPa, while the film irradiated with 400 keV N^{2+} had a hardness of 0.3 GPa and reduced elastic modulus of 6.4 GPa. At a fluence of 1×10^{14} ions/cm^2, the film irradiated with 1 MeV Cu^+ had a hardness of 1.0 GPa and reduced elastic modulus of 15.5 GPa, while the film irradiated with 400 keV N^{2+} had a hardness of 0.9 GPa and reduced elastic modulus of 13.0 GPa. The difference in the hardness and reduced elastic modulus became greater at higher fluences. At a fluence of 1×10^{15} ions/cm^2, the film irradiated with 1 MeV Cu^+ had a hardness of 6.2 GPa and reduced elastic modulus of 69.1 GPa, which are approximately twice the values for the film irradiated with 400 keV N^{2+}. This suggests that both electronic stopping and nuclear stopping contribute to the improvements of the mechanical properties.

Figure 4.33 shows the hardness and reduced elastic modulus of the acid catalyzed films irradiated with 200 keV H^+, 400 keV N^{2+}, 1 MeV Cu^+, 4 MeV Cu^{2+} and 9 MeV Cu^{3+} as a function of total energy deposited per thickness (defined as the product of total stopping power and fluence) on a logarithmic plot. For each ion species, with increasing total deposited energy per thickness, the hardness and reduced elastic modulus increased as a result of the conversion of the polymer to a ceramic through the decomposition of the organic components, increased interconnectivity and reduced porosity. However for different ions with the same deposited energy per thickness, the films exhibited different mechanical properties. The hardness and elastic modulus of the films irradiated with 200 keV H^+ showed a linear relationship with energy loss on the logarithmic plot. With increasing total stopping power, this linear relationship no longer held as shown in Fig. 4.33. Figure 4.34 shows the H atomic concentration as a function of total energy deposited per thickness on a semi-logarithmic plot. There is no simple relationship between the H atomic concentration and the total deposited energy per thickness.

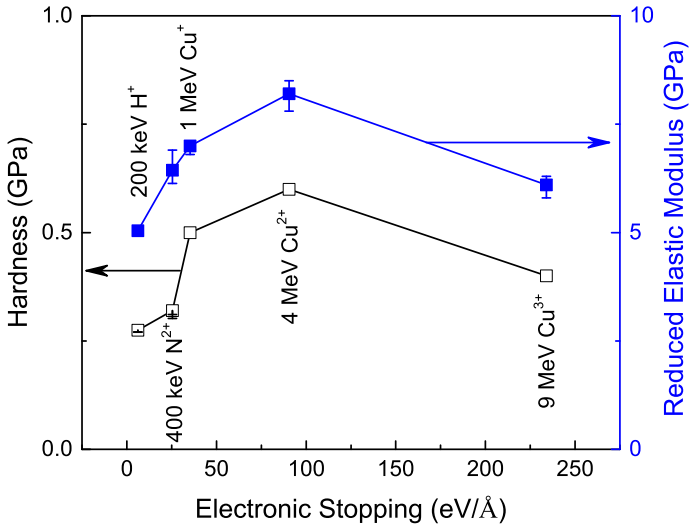

(a) Electronic Stopping

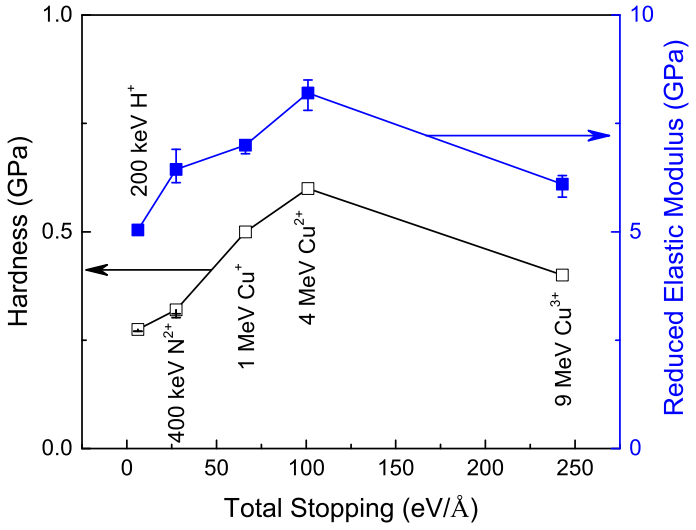

(b) Total Stopping

Figure 4.29: Hardness and reduced elastic modulus of the acid catalyzed films irradiated at a fluence of 1×10^{13} ions/cm^2 as a function of (a) electronic stopping and (b) total stopping.

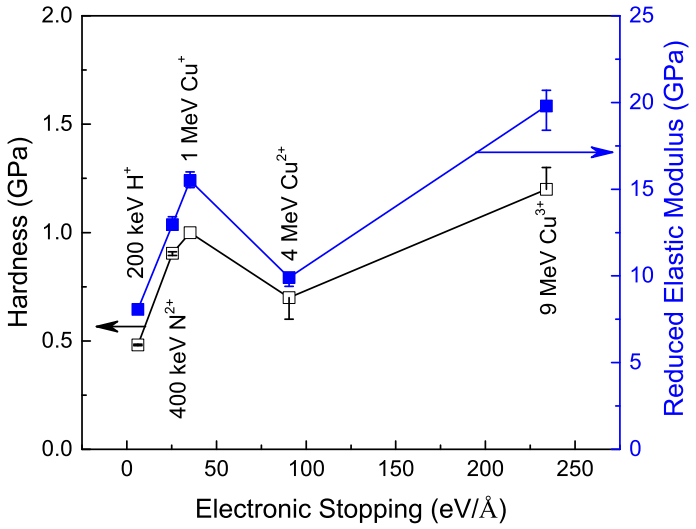

(a) Electronic Stopping

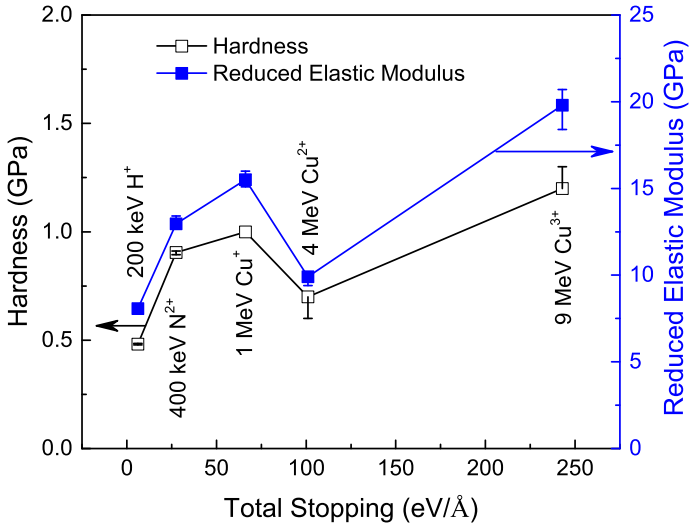

(b) Total Stopping

Figure 4.30: Hardness and reduced elastic modulus of the acid catalyzed films irradiated at a fluence of 1×10^{14} ions/cm^2 as a function of (a) electronic stopping and (b) total stopping.

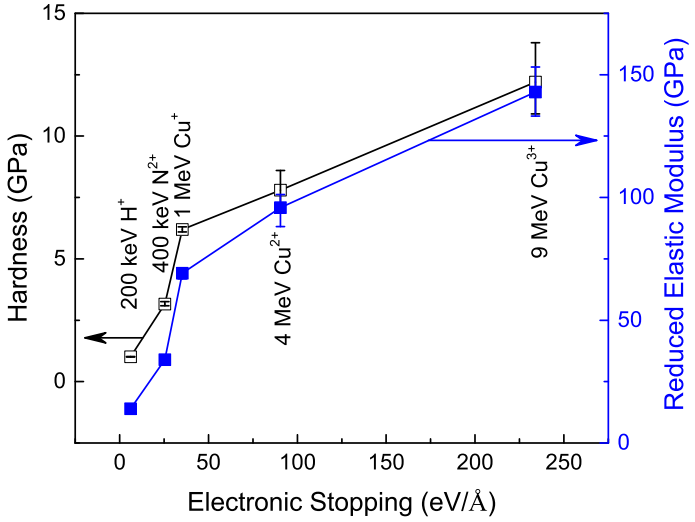

(a) Electronic Stopping

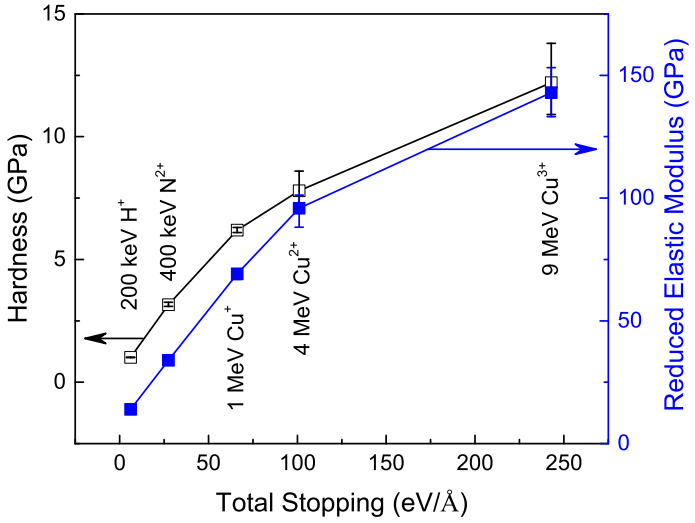

(b) Total Stopping

Figure 4.31: Hardness and reduced elastic modulus of the acid catalyzed films irradiated at a fluence of 1×10^{15} ions/cm^2 as a function of (a) electronic stopping and (b) total stopping.

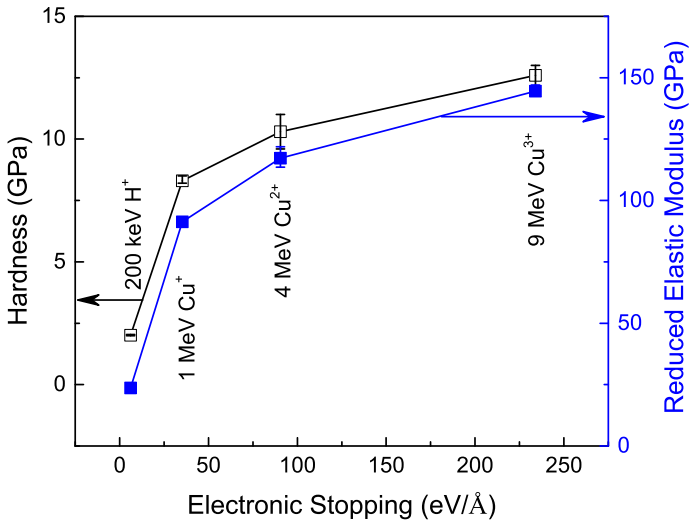

(a) Electronic Stopping

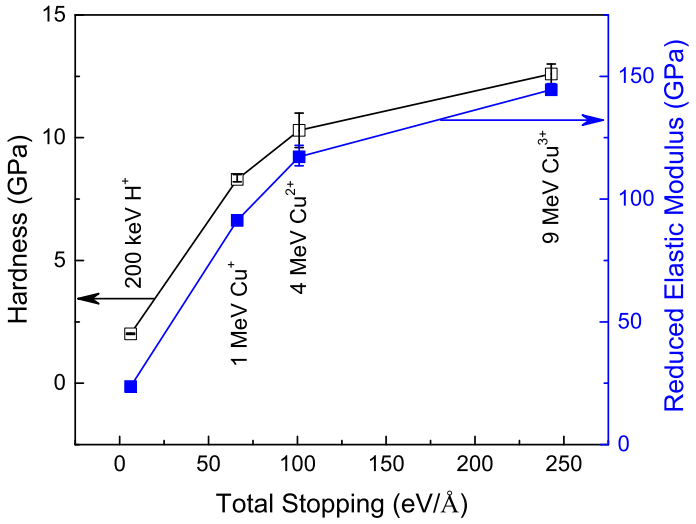

(b) Total Stopping

Figure 4.32: Hardness and reduced elastic modulus of the acid catalyzed films irradiated at a fluence of 1×10^{16} ions/cm^2 as a function of (a) electronic stopping and (b) total stopping.

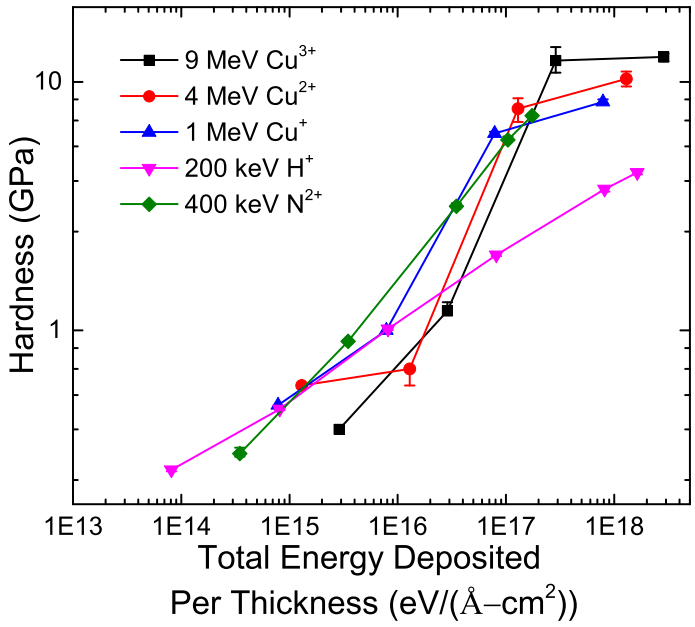

(a) Hardness

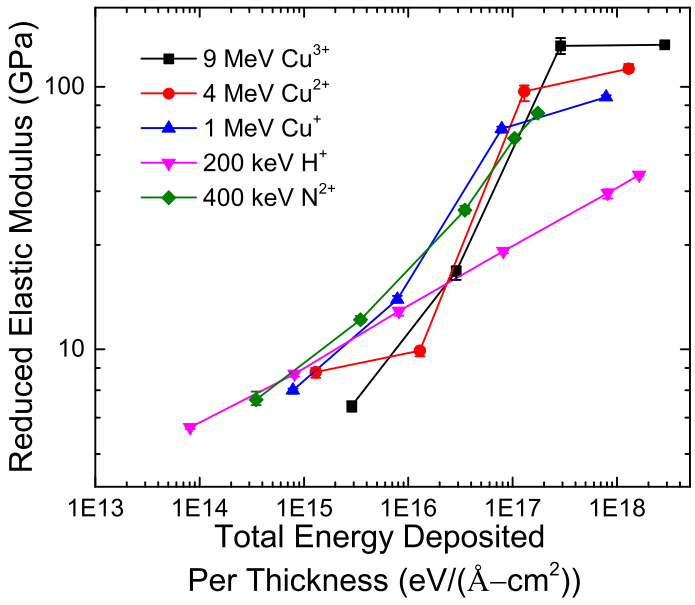

(b) Reduced elastic modulus

Figure 4.33: Plots of (a) hardness and (b) reduced elastic modulus of the acid catalyzed films irradiated with 200 keV H^+, 400 keV N^{2+}, 1 MeV Cu^+, 4 MeV Cu^{2+} and 9 MeV Cu^{3+} as a function of total energy deposited per thickness.

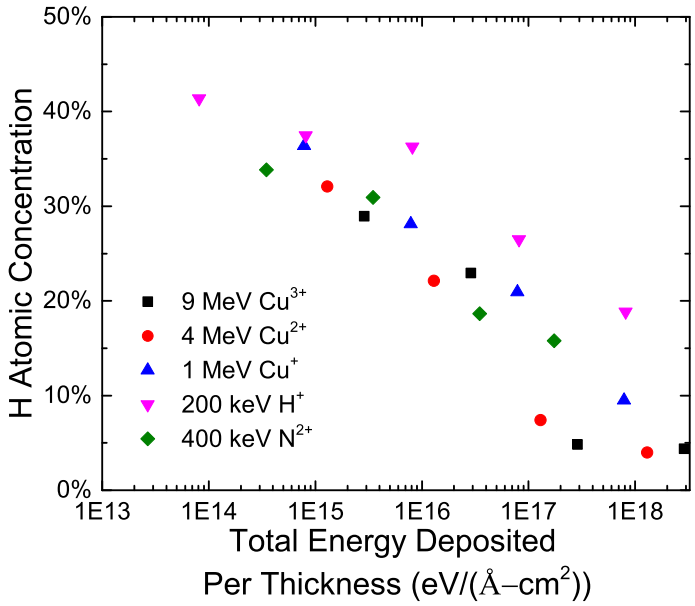

Figure 4.34: Hydrogen concentration of the acid catalyzed films irradiated with 200 keV H^+, 400 keV N^{2+}, 1 MeV Cu^+, 4 MeV Cu^{2+} and 9 MeV Cu^{3+} as a function of total energy deposited per thickness.

4.3.4 Proposed Model to Evaluate the Elastic Modulus of the Fully Converted Films

Based on the understanding of the silicon oxycarbide material produced through pyrolysis, it is proposed that the films fully converted by ion irradiation have a similar structure as the silicon oxycarbide materials heat treated in Ar flow at 1000 - 1200 °C. The fully converted films are simply defined as the films having a H/Si ratio of <1 after ion irradiation in this study. A simple method that has been used in analyzing the elastic properties of various polymer-derived amorphous ceramics is to consider the amorphous material as being formed by the most favorable constituents thermodynamically [67]. The chemical structure of silicon oxycarbide can be written as xSiC + $(1-x)$$SiO_2$ + yC in C-rich oxycarbide or xSiC + $(1-x)$$SiO_2$ + zSi in Si-rich oxycarbide [43, 44], of which the first two terms represent a stoichiometric silicon oxycarbide while the last term stands for the secondary phase: free carbon or silicon . Therefore the amorphous material can be treated as a mixture of amorphous SiC, amorphous silica and excess free C (or free Si).

Based on the simple rule of mixtures (Voigt and Reuss model [157]), the elastic modulus of a C-rich composite (E) is

$$E = v_1 E^{\alpha}_{SiC} + v_2 E^{\alpha}_{a-SiO_2} + v_3 E^{\alpha}_{C} \tag{4.8}$$

where E_{SiC}, E_{a-SiO_2} and E_C denotes the elastic modulus of amorphous SiC, amorphous silica, and free carbon, respectively, v_1, v_2 and v_3 are the corresponding volume fractions, and α is a constant between -1 and +1. When $\alpha = 1$, it leads to an upper bound known as the Voigt average, and when α = -1 it results in a lower bound known as the Reuss average. Therefore a commonly used approach is to take the average of the upper and lower bound, known as the Voigt-Reuss-Hill average. The elastic modulus of SiC ceramic is taken as ∼300 GPa [158–160] and its density as 3.21 g/cm^3. Fused silica has an elastic modulus of 72 GPa and a density of 2.20 g/cm^3. The density of the carbon clusters is considered to be close to the theoretical density of graphite, 2.26 g/cm^3. The excess free carbon existing in the films is assumed to be graphitic carbon which has negligible contribution to the system modulus. A typical procedure to calculate the reduced elastic modulus based on this model is reported here. The film irradiated with 9 MeV Cu^{3+} at a fluence of 1×10^{15} ions/cm^2 has a chemical composition $SiC_{0.88}O_{0.72}$, corresponding to the thermodynamic composition of 0.64SiC + 0.36SiO_2 + 0.24C. The volume fraction of each constituent ($v_1 = 0.42$, $v_2 = 0.51$ and $v_3 = 0.07$) was determined from the chemical composition and the density of each constituent. Finally, the upper and lower bound moduli are calculated (E_{Voigt} = 163.1 GPa, E_{Reuss} = 117.4 GPa), thus the average is 140.2 GPa. In order to compare with our experimental results, the calculated elastic modulus is converted to the reduced elastic modulus through Eq. 3.3 with Poisson's ratio being assumed to be 0.17 (which is that of fused silica).

Only the irradiated films with much of the H released can be analyzed with this model, as it is based upon the assumption that the only elements in the material system are Si, C and O. Table 4.4 shows the calculated reduced elastic modulus using the Voigt and Reuss model, the measured reduced elastic modulus evaluated at a contact depth/thickness of 10%, and the reduced elastic modulus from the Doerner & Nix's model, for some selected ion irradiated films. The chemical composition was obtained through the analysis of the RBS data. The calculated reduced elastic modulus was within a 15% error of the measured reduced elastic modulus, which indicates the validation of applying this model to estimate the reduced elastic modulus from the chemical composition.

The mechanical properties of the silicon oxycarbide obtained with heat treatment through different starting materials were increased with x, a measure of Si-C bond concentration in the silicon oxycarbide network [43, 44]. The excess free carbon had negligible contribution to the system modulus. Silicon oxycarbide synthesized with RF sputtering had a reduced elastic modulus from 68.1 to 242.9 GPa depending on the deposition rate of silicon carbide to that of silicon dioxide [161]. This is in agreement with literature that carbide is a much stiffer material than the relative soft oxide. The reduced elastic modulus of the fully converted films after ion irradiation also increased with

Table 4.4: Calculated and measured reduced elastic modulus of selected ion irradiated films.

Ion Irradiation Conditions	Chemical Composition	SiC x	SiO_2 1-x	C y	Calculated (GPa)	Measured (GPa)	Doerner & Nix's Model (GPa)
9 MeV Cu^{3+} 1E15	$SiC_{0.88}O_{0.72}$	0.64	0.36	0.24	128.3	142.9	132.0
9 MeV Cu^{3+} 1E16	$SiC_{0.78}O_{0.80}$	0.60	0.40	0.18	122.6	144.5	133.2
4 MeV Cu^{2+} 1E16	$SiC_{1.14}O_{1.17}$	0.41	0.59	0.72	100.0	117.2	115.6
1 MeV Cu^{+} 1E16	$SiC_{2.76}O_{1.29}$	0.35	0.65	2.41	98.2	91.3	85.3

increasing Si-C bond concentration, consistent with that of the silicon oxycarbide produced by heat treatment in Ar flow or RF sputtering. Unlike the pyrolyzed silicon oxycarbide in which the concentration of Si-C bond can only be tailored by varying the precursors in the sol-gel process [44,67], the Si-C bond concentration in silicon oxycarbide obtained from ion irradiation could be easily adjusted by varying the stopping power and ion species.

4.3.5 A Plausible Structural Evolution During Ion Irradiation

The incorporation of a high carbon content into fused silica is difficult. Most silicon oxycarbide glass reported in the literature were synthesized by the sol-gel process. The chemical composition of pyrolyzed silicon oxycarbide can be tailored by varying the precursors in the sol-gel process. The stoichiometric silicon oxycarbide, consisting solely of Si-O and Si-C bonds, is formed by a random array of SiC_zO_{4-z} tetrahedra ($0 \leq z \leq 4$) [44,162,163]. Carbon is bonded to four silicon atoms forming tetracoordinated CSi_4 units. Compared to fused silica, the presence of tetrahedrally coordinated CSi_4 units leads to a stiffer and constrained network with improved mechanical properties such as elastic modulus, hardness as well as density, viscosity and glass transition temperature [44–46, 52]. The improvements of many silicon oxycarbide properties depend on the amount of carbon directly bonded to silicon in the silicon oxycarbide network [164]. The excess free carbon acting as a secondary phase can be detrimental for the high-temperature stability of silicon oxycarbide in oxidizing [164].

Possible Schemes of Forming Tetrahedrally Coordinated CSi_4 Units

For pyrolyzed silicon oxycarbide, tetracoordinated CSi_4 units were formed gradually through successive bond cleavages, combinations and rearrangements [45]. The chemical structure of the ion

irradiated films is more complex and the mechanism of forming CSi_4 units is different. Figure 4.35 shows possible schemes of forming CSi_4 units through the destruction of Si-O-C_2H_5 and Si-CH_3. Cleavage of C-H bonds in Si-CH_3 could lead to the formation of C-C, thus forming free carbon and releasing H_2. The CSi_4 units could be formed between Si-C- dangling bonds and Si-O-Si- dangling bonds, of which the former could be produced by cleavage of C-H bonds in Si-CH_3, and the latter could be formed by cleavage of Si-C bonds in Si-CH_3 or Si-O bonds in Si-O-C_2H_5. Scheme (a) represents a construction of CSi_4 units by cleavage of three C-H bonds in Si-CH_3 and three Si-O bonds in Si-O-C_2H_5, and scheme (b) shows cleavage of three C-H bonds and three Si-C bonds in Si-CH_3. Scheme (a) introduces a decrease in O concentration while scheme (b) does not. The ratio of -O-C_2H_5 to Si is 1.4 while the ratio of -CH_3 to Si is 0.6 according to the theoretical formula. Simply from the view of the localized density, scheme (a) is more likely if the energy difference in cleaving C-H bonds in Si-CH_3 and Si-O bonds in Si-O-C_2H_5 was not considered.

The atomic ratio O/Si of the fully converted films, which can be found in Table 4.3, is 0.8, 1.2, 1.3, 2.5 and 2.8 for the films irradiated at the highest fluence used with 9 MeV Cu^{3+}, 4 MeV Cu^{2+}, 1 MeV Cu^{+}, 400 keV N^{2+}, and 200 keV H^{+}, respectively. Oxygen release might be related with both Si-O-Si network and Si-O-C_2H_5, in which the latter is assumed to be more favorable. The amount of O released is consistent with the total stopping power of the ions used in the irradiation. This suggests that cleavage of Si-O in Si-O-C_2H_5 is highly dependent on the total stopping power of the incident ions. Irradiation with 400 keV N^{2+} or 200 keV H^{+} has negligible effects on decomposing the Si-O-C_2H_5 thus the O/Si in the final product is still comparable to the green films, while irradiation with 9 MeV Cu^{3+} results in a complete destruction of the Si-O-C_2H_5 structure leading to the O/Si ratio being close to one. Therefore, it is possible to tailor the O/Si in the resulting silicon oxycarbide, and thus the concentration of carbon directly bonded to silicon. This in turn can tailor the mechanical properties of the film.

4.3.6 Microstructure of the Ion Irradiated Films

The microstructure of the films irradiated with 200 keV H^{+} and 400 keV N^{2+} at various fluences was also studied by depth resolved XRD. Figures 4.36 and 4.37 shows depth resolved XRD patterns collected at glancing angles of 2°, 4°, 6°, 8° and 10° from the acid catalyzed films irradiated with 200 keV H^{+} and 400 keV N^{2+} at a fluence of 1×10^{13} to 5×10^{15} ions/cm^2. Each increase (2° rotation) in the glancing angle was considered to be corresponding to a change of about 60 nm in depth on average. Some crystalline peaks were observed around 44° and 50 - 60°. The peaks

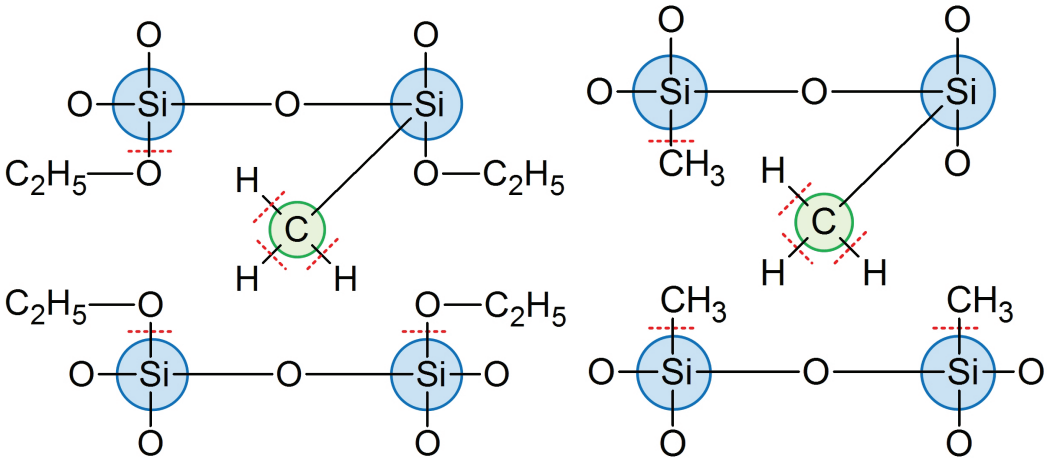

(a) Scheme (a) (b) Scheme (b)

Figure 4.35: Possible schemes for formation of CSi_4 units through destruction of (a) Si-O in Si-O-C_2H_5 and C-H in Si-CH_3, and (b) Si-C in Si-CH_3 and C-H in Si-CH_3.

located between 50 - 60° were similar to those from the acid catalyzed films heat treated at 700 or 800 °C and were the most intense when collected at a depth of about 240 nm. When the data was collected at a deeper or shallower depth, the intensity of these peaks decreased. For each ion species, the intensity of these peaks increased with increasing fluence. The peaks around 44° were observed on films irradiated with 400 keV N^{2+} at all fluences but only on films irradiated with 200 keV H^+ at a fluence of 1×10^{15} ions/cm^2. These peaks increased in intensity with increasing collecting depth. With limited number of peaks, the possible crystalline phase can not be determined. It suggests the majority of the films after ion irradiation are still amorphous.

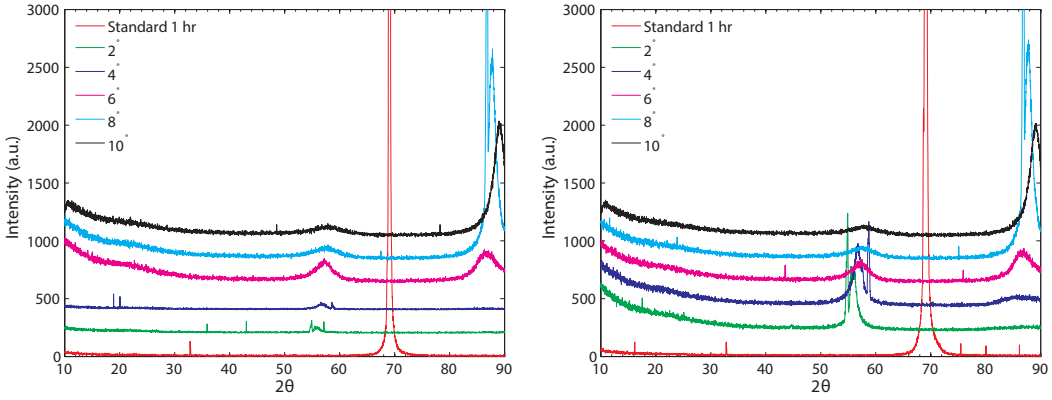

(a) 200 keV H^+, 1×10^{13} ions/cm^2

(b) 200 keV H^+, 1×10^{14} ions/cm^2

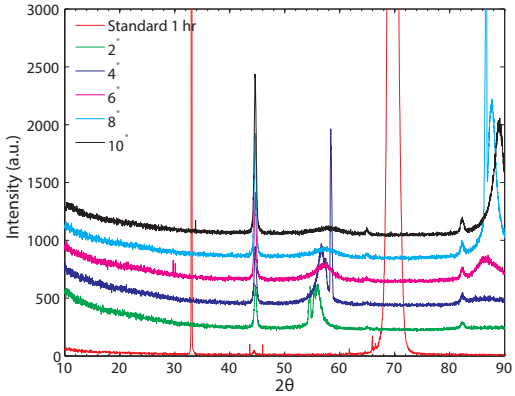

(c) 200 keV H^+, 1×10^{15} ions/cm^2

Figure 4.36: Depth resolved XRD patterns collected at glancing angles of 2°, 4°, 6°, 8° and 10° from the acid catalyzed films irradiated with 200 keV H^+ at a fluence of (a) 1×10^{13} ions/cm^2, (b) 1×10^{14} ions/cm^2, and (c) 1×10^{15} ions/cm^2.

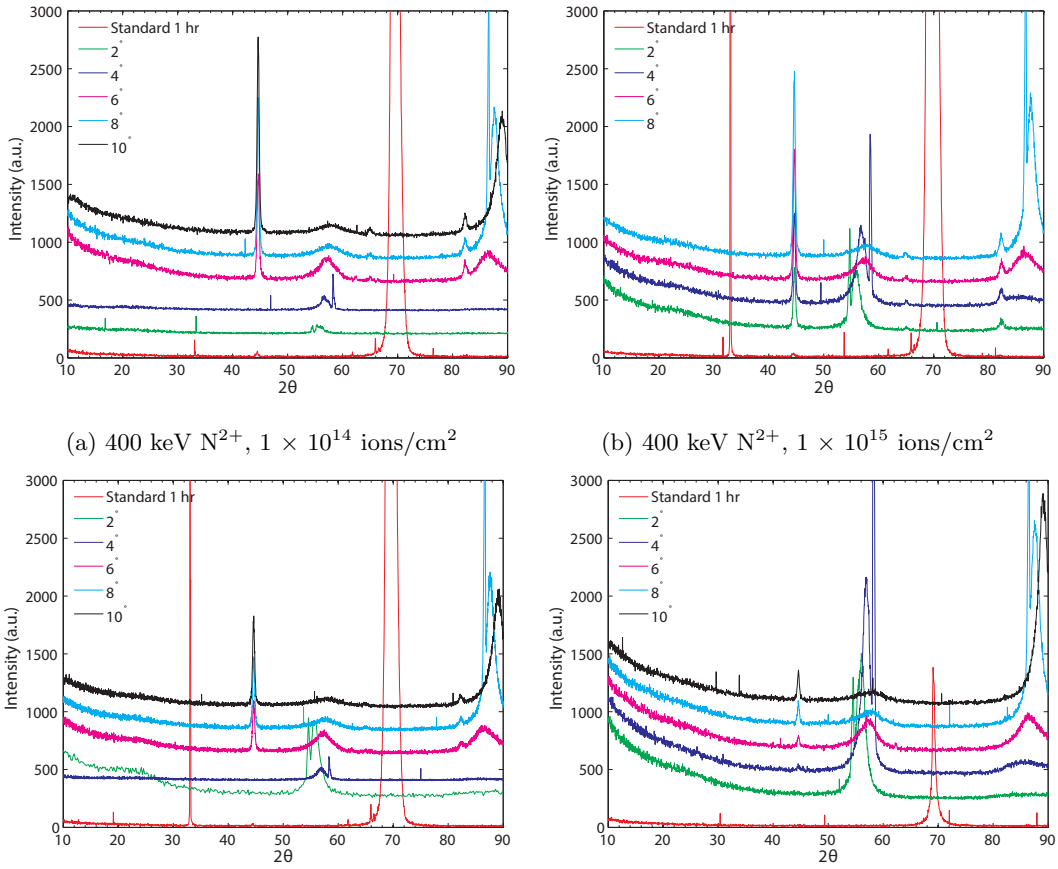

(a) 400 keV N^{2+}, 1×10^{14} ions/cm^2

(b) 400 keV N^{2+}, 1×10^{15} ions/cm^2

(c) 400 keV N^{2+}, 1×10^{15} ions/cm^2

(d) 400 keV N^{2+} 5×10^{15} ions/cm^2

Figure 4.37: Depth resolved XRD patterns collected at glancing angles of 2°, 4°, 6°, 8° and 10° from the acid catalyzed films irradiated with 400 keV N^{2+} at a fluence of (a) 1×10^{14} ions/cm^2, (b) 1×10^{15} ions/cm^2 with beam current of 50 nA, (c) 1×10^{15} ions/cm^2 with beam current of 200 nA, and (d) 1×10^{15} ions/cm^2.

4.4 Investigation of the Base Catalyzed Films

Initially heat treatment and ion irradiation were performed on the base catalyzed films. However, after preliminary investigation and comparing with previous study on the acid catalyzed films, the acid catalyzed films were found to be more favorable in studying the effects of heat treatment and ion irradiation and have been our main focus. This section presents experimental results and findings of the base catalyzed films as a result of heat treatment and ion irradiation.

4.4.1 Effects of Heat Treatment

The green films of the base catalyzed sol-gel system were synthesized by heat treatment in ambient air for 30 min and had a nominal thickness of 1 μm. Heat treatment was performed in ambient air at temperatures from 300 to 800 °C at the IWT in Germany. The resulting changes in the film thickness and shrinkage after heat treatment are shown in Fig. 4.38. Also shown are the film thickness and shrinkage of the acid catalyzed films having the same nominal thickness of 1 μm. Both the acid and base catalyzed films exhibited the same trend that film thickness decreased and shrinkage increased with increasing heat treatment temperature. The acid and base catalyzed films had an initial difference in thickness of about 200 nm before heat treatment, and about the same difference after heat treatment at the same temperature.

The effect of heat treatment on the hardness and reduced elastic modulus was investigated using nanoindentation. Figure 4.39 shows the hardness and reduced elastic modulus of both the acid and base catalyzed films after heat treatment in ambient air. Heat treatment was found to increase the hardness and reduced elastic modulus for both types of films. The base catalyzed films showed a higher hardness and reduced elastic modulus than the acid catalyzed films heat treated at the same temperature. Additionally the base catalyzed films exhibited a higher increase in hardness and reduced elastic modulus with increasing temperature below 600 °C, but a relatively constant hardness and reduced elastic modulus when heat treated at temperatures above 600 °C. Unlike the base catalyzed films, the acid catalyzed films showed a monotonic increase in hardness. The base catalyzed films exhibited a maximum hardness of 3.2 GPa when heat treated at 600 °C while the acid catalyzed films had a maximum of 1.3 GPa at 800 °C. Regarding the reduced elastic modulus, the base catalyzed films heat treated at 600 °C exhibited a maximum of 71.6 GPa (a little higher than that of fused silica, 69.6 GPa) while the acid catalyzed films had a maximum of 19.5 GPa when heat treated at 800 °C. Figure 4.40 shows the measured hardness as a function of film shrinkage for both the acid and base catalyzed films after heat treatment. When compared at the same shrinkage,

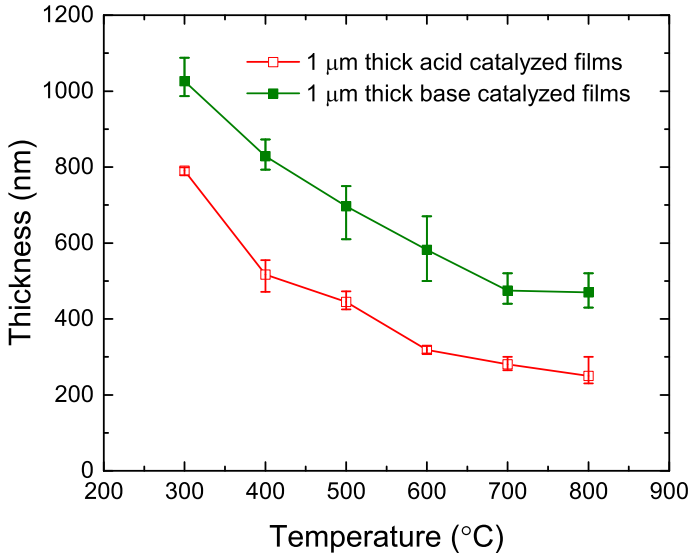

(a) Film thickness

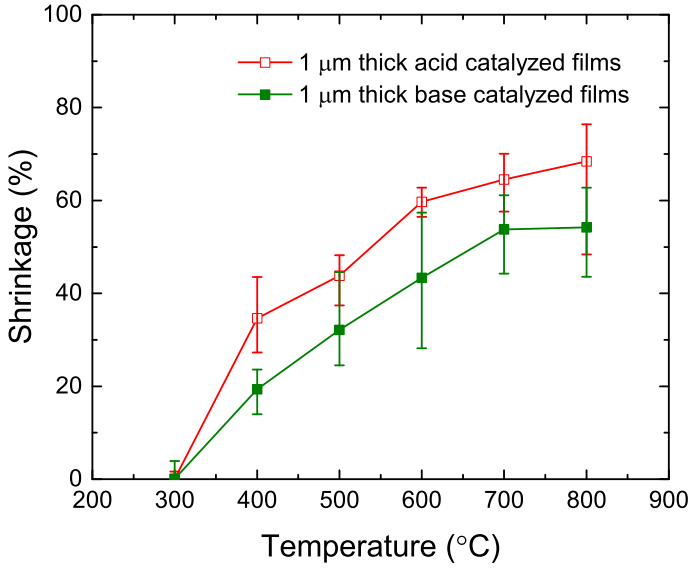

(b) Film shrinkage

Figure 4.38: Plots of (a) film thickness and (b) shrinkage measured as a function of heat treatment temperature for both the acid and base catalyzed films.

the based catalyzed films exhibited a higher hardness than the acid catalyzed films. It suggests that change in hardness is not simply related to film shrinkage but also relies on the type of the sol-gel films.

4.4.2 Effects of Ion Irradiation

Ion irradiation of the base catalyzed films was carried out at room temperature using H^+ and N^{2+} ions at Los Alamos National Laboratory. Table 4.5 lists the ion irradiation conditions for 1 μm thick base catalyzed films, including the ion species, the energy of the incident ions, electronic and nuclear stopping power, projected range and fluence. The chemical composition of the green films determined from XPS and ERD are also shown. The projected range is larger than the film thickness such that full irradiation is achieved. Also shown in Table 4.5 are the ion irradiation conditions for 600 nm thick acid catalyzed films pursued in a previous study [17]. The base catalyzed green films have a much lower H/Si (0.8) and C/Si (0.4) compared with the acid catalyzed green films in the previous study having a H/Si of 2.5 and C/Si of 2.3. Despite of the difference in film thickness and density, the electronic and nuclear stopping power of 125 keV H^+, as well as that of 250 keV N^{2+}, in the base catalyzed films are similar to that in the acid catalyzed films.

Table 4.5: Ion irradiation conditions for 1 μm thick base catalyzed films and 600 nm thick acid catalyzed films: chemical composition, thickness, density, average electronic and nuclear stopping power, projected range and fluence.

	Acid catalyzed films [17]		Base catalyzed films	
Chemical Composition	$SiO_{1.5}C_{2.3}H_{2.5}$		$SiO_{1.8}C_{0.4}H_{0.8}Na_{0.3}$	
Thickness (nm)	600		1000	
Density (g/cm^3)	1.1		1.3	
Ions	125 keV H^+	250 keV N^{2+}	125 keV H^+	250 keV N^{2+}
Electronic Stopping (eV/Å-ion)	6.4	24.9	7.4	26.4
Nuclear Stopping (eV/Å-ion)	0.0	1.9	0.0	2.2
Projected range (μm)	2.1	1.1	1.8	1.0
Fluence (10^{15} ions/cm^2)	0.1 - 100	0.1 - 50	0.1 - 15	0.1 - 10

The film shrinkage of the base catalyzed films irradiated with 125 keV H^+ and 250 keV N^{2+} as

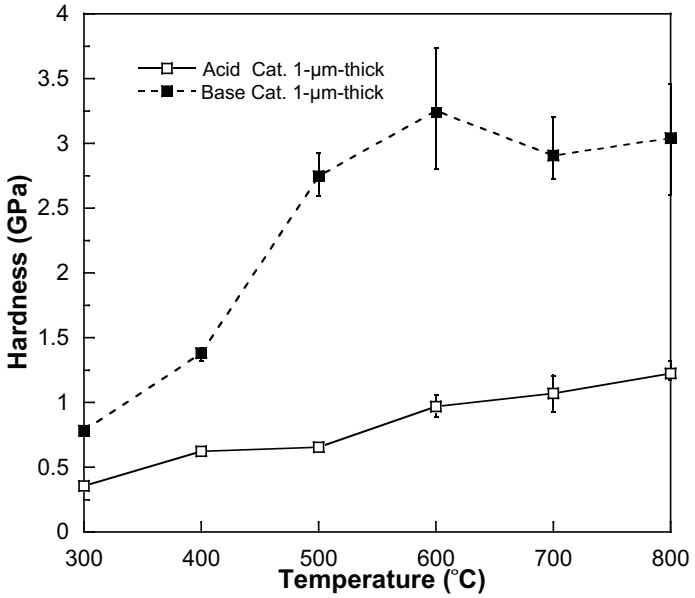

(a) Hardness

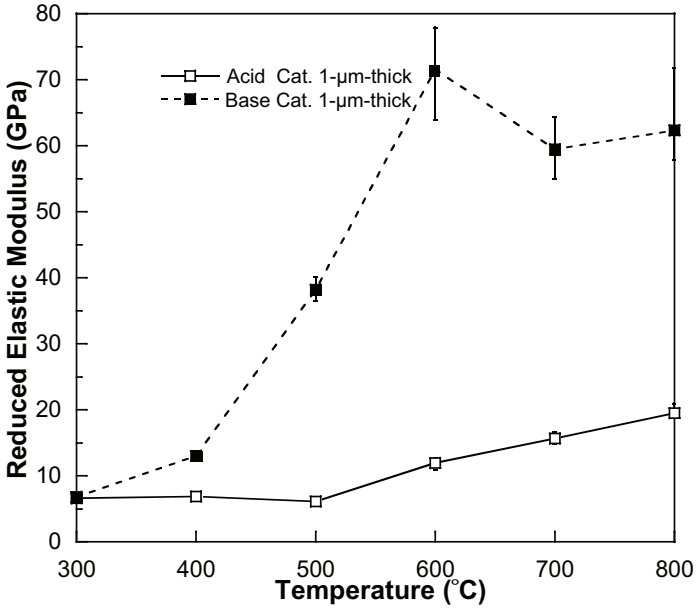

(b) Reduced elastic modulus

Figure 4.39: Plots of (a) hardness and (b) reduced elastic modulus of the acid and base catalyzed films heat treated at different temperatures as a function of heat treatment temperature.

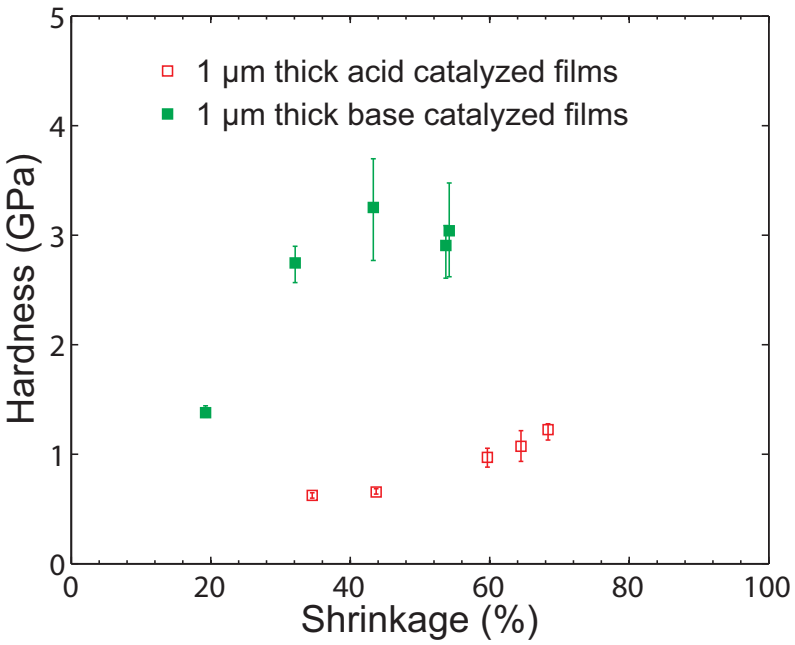

Figure 4.40: Hardness of the acid and base catalyzed films after heat treatment as a function of film shrinkage.

a function of fluence is shown in Fig. 4.41. Also shown is the film shrinkage of the acid catalyzed films irradiated with the same ion species and the same energy. Shrinkage was observed to increase with increasing fluence regardless of the type of the sol-gel system, ion species and energy of the ions. In contrast with the observation that the 250 keV N^{2+} resulted in a much higher shrinkage than the 125 keV H^{+} for the acid catalyzed films when compared at the same fluence, both ions play a similar role for the base catalyzed films.

The hardness and reduced elastic modulus depth profiles of 1 μm thick base catalyzed films irradiated with 125 keV H^{+} and 250 keV N^{2+} are shown in Fig. 4.42. Unlike the acid catalyzed films, the base catalyzed films showed a considerable decrease in hardness and reduced elastic modulus as the normalized contact depth increased from 5% to 20% after N^{2+} irradiation at a fluence of 10^{15} or 10^{16} ions/cm^2. The reason for the decrease in the measured hardness and reduced elastic modulus is unclear. A potential cause might be microstructure of the films irradiated by 250 keV N^{2+} is nonuniform and varies with depth.

The effect of fluence on the hardness and reduced elastic modulus of both the acid and base catalyzed irradiated films, evaluated at 10% of the film thickness, are shown in Fig. 4.43. The observation of increased hardness with increasing ion fluence was consistent for both the acid and base catalyzed films. Irradiation with N^{2+} was observed to be more effective than with H^{+} in

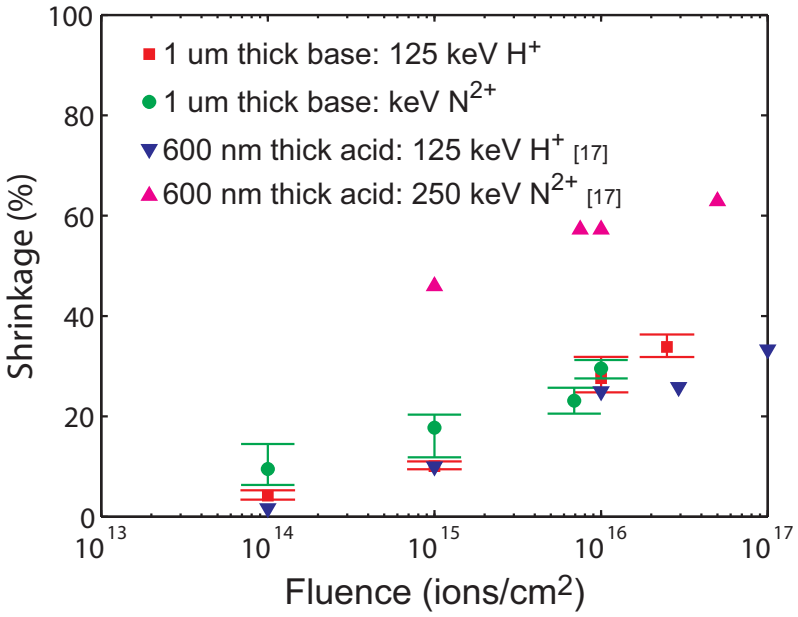

Figure 4.41: Film shrinkage of 1 μm thick base catalyzed films and 600 nm thick acid catalyzed films irradiated with 125 keV H^+ and 250 keV N^{2+} as a function of fluence ranging from 1×10^{13} to 1×10^{17} ions/cm^2.

converting the sol-gel films to their ceramic state for both the acid and base catalyzed films as when the same fluence was used, the films irradiated with N^{2+} showed a higher increase in hardness than with H^+. For the acid catalyzed films, the irradiating ion species plays a greater role in the final achieved hardness than for the base catalyzed system. This can be seen when comparing the results for the N^{2+} and H^+ irradiations. At the highest fluence investigated for both ions, the N^{2+} irradiated acid catalyzed film had a hardness 270% greater than for the film irradiated with H^+. Whereas for the base catalyzed films, only a 30% higher hardness was observed. In addition, at the highest fluence, N^{2+} irradiation of the acid catalyzed films resulted in a higher hardness than for the base catalyzed films, 7.4 GPa compared to 4.7 GPa. This is in contrast with H^+ irradiation which resulted in a slightly higher hardness for the base catalyzed films when compared to the acid catalyzed films. For the base catalyzed films, the reduced elastic modulus showed no dependence on ion species.

The relationship between the mechanical properties and film shrinkage for the acid catalyzed films has been discussed in Chapter 4.3.1. It was shown that the change in the mechanical properties is not simply related to the film shrinkage, but more connected with the microstructural evolution including chemical changes and porosity reduction. Figure 4.44 shows the relationship between hardness and

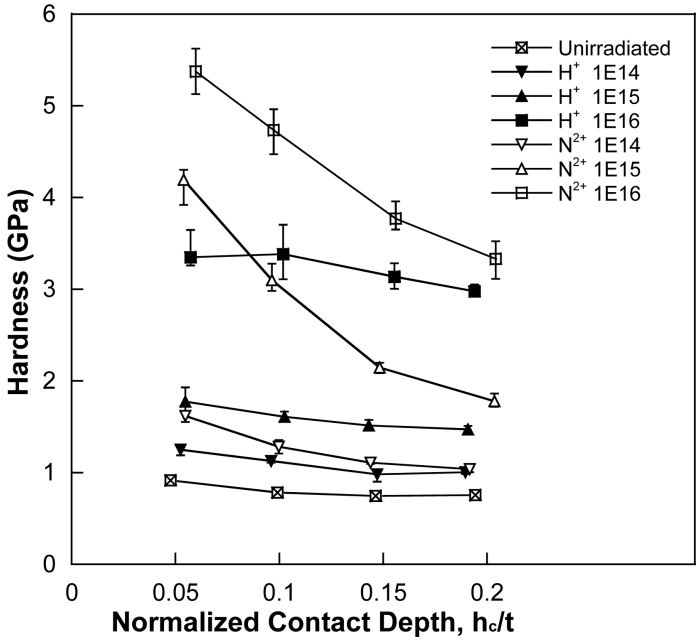

(a) Hardness

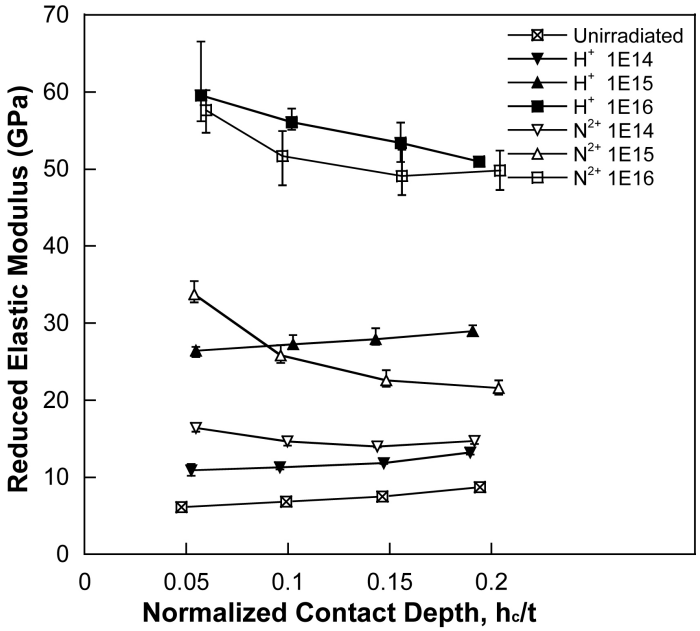

(b) Reduced elastic modulus

Figure 4.42: Depth profiles of (a) hardness and (b) reduced elastic modulus depth profiles of 1 μm thick base catalyzed films irradiated with 125 keV H^+ and 250 keV N^{2+} at fluences ranging from 1×10^{14} to 1×10^{16} ions/cm^2 [11]. For comparison an unirradiated film is also shown.

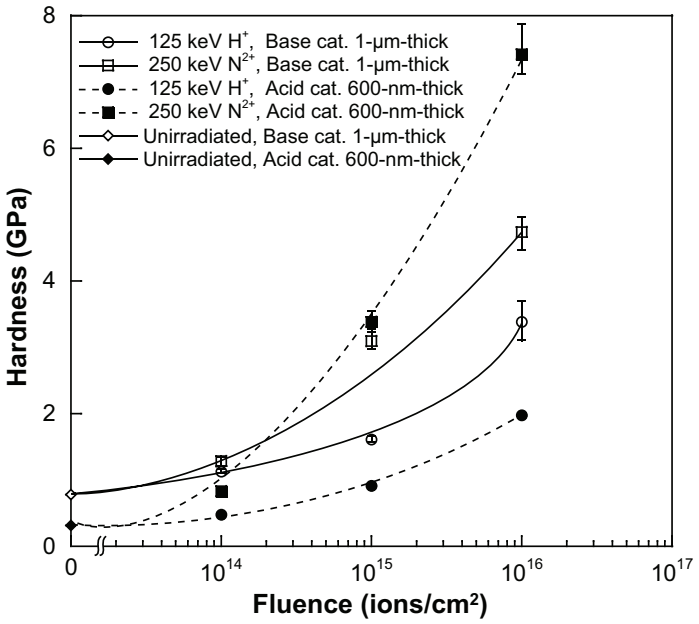

(a) Hardness

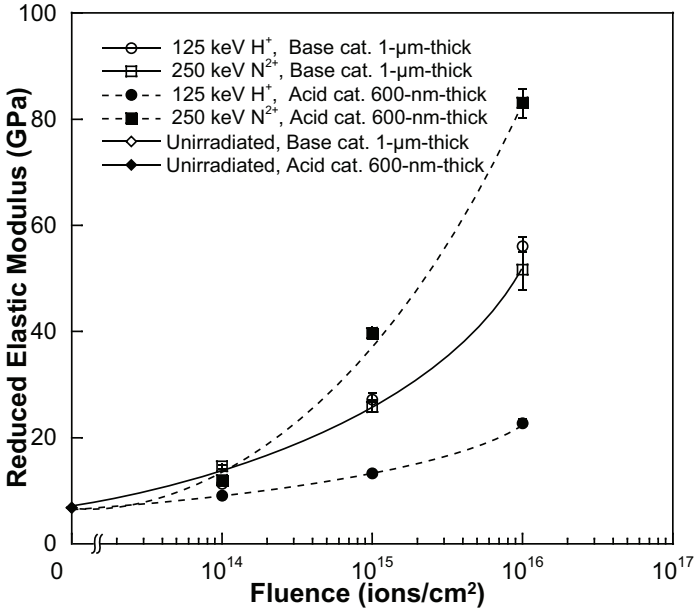

(b) Reduced elastic modulus

Figure 4.43: Plots of (a) hardness and (b) reduced elastic modulus evaluated at 10% of the film thickness of the acid and base catalyzed films irradiated with 125 keV H^+ and 250 keV N^{2+} as a function of fluence [11].

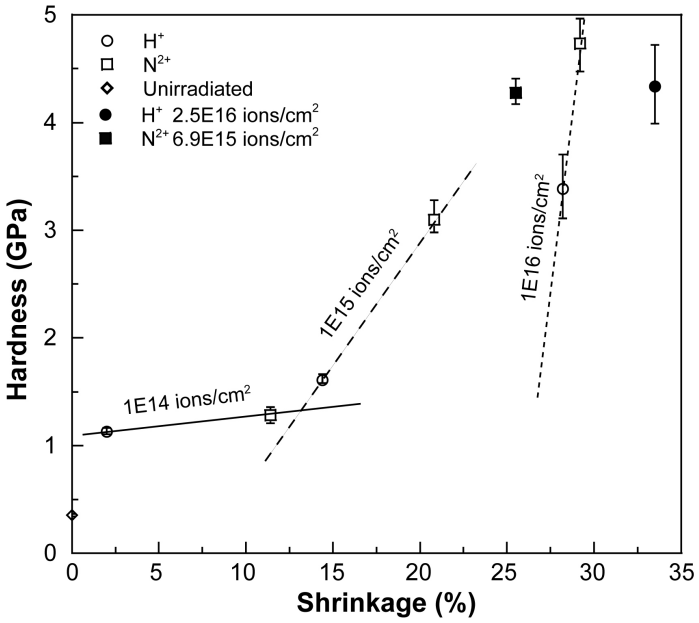

Figure 4.44: Hardness of the base catalyzed films evaluated at 10% of the film thickness as a function of film shrinkage for irradiations with 125 keV H^+ and 250 keV N^{2+} [11].

film shrinkage of the base catalyzed films after irradiation. For both ion species, hardness and film shrinkage were seen to increase with increasing fluence. At a given fluence, N^{2+} irradiation resulted in a higher film shrinkage and higher hardness when compared to H^+ irradiation. The increase in hardness for a given percent shrinkage increased with fluence. The film irradiated with 250 keV N^{2+} at a fluence of 6.9×10^{15} ions/cm^2 exhibited a lower shrinkage (25% compared to 33%) but similar hardness compared with the film irradiated with 125 keV H^+ at a fluence of 2.5×10^{16}. This points to the fact that the hardness increase is not simply related to film shrinkage.

Fig. 4.45 shows the relationship between the measured hardness and film shrinkage after irradiations with H^+ and N^{2+} for both the 1 μm thick base catalyzed and 600 nm thick acid catalyzed films. The base catalyzed films showed a higher hardness for a given percentage shrinkage. At the highest fluence the shrinkage of the base catalyzed film was approximately half that of the acid catalyzed film, 29% as compared to 58%. In general, the response to irradiation of both the acid and base catalyzed films was found to be similar. The effects of ion irradiation on film conversion however were more pronounced for the acid catalyzed system and for the same irradiation conditions, in most cases resulted in films of higher hardness.

The effect of ion irradiation on hardness and hydrogen concentration as a function of fluence is shown in Fig. 4.46. Compared to the acid catalyzed films, the unirradiated base catalyzed films

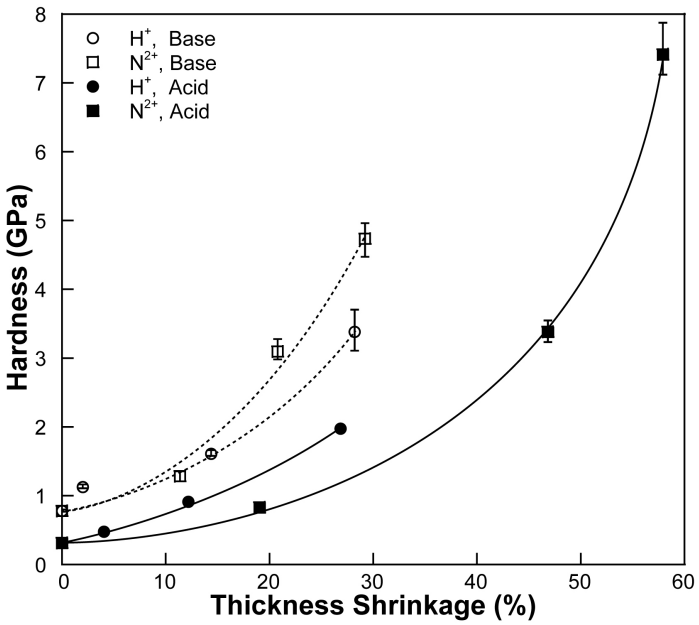

Figure 4.45: Hardness of the acid and base catalyzed films evaluated at 10% of the film thickness as a function of film shrinkage for irradiations with 125 keV H^+ and 250 keV N^{2+} [11].

had a higher hardness, 0.78 GPa compared to 0.32 GPa. Hardness increased with fluence, while hydrogen concentration decreased, for both the acid and base catalyzed films. As produced, the acid catalyzed films had a higher concentration of hydrogen than that for the base catalyzed films. The films exhibited a different hardening response to irradiation with H^+ or N^{2+} based on sol composition.

Fig. 4.47 shows the hardness as a function of resulting hydrogen concentration for irradiations with H^+ and N^{2+} for both sol-gel systems over the range of fluences investigated. For each type of sol-gel film, there is a clear and distinct trend of increasing hardness with decreasing hydrogen concentration, resulting in the two curves shown in Fig. 4.47. No apparent effect of irradiating species was observed. The observed shift in the trend for hardness with hydrogen concentration was consistent with the difference in initial hydrogen concentration of the two sol systems. A minimum hydrogen concentration of about 10% was achieved with ion irradiations at the highest fluences for both the acid and base catalyzed films. However, for this concentration the acid catalyzed films achieved a significantly higher hardness. At the highest fluence, ion irradiation induced a maximum hydrogen loss of 25% for the acid catalyzed films compared to 12% for base catalyzed films as shown in Fig. 4.48.

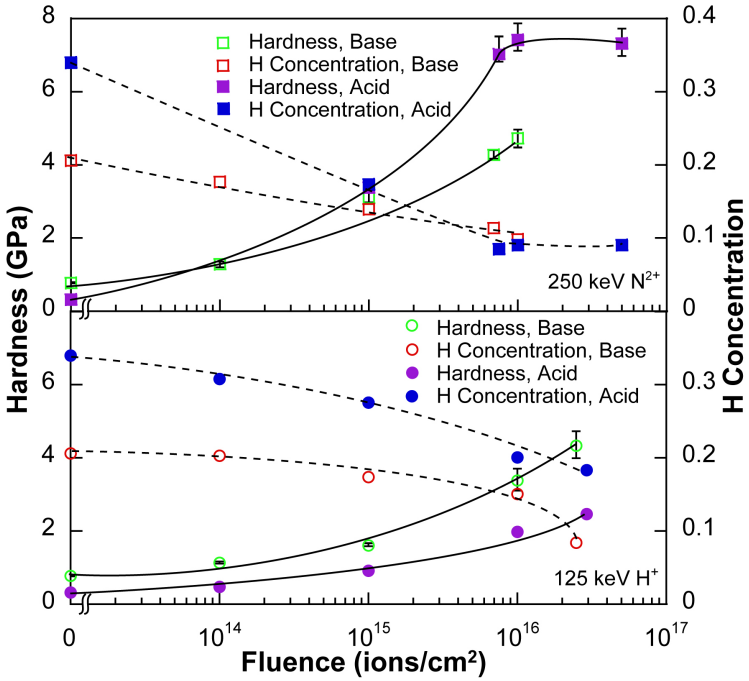

Figure 4.46: Hardness and hydrogen concentration of the acid and base catalyzed films irradiated with 125 keV H^+ and 250 keV N^{2+} as a function of fluence [12].

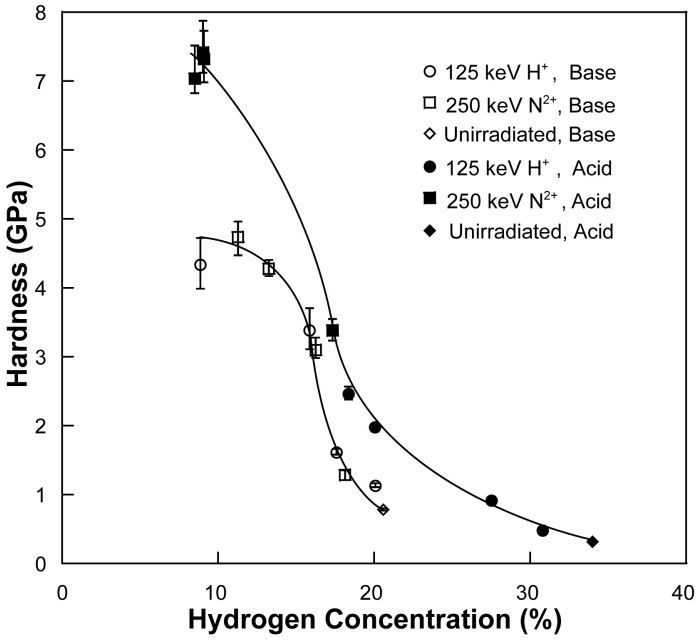

Figure 4.47: Hardness of the acid and base catalyzed films irradiated with 125 keV H^+ and 250 keV N^{2+}as a function of hydrogen concentration [12].

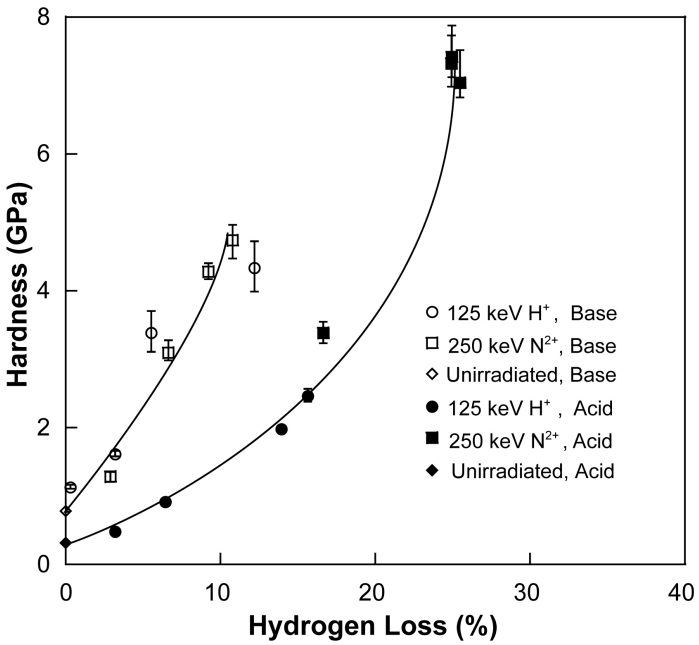

Figure 4.48: Hardness of the acid and base catalyzed films irradiated with 125 keV H^+ and 250 keV N^{2+}as a function of percent hydrogen loss [12].

4.4.3 Effects of Secondary Heat Treatment

Secondary heat treatment was performed on the base catalyzed films after ion irradiation in an Ar flow at 1100 and 1350 °C for 2 hrs. Optical microscopy investigations showed that all films after post-irradiation heat treatment contain bubbles and cracks. A possible reason for the formation of bubbles is the chemical reactions between the substrate and the silica in the films [44]. Regarding the cracks, the mismatch of the thermal expansion coefficient between the film and the substrate is the main contribution [136]. It is noted that the unirradiated base catalyzed films heat treated at 1100 °C and 1350 °C also showed surface cracks while the unirradiated acid catalyzed films heat treated at 1100 °C were still crack-free. Raman spectroscopy experiments performed at OSU [146] have shown that free carbon was retained when heat treated at 1100 °C and disappeared when heat treated at 1350 °C.

Chapter 5

CONCLUSIONS AND FUTURE WORK

5.1 Conclusions

A study of the effects of ion irradiation on the mechanical properties and structural evolution of sol-gel derived silica thin films has been performed. All films were synthesized by sol-gel process using TEOS and MTES as precursors and spin-coated onto (100) Si wafers. The resulting change in the mechanical properties and structural evolution from heat treatment and ion irradiation were investigated by atomic force microscopy (AFM), nanoindentation, Rutherford backscattering spectrometry (RBS), elastic recoil detection (ERD) and scanning electron microscopy (SEM).

5.1.1 Acid Catalyzed Sol-gel Films

1. The surface of all heat treated and ion irradiated films was characterized by AFM and SEM. The films heat treated in vacuum or in Ar exhibit crack-free surfaces up to a temperature of 1100 °C above which numerous bubbles, resulting from the chemical interaction between the silica film and the silicon substrate, were observed. Irradiation with 200 keV H^+, 400 keV N^{2+}, 1 MeV Cu^+, 4 MeV Cu^{2+} and 9 MeV Cu^{3+} with fluences of 1×10^{13} to 2×10^{17} ions/cm^2 did not increase the surface roughness. However, surface buckling was observed on films irradiated with a fluence of 1×10^{17} ions/cm^2 or above after being stored in the laboratory at room temperature for about one month. The buckling defects are attributed to the high residual compressive stress resulting from the ion irradiation.

2. The effects of heat treatment on the acid catalyzed films were studied. The theoretical chemical composition was obtained based on the starting materials and the involved chemical reactions. The theoretical composition of the green film $SiO(OC_2H_5)_{1.4}(CH_3)_{0.6}$ is in good agreement with the chemical composition obtained from RBS and ERD. The difference in the mechanical properties of the films heat treated in ambient air and in vacuum is attributed to the different thermal stability and decomposition path of the organic components in different environments, thus affecting the resultant change of the microstructure. The related peak change with increasing temperature in the FT-IR and Raman spectra is consistent with the change in the measured mechanical properties [90]. No crystalline phase was detected at a temperature 1100 °C or below. In contrast to the forming of silicon oxycarbide ceramic at 800 - 1000 °C reported in the literature, the film heat treated at 1100 °C in Ar exhibits mechanical properties of amorphous silica.

3. The effects of ion irradiation on the acid catalyzed films was systematically investigated. Ion irradiation was performed with 200 keV H^+, 400 keV N^{2+}, 1 MeV Cu^+, 4 MeV Cu^{2+} and 9 MeV Cu^{3+} with fluences of 1×10^{13} to 2×10^{17} ions/cm^2. The resulting changes in the film shrinkage, and the hardness and reduced elastic modulus were measured and analyzed. The significance of the fluence was observed as follows. At a fluence of 1×10^{13} ions/cm^2, there was almost no change in the shrinkage and mechanical properties compared with the green films. At a fluence of 1×10^{14} ions/cm^2, there was a wide distribution of film shrinkage from 7% to 51%, while there was a minor change in the mechanical properties. Film irradiated with 9 MeV Cu^{3+} at a fluence of 1×10^{14} ions/cm^2 had a film shrinkage of 51% and a hardness of 1.2 GPa compared with 0.3 GPa for the green film. At higher fluences, the increase in the mechanical properties was strongly associated with film shrinkage. For example, with increasing fluence from 1×10^{14} to 1×10^{15} ions/cm^2, irradiation with 9 MeV Cu^{3+} resulted in an increase of film shrinkage from 51% to 77% and an increase of $\sim$11 GPa in measured hardness and $\sim$123 GPa in reduced elastic modulus.

4. Analyzing the chemical composition of the ion irradiated films has shown that not only H, but also O and C, were released during irradiation. The ratio of H/Si approaches a constant of $\sim$0.14 with 4 MeV Cu^{2+} at a fluence of 1×10^{16} ions/cm^2 and 9 MeV Cu^{3+} at a fluence of 1×10^{15} ions/cm^2 or above, while the ratio for the other ion irradiations shows a continuous decrease with increasing fluence towards the final value. This indicates that the final H concentration may be solely dependent on the chemical nature of the films.

5. The films irradiated with 1 MeV Cu^+ (electronic stopping of 35.3 eV/Å-ion, nuclear stopping of 30.8 eV/Å-ion) exhibited a higher hardness and reduce elastic modulus than the films irradiated with 400 keV N^{2+} (electronic stopping of 25.5 eV/Å-ion, nuclear stopping of 2.0 eV/Å-ion) for a given fluence. The difference in the hardness and reduced elastic modulus became significant at higher fluences. At a fluence of 1×10^{15} ions/cm^2, the film irradiated with 1 MeV Cu^+ had a hardness of 6.2 GPa and reduced elastic modulus of 69.1 GPa which are approximately twice the values for the film irradiated with 400 keV N^{2+}. This suggests that both electronic stopping and nuclear stopping contribute to the improvements of the mechanical properties.

6. The Voigt and Reuss model has been employed to evaluate the reduced elastic modulus of the fully converted films through ion irradiation by considering them as a composite. It has been used in pyrolyzed silicon oxycarbide glass by decomposing the chemical composition into xSiC + $(1-x)$$SiO_2$ + yC. Therefore the elastic modulus is estimated from the volume fraction of amorphous SiC, amorphous silica and excess free carbon. Following the same procedure, the reduced elastic moduli of the ion irradiated films were calculated and are in good agreement with the experimental results, suggesting it is valid to apply this model to estimate the elastic modulus from the chemical composition in the ion irradiated sol-gel films. The reduced elastic modulus of the fully converted films after ion irradiation increased with increasing Si-C bond concentration, consistent with that of the silicon oxycarbide synthesized by heat treatment in Ar flow or by RF sputtering.

7. Oxygen release might be related with both the Si-O-Si network and Si-O-C_2H_5, in which the latter is assumed to be more favorable. The amount of O released after ion irradiation at the highest fluence is consistent with the total stopping power of the ions used in the irradiation. This suggests that cleavage of Si-O in Si-O-C_2H_5 is highly dependent on the stopping power of the incident ions.

8. Tetrahedrally coordinated CSi_4 units in the stoichiometric silicon oxycarbide were considered to improve mechanical properties, such as elastic modulus, hardness as well as density, viscosity and glass transition temperature, compared to fused silica. The mechanism of forming CSi_4 during ion irradiation can be described by two schemes, of which scheme (a), the construction of CSi_4 units by cleavage of three C-H bonds in Si-CH_3 and three Si-O bonds in Si-O-C_2H_5, seems more likely if only considering the localized density of Si-O-C_2H_5 and Si-CH_3 groups.

5.1.2 Base Catalyzed Sol-gel Films

Base catalyzed sol-gel system was chosen to compare the effects of the type of the sol-gel system on the mechanical and chemical properties after heat treatment and ion irradiation. The base catalyzed films showed higher surface roughness than the acid catalyzed films in their green state (3 nm Rq compared to 1 nm Rq over a scan size of 1 μm $\times$ 1 μm measured by AFM). Unlike the acid catalyzed films showing a monotonic increased in the hardness and reduced elastic modulus with increasing heat treatment temperature ranging from 300 °C to 800 °C in air, the base catalyzed films had a maximum hardness when heat treated at 600 °C and above. The base catalyzed films heat treated at 1100 °C or above in Ar contained cracks while the acid catalyzed films at 1100 °C were still crack-free.

5.2 Future Work

- To better understand the microstructure of the films irradiated with 1 MeV Cu^{+}, 4 MeV Cu^{2+} and 9 MeV Cu^{3+}, characterization of the possible crystalline phases using XRD should be performed.

- Nuclear magnetic resonance (NMR) has been widely used in determining the chemical bond configurations. Quantitative information of the change in the bond configuration may help clarify the conversion process resulting from different ions with different stopping powers. However, the difficulty to employ NMR on a thin film with less than 1 μm thick must be overcome.

- Perform post-irradiation heat treatment and analyze the possible nanophases introduced.

- In order to reduce the mismatch of the thermal expansion coefficient between the films and the substrate, thus avoiding cracking when synthesizing nanophase materials at high temperature, perform ion irradiation and post-irradiation experiments on the films deposited on fused silica wafers.

BIBLIOGRAPHY

[1] E. Brinksmeier, O. Riemer, W. Preu, F. Klocke, T. Pfeifer, M. Weck, W. Michaeli, P. Mayr, H.-R. Stock, A. Mehner, G. Goch, and D.A. Lucca. Process chains for the replication of complex optical elements. *Annals of the WGP*, XI/1:61–64, 2004.

[2] W. Datchary, A. Mehner, H.W. Zoch, D.A. Lucca, M.J. Klopfstein, R. Ghisleni, D. Grimme, and E. Brinksmeier. High precision diamond machining of hybrid sol-gel coatings. *Journal of Sol-Gel Science and Technology*, 35:245–251, 2005.

[3] J. Gallardo, P. Galliano, and A. Durn. Thermal evolution of hybrid sol-gel silica coatings: A structural analysis. *Journal of Sol-Gel Science and Technology*, 19:393–397, 2000.

[4] S. Jeong, D. Kim, S. Lee, B.-K. Park, and J. Moon. Organic-inorganic hybrid dielectrics with low leakage current for organic thin-film transistors. *Applied Physics Letters*, 89:092101, 2006.

[5] A. Mehner, H. Klumper-Westkamp, F. Hoffmann, and P. Mayr. Crystallization and residual stress formation of sol-gel-derived zirconia films. *Thin Solid Films*, 308-309:363–368, 1997.

[6] A. Mehner, W. Datchary, N. Bleil, H.W. Zoch, M.J. Klopfstein, and D.A. Lucca. The influence of processing on crack formation, microstructure, density and hardness of sol-gel derived zirconia films. *Journal of Sol-Gel Science and Technology*, 36:25–32, 2005.

[7] J.C. Pivin and P. Colombo. Ceramic coatings by ion irradiation of polycarbosilanes and polysiloxanes. Part I Conversion Mechanism. *Journal of Materials Science*, 32:6163–6173, 1997.

[8] J.C. Pivin and P. Colombo. Ceramic coatings by ion irradiation of polycarbosilanes and polysiloxanes. Part II Hardness and Thermochemical Stability. *Journal of Materials Science*, 32:6175–6182, 1997.

[9] D.A. Lucca, R. Ghisleni, J.-K. Lee, Y.Q. Wang, M. Nastasi, J. Dong, and A. Mehner. Effects of ion irradiation on the structural transformation of sol-gel derived TEOS/MTES thin films. *Nuclear Instruments and Methods in Physics Research B*, 266:2457–2460, 2008.

[10] R. Ghisleni, D.A. Lucca, J.-K. Lee Y.Q. Wang, M. Nastasi, J. Dong, and A. Mehner. Ion irradiation effects on surface mechanical behavior and shrinkage of hybrid sol-gel derived silicate thin films. *Nuclear Instruments and Methods in Physics Research B*, 266:2453–2456, 2008.

[11] D.A. Lucca, Y. Qi, T.A. Harriman, T. Prenzel, Y.Q. Wang, M. Nastasi, J. Dong, and A. Mehner. Effects of ion irradiation on the mechanical properties of $SiNa_wO_xC_yH_z$ sol-gel derived thin films. *Nuclear Instruments and Methods in Physics Research B*, 268:2926–2929, 2010.

[12] Y. Qi, T. Prenzel, T.A. Harriman, Y.Q. Wang, D.A. Lucca, D. Williams, M. Nastasi, J. Dong, and A. Mehner. Investigation of hydrogen concentration and hardness of ion irradiated organically modified silicate thin films. *Nuclear Instruments and Methods in Physics Research B*, 268:1997–2000, 2010.

[13] V.K. Mittal, S. Lotha, and D.K. Avasthi. Hydrogen loss under heavy ion irradiation in polymers. *Radiation Effects and Defects in Solids*, 147:199–209, 1999.

[14] S.K. Srivastavaa, D.K. Avasthia, and J.C. Pivin. Mechanism of H release from Si-based polymers under ion irradiation. *Nuclear Instruments and Methods in Physics Research B*, 191:718–722, 2002.

[15] D.L. Baptista, I.T.S. Garcia, and F.C. Zawislak. Loss of hydrogen from ion irradiated photoresist and a-C:H films. *Nuclear Instruments and Methods in Physics Research Section B*, 846:219–220, 2004.

[16] E.H.C. Ullersma, P. Ullersma, and F.H.P.M. Habraken. Hydrogen loss in a-Si:C:H layers induced by MeV ion beam irradiation. *Physical Review B*, 61:10133–10141, 2000.

[17] R. Ghisleni. *Effects of ion irradiation on the surface mechanical behavior of hybrid sol–gel derived silicate thin films*. PhD thesis, Oklahoma State University, Stillwater OK, May 2007.

[18] C.J. Brinker and G.W. Scherer. *Sol-gel Science: The Physics and Chemistry of Sol-gel Processing*. Academic Press, 1st edition, 1990.

[19] L.L. Hench and J.K. West. The sol-gel process. *Chemical Reviews*, 90:33–72, 1990.

[20] H. Dislich and P. Hinz. History and principles of the sol-gel process, and some new multicomponent oxide coatings. *Journal of Non-Crystalline Solids*, 48:11–16, 1982.

[21] P. Anderson and L.C. Klein. Shrinkage of lithium aluminosilicate gels during drying. *Journal of Non-Crystalline Solids*, 93:415–422, 1987.

[22] G. Hass, M.H. Francombe, and R.W. Hoffman. *Physics of Thin Films: Advances in Research and Development*. Elsevier, 2013.

[23] I. Strawbridge and P.F. James. Thin silica films prepared by dip coating. *Journal of Non-Crystalline Solids*, 82:366–372, 1986.

[24] I. Strawbridge and P.F. James. The factors affecting the thickness of sol-gel derived silica coatings prepared by dipping. *Journal of Non-Crystalline Solids*, 86:381–393, 1986.

[25] B.E. Yoldas. Zirconium oxides formed by hydrolytic condensation of alkoxides and parameters that affect their morphology. *Journal of Materials Science*, 21:1080–1086, 1986.

[26] C.J. Brinker. Hydrolysis and condensation of silicates: Effects on structure. *Journal of Non-Crystalline Solids*, 100:31–50, 1988.

[27] H. Kozuka, M. Kajimura, T. Hirano, and K. Katayama. Crack-free, thick ceramic coating films via non-repetitive dip-coating using polyvinylpyrrolidone as stress-relaxing agent. *Journal of Sol-Gel Science and Technology*, 19:205–209, 2000.

[28] H. Kozuka, S. Takenaka, H. Tokita, T. Hirano, Y. Higashi, and T. Hamatani. Stress and cracks in gel-derived ceramic coatings and thick film formation. *Journal of Sol-Gel Science and Technology*, 26:681–686, 2003.

[29] C.-K. Chan, I.-M. Chu, and Y.-W. Lin. Interfacial interactions and their influence to phase behavior in poly(vinyl pyrrolidone)/silica hybrid materials prepared by sol-gel process. *Materials Letters*, 58:2243–2247, 2004.

[30] V. Subramanian, N. Ndiege, E.G. Seebauer, M.A. Shannon, and R.I. Masel. Synthesis and characterization of polyvinylpyrrolidine assisted tantalum pentoxide films. *Thin Solid Films*, 516:4784–4792, 2008.

[31] N. Ndiege, T. Wilhoite, V. Subramanian, M. Shannon, and R. Masel. Sol-gel synthesis of thick Ta_2O_5 films for photonic band gap materials. *MRS Proceedings*, 929, 2006.

[32] N. Ndiege, T. Wilhoite, V. Subramanian, M.A. Shannon, and R.I. Masel. Sol-gel synthesis of thick Ta_2O_5 films. *Chemistry of Materials*, 19:3155–3161, 2007.

[33] K. Izumi, H.Tanaka, Y. Uchida, N. Tohge, and T. Minami. Influence of firing conditions on adhesion of methyltrialkoxysilane-derived coatings on steel sheets. *Journal of Non-Crystalline Solids*, 147-148:483–487, 1992.

[34] K.S. Huang, E.C. Lee, and Y.S. Chang. Synethesis and characterization of soluble hybrids of poly(vinyl pyrrolidone) or its copolymer. *Journal of Applied Polymer Science*, 100:2164–2170, 2006.

[35] K. Kamiya, T. Yoko, K. Tanaka, and M. Takeuchi. Thermal evolution of gels derived from $CH_3Si(OC_2H_5)_3$ by the sol-gel method. *Journal of Non-Crystalline Solids*, 121:182–187, 1990.

[36] J. Gallardo, A. Duran, D. Di Martino, and R.M. Almeida. Structure of inorganic and hybrid SiO_2 sol-gel coatings studied by variable incidence infrared spectroscopy. *Journal of Non-Crystalline Solids*, 298:219–225, 2002.

[37] P. Innocenzi, M.O. Abdirashid, and M. Guglielmi. Structure and properties of sol-gel coatings from methyltriethoxysilane and tetraethoxysilane. *Journal of Sol-Gel Science and Technology*, 3:47–55, 1994.

[38] W. Li and R.J. Willey. Stability of hydroxyl and methoxy surface groups on silica aerogels. *Journal of Non-Crystalline Solids*, 212:243–249, 1997.

[39] Y. Liu, W. Ren, L. Zhang, and X. Yao. New method for making porous SiO_2 thin films. *Thin Solid Films*, 353:124–128, 1999.

[40] Y.K. Du, P. Yang, Z.G. Mou, N.P. Hua, and L. Jiang. Thermal decomposition behaviors of PVP coated on platinum nanoparticles. *Journal of Applied Polymer Science*, 99:23–26, 2006.

[41] Y. Borodko, S.E. Habas, M. Koebel, P. Yang, H. Frei, and G.A. Somorjai. Probing the interaction of poly (vinylpyrrolidone) with platinum nanocrystals by UV-Raman and FTIR. *The Journal of Physical Chemistry B*, 110:23052–23059, 2006.

[42] T. Kishimoto and H. Kozuka. Sol-gel preparation of TiO_2 ceramic coating films from aqueous solutions of titanium sulfate (IV) containing polyvinylpyrrolidone. *Journal of Materials Research*, 18:466–474, 2003.

[43] G.D. Sorarù, S. Modena, E. Guadagnino, P. Colombo, J. Egan, and C. Pantano. Chemical durability of silicon oxycarbide glasses. *Journal of the American Ceramic Society*, 85:1529–1536, 2002.

[44] S. Walter, G.D. Soraru, H. Brequel, and S. Enzo. Microstructural and mechanical characterization of sol gel-derived Si-O-C glasses. *Journal of the European Ceramic Society*, 22:2389–2400, 2002.

[45] P.H. Mutin. Control of the composition and structure of silicon oxycarbide and oxynitride glasses derived from polysiloxane precursors. *Journal of Sol-Gel Science and Technology*, 14:27–38, 1999.

[46] E. Radovanovic, M.F. Gozzi, M.C. Gonçalves, and I.V.P. Yoshida. Silicon oxycarbide glasses from silicone networks. *Journal of Non-Crystalline Solids*, 248:37–48, 1999.

[47] R. Riedel, G. Mera, R. Hauser, and A. Klonczynski. Silicon-based polymer-derived ceramics: Synthesis properties and applications - A review dedicated to Prof. Dr. Fritz Aldinger on the occasion of his 65th birthday. *Journal of the Ceramic Society of Japan*, 114:425–444, 2006.

[48] C. Turquat, H.-J. Kleebe, G. Gregori, S. Walter, and G.D. Sorarù. Transmission electron microscopy and electron energy–loss spectroscopy study of nonstoichiometric silicon–carbon–oxygen glasses. *Journal of the American Ceramic Society*, 84:2189–2196, 2001.

[49] J. Brus, F. Kolář, V. Machovič, and J. Svıtilová. Structure of silicon oxycarbide glasses derived from poly (methylsiloxane) and poly [methyl (phenyl) siloxane] precursors. *Journal of Non-Crystalline Solids*, 289:62–74, 2001.

[50] G.D. Sorarù, G. D'andrea, R. Campostrini, F. Babonneau, and G. Mariotto. Structural characterization and high-temperature behavior of silicon oxycarbide glasses prepared from sol-gel precursors containing Si-H bonds. *Journal of the American Ceramic Society*, 78:379–387, 1995.

[51] C.G. Pantano, A.K. Singh, and H. Zhang. Silicon oxycarbide glasses. *Journal of Sol-Gel Science and Technology*, 14:7–25, 1999.

[52] G.M. Renlund, S. Prochazka, and R.H. Doremus. Silicon oxycarbide glasses: Part II. Structure and Properties. *Journal of Materials Research*, 6:2723–2734, 1991.

[53] J. Latournerie, P. Dempsey, D. Hourlier-Bahloul, and J.-P. Bonnet. Silicon oxycarbide glasses: Part 1 - Thermochemical Stability. *Journal of the American Ceramic Society*, 89:1485–1491, 2006.

[54] G.D. Sorarù. Silicon oxycarbide glasses from gels. *Journal of Sol-Gel Science and Technology*, 2:843–848, 1994.

[55] H.-J. Kleebe, C. Turquat, and G.D. Sorarù. Phase separation in an SiCO glass studied by transmission electron microscopy and electron energy-loss spectroscopy. *Journal of the American Ceramic Society*, 84:1073–1080, 2001.

[56] E. Breval, M. Hammond, and C.G. Pantano. Nanostructural characterization of silicon oxycarbide glasses and glass-ceramics. *Journal of the American Ceramic Society*, 77:3012–3018, 1994.

[57] F.W. DelRio, M.L. Dunn, and M.P. de Boer. Growth of silicon carbide nanoparticles using tetraethylorthosilicate for microelectromechanical systems. *Electrochemical and Solid-State Letters*, 10:H27–H30, 2007.

[58] T. Venkatesan. High energy ion beam modification of polymer films. *Nuclear Instruments and Methods in Physics Research B*, 7/8:461–467, 1985.

[59] S.K. Srivastava, D.K. Avasthi, and J.C. Pivin. Mechanism of H release from Si-based polymers under ion irradiation. *Nuclear Instruments and Methods in Physics Research B*, 191:718–722, 2002.

[60] J.C. Pivin, P. Colombo, A. Martucci, G.D. Soraru, E. Pippel, and M. Sendova-Vassileva. Ion beam induced conversion of Si-based polymers and gels layers into ceramics coatings. *Journal of Sol-Gel Science and Technology*, 26:251–255, 2003.

[61] M.N. Rahamn. *Ceramic Processing and Sintering*. CRC Press, 2nd edition, 2003.

[62] J.C. Pivin, P. Colombo, M. Sendova-Vassileva, J. Salomon, G. Sagon, and A. Quaranta. Ion-induced conversion of polysiloxanes and polycarbosilanes into ceramics: Mechanisms and Properties. *Nuclear Instruments and Methods in Physics Research B*, 141:652–662, 1998.

[63] S. Yu, T.K.S. Wong, X. Hu, and K. Pita. The effect of TEOS/MTES ratio on the structural and dielectric properties of porous silica films. *Journal of the Electrochemical Society*, 150:F116–F121, 2003.

[64] S. Yu, T.K.S. Wong, X. Hu, and M.S. Yong. Dielectric and mechanical properties of surface modified organosilicate films. *Journal of Sol-Gel Science and Technology*, 35:69–75, 2005.

[65] A.V. Rao, P.B. Wagh, D. Haranath, P.P. Risbud, and S.D. Kumbhare. Influence of temperature on the physical properties of TEOS silica xerogels. *Ceramics International*, 25:505–509, 1999.

[66] A. Matsuda, Y. Matsuno, M. Tatsumisago, and T. Minami. Fine patterning and characterization of gel films derived from methyltriethoxysilane and tetraethoxysilane. *Journal of American Ceramic Society*, 81:2849–2852, 1998.

[67] G.D. Sorarù, E. Dallapiccola, and G. D'Andrea. Mechanical characterization of sol–gel-derived silicon oxycarbide glasses. *Journal of the American Ceramic Society*, 79:2074–2080, 1996.

[68] J.C. Pivin, P. Colombo, and G.D. Soraru. Comparison of ion irradiation effects in silicon-based preceramic thin films. *Journal of American Ceramic Society*, 83:713–720, 2000.

[69] J.C. Pivin and P. Colombo. Conversion of organic-inorganic polymers to ceramics by ion implantation. *Nuclear Instruments and Methods in Physics Research B*, 120:262–265, 1996.

[70] J.C. Pivin, P. Viel, G. Zalczer, and G. Marletta. Effects of ionizations and displacements on the hardness and optical absorption of some ion irradiated polymers. *Nuclear Instruments and Methods in Physics Research B*, 105:192–196, 1995.

[71] J.C. Pivin. Contribution of ionizations and atomic displacements to the hardening of ion-irradiated polymers. *Thin Solid Films*, 263:185–193, 1995.

[72] J.C. Pivin. Formation of nanostructures with a controlled size distribution in Si-based gels by ion irradiation. *Materials Science-Poland*, 23:101–109, 2005.

[73] D. Wang and G.P. Bierwagen. Sol-gel coatings on metals for corrosion protection. *Progress in Organic Coatings*, 64:327–338, 2009.

[74] A. Conde, J. De Damborenea, A. Durn, and M. Menning. Protective properties of a sol-gel coating on zinc coated steel. *Journal of Sol-Gel Science and Technology*, 37:79–85, 2006.

[75] M. Menning, C. Schelle, A. Duran, J.J. Damborena, M. Guglielmi, and G. Brusatin. Investigation of glass-like sol-gel coatings for corrosion protection of stainless steel against liquid and gaseous attack. *Journal of Sol-Gel Science and Technology*, 13:717–722, 1998.

[76] J. Liu, G. Gong, and C. Yan. Enhancement of the erosion-corrosion resistance of dacromet with hybrid SiO_2 sol-gel. *Surface and Coatings Technology*, 200:4967–4975, 2006.

[77] K.-H. Haas, S. Amberg-Schwab, K. Rose, and G. Schottner. Functionalized coatings based on inorganic-organic polymers (ormocer®s) and their combination with vapor deposited inorganic thin films. *Surface and Coatings Technology*, 111:72–79, 1999.

[78] C. Li, K. Jordens, and G.L. Wilkes. Abrasion-resistant coatings for plastic and soft metallic substrates by sol-gel reactions of a triethoxysilylated diethylenetriamine and tetramethoxysilane. *Wear*, 242:152–159, 2000.

[79] J.M. Urreaga, M.C. Matas, V.L., and M.U. de la Orden. Abrasion resistance in the tumble test of sol-gel hybrid coatings for ophthalmic plastic lenses. *Materials Letters*, 45:293–297, 2000.

[80] J. Wang. Sol-gel materials for electrochemical biosensors. *Analytica Chimica Acta*, 399:21–27, 1999.

[81] J. Shen, X. Yang, Y. Zhu, H. Kang, H. Cao, and C. Li. Gold-coated silica-fiber hybrid materials for application in a novel hydrogen peroxide biosensor. *Biosensors and Bioelectronics*, 34:132–136, 2012.

[82] G.-H. Wang and L.-M. Zhang. Using novel polysaccharide-silica hybrid material to construct an amperometric biosensor for hydrogen peroxide. *The Journal of Physical Chemistry B*, 110:24864–24868, 2006.

[83] M. Wu, Z. Wu, R.and Zhang, and H. Zou. Preparation and application of organic-silica hybrid monolithic capillary columns. *Electrophoresis*, 32:105–115, 2011.

[84] J. Ou, H. Lin, Z. Zhang, J. Huang, G.and Dong, and H. Zou. Recent advances in preparation and application of hybrid organic-silica monolithic capillary columns. *Electrophoresis*, 34:126–140, 2013.

[85] L.C. Klein. *Sol-gel Optics: Processing and Applications*. Springer Science & Business Media, 2013.

[86] B. Lebeau and C. Sanchez. Sol-gel derived hybrid inorganic-organic nanocomposites for optics. *Current Opinion in Solid State and Materials Science*, 4:11–23, 1999.

[87] I. Fisher, W.D. Kaplan, and M. Eizenberg. Dielectric property-microstructure relationship for nanoporous silica based thin films. *Journal of Applied Physics*, 95:5762–5767, 2004.

[88] C.V. Nguyen, K.R. Carter, C.J. Hawker, J.L. Hedrick, R.L. Jaffe, R.D. Miller, J.F. Remenar, H.-W. Rhee, P.M. Rice, M.F. Toney, M. Trollss, and D.Y. Yoon. Low-dielectric, nanoporous organosilicate films prepared via inorganic/organic polymer hybrid templates. *Chemistry of Materials*, 11:3080–3085, 1999.

[89] T.-J. Ha, S.G. Choi, S.-B. Jung, B.-G. Yu, and H.-H. Park. The improvement of mechanical and dielectric properties of ordered mesoporous silica film using TEOS-MTES mixed silica precursor. *Ceramics International*, 34:947–951, 2008.

[90] T. Prenzel. Characterization of silica-based hybrid sol-gel coatings after heat treatment and ion irradiation. Diploma thesis in chemistry, University Bremen, 2009.

[91] J.F. Ziegler, M.D. Ziegler, and J.P. Biersack. SRIM - the stopping and range of ions in matter (2010). *Nuclear Instruments and Methods in Physics Research Section B*, 268:1818–1823, 2010.

[92] W.C. Oliver and G.M. Pharr. Measurement of hardness and elastic modulus by instrumented indentation: Advances in understanding and refinements to methodology. *Journal of Materials Research*, 19:3–20, 2004.

[93] W.C. Oliver and G.M. Pharr. An improved technique for determining hardness and elastic modulus using load and displacement sensing indentation experiments. *Journal of Materials Research*, 7:1564–1583, 1992.

[94] J. Menčík, D. Munz, E. Quandt, E.R. Weppelmann, and M.V. Swain. Determination of elastic modulus of thin layers using nanoindentation. *Journal of Materials Research*, 12:2475–2484, 1997.

[95] T.Y. Tsui and G.M. Pharr. Substrate effects on nanoindentation mechanical property measurement of soft films on hard substrates. *Journal of Materials Research*, 14:292–301, 1999.

[96] H. Ni and X. Li. Young's modulus of ZnO nanobelts measured using atomic force microscopy and nanoindentation techniques. *Nanotechnology*, 17:3591, 2006.

[97] G.E. Fougere, L. Riester, M. Ferber, J.R. Weertman, and R.W. Siegel. Young's modulus of nanocrystalline Fe measured by nanoindentation. *Materials Science and Engineering: A*, 204:1–6, 1995.

[98] T.S. Li, H. Li, and F. Pan. Microstructure and nanoindentation hardness of Ti/TiN multilayered films. *Surface and Coatings Technology*, 137:225–229, 2001.

[99] B. Yang, L. Riester, and T.G. Nieh. Strain hardening and recovery in a bulk metallic glass under nanoindentation. *Scripta Materialia*, 54:1277–1280, 2006.

[100] A.C. Fischer-Cripps. *Factors Affecting Nanoindentation Test Data*. Springer, 2000.

[101] D.S. Harding, W.C. Oliver, and G.M. Pharr. Cracking during nanoindentation and its use in the measurement of fracture toughness. *MRS Proceedings*, 356:663, 1994.

[102] X. Li, D. Diao, and B. Bhushan. Fracture mechanisms of thin amorphous carbon films in nanoindentation. *Acta materialia*, 45:4453–4461, 1997.

[103] V. Domnich, Y. Gogotsi, and S. Dub. Effect of phase transformations on the shape of the unloading curve in the nanoindentation of silicon. *Applied Physics Letters*, 76:2214–2216, 2000.

[104] J.-I. Jang, M.J. Lance, S. Wen, T.Y. Tsui, and G.M. Pharr. Indentation-induced phase transformations in silicon: influences of load, rate and indenter angle on the transformation behavior. *Acta Materialia*, 53:1759–1770, 2005.

[105] C.A. Tweedie and K.J. Van Vliet. Contact creep compliance of viscoelastic materials via nanoindentation. *Journal of Materials Research*, 21:1576–1589, 2006.

[106] H. Lu, B. Wang, J. Ma, G. Huang, and H. Viswanathan. Measurement of creep compliance of solid polymers by nanoindentation. *Mechanics of Time-Dependent Materials*, 7:189–207, 2003.

[107] M.L. Oyen. Analytical techniques for indentation of viscoelastic materials. *Philosophical Magazine*, 86:5625–5641, 2006.

[108] S.V. Hainsworth, H.W. Chandler, and T.F. Page. Analysis of nanoindentation load-displacement loading curves. *Journal of Materials Research*, 11, 1996.

[109] M.F. Doerner and W.D. Nix. A method for interpreting the data from depth-sensing indentation instruments. *Journal of Materials Research*, 1:601–609, 1986.

[110] J. Woirgard and J.-C. Dargenton. An alternative method for penetration depth determination in nanoindentation measurements. *Materials Research Society*, 12:2455–2458, 1997.

[111] G.M. Pharr, W.C. Oliver, and F.R. Brotzen. On the generality of the relationship among contact stiffness, contact area, and elastic modulus during indentation. *Journal of Materials Research*, 7:613–617, 1992.

[112] G.M. Pharr, E.G. Herbert, and Y. Gao. The indentation size effect: A critical examination of experimental observations and mechanistic interpretations. *Annual Review of Materials Research*, 40:271–292, 2010.

[113] M.R. VanLandingham. Review of instrumented indentation. *Journal of Research of the National Institute of Standards and Technology*, 108, 2003.

[114] W.D. Nix and H. Gao. Indentation size effects in crystalline materials: A law for strain gradient plasticity. *Journal of the Mechanics and Physics of Solids*, 46:411–425, 1998.

[115] J.G. Swadener, E.P. George, and G.M. Pharr. The correlation of the indentation size effect measured with indenters of various shapes. *Journal of the Mechanics and Physics of Solids*, 50:681–694, 2002.

[116] K.W. McElhaney, J.J. Vlassak, and W.D. Nix. Determination of indenter tip geometry and indentation contact area for depth-sensing indentation experiments. *Journal of Materials Research*, 13:1300–1306, 1998.

[117] Y. Liu and A.H.W. Ngan. Depth dependence of hardness in copper single crystals measured by nanoindentation. *Scripta Materialia*, 44:237–241, 2001.

[118] K. Sangwal. On the reverse indentation size effect and microhardness measurement of solids. *Materials Chemistry and Physics*, 63:145–152, 2000.

[119] Q. Ma and D.R. Clarke. Size dependent hardness of silver single crystals. *Journal of Materials Research*, 10:853–863, 1995.

[120] J.L. Hay, M.E. O'Hern, and W.C. Oliver. The importance of contact radius for substrate-independent property measurement of thin films. *MRS Proceedings*, 522:27, 1998.

[121] M.F. Doerner and W.D. Nix. A method for interpreting the data from depth-sensing indentation instruments. *Journal of Materials Research*, 1:601–609, 1986.

[122] R.B. King. Elastic analysis of some punch problems for a layered medium. *International Journal of Solids and Structures*, 23:1657–1664, 1987.

[123] H. Gao, C. Chiu, and J. Lee. Elastic contact versus indentation modeling of multi-layered materials. *International Journal of Solids and Structures*, 29:2471–2492, 1992.

[124] X. Chen and J.J. Vlassak. Numerical study on the measurement of thin film mechanical properties by means of nanoindentation. *Journal of Materials Research*, 16:2974–2982, 2001.

[125] R. Saha and W.D. Nix. Effects of the substrate on the determination of thin film mechanical properties by nanoindentation. *Acta Materialia*, 50:23–38, 2002.

[126] J.H. Westbrook and H. Conrad. *The Science of Hardness Testing and Its Research Applications*. American Society for Metals, 1973.

[127] B. Jonsson and S. Hogmark. Hardness measurements of thin films. *Thin Solid Films*, 114:257–269, 1984.

[128] P.J. Burnett and D.S. Rickerby. The mechanical properties of wear-resistant coatings: I: Modelling of hardness behaviour. *Thin Solid Films*, 148:41–50, 1987.

[129] A.C. Fischer-Cripps. *Nanoindentation*. Springer, 2011.

[130] G. Friedbacher and H. Bubert. *Surface and Thin Film Analysis: A Compendium of Principles, Instrumentation, and Applications*. Wiley, 2011.

[131] M. Bozoian, K.M. Hubbard, and M. Nastasi. Deviations from Rutherford-scattering cross sections. *Nuclear Instruments and Methods in Physics Research Section B*, 51:311–319, 1990.

[132] M. Bozoian. Thresholds of non-Rutherford nuclear cross sections for ion beam analysis. *Nuclear Instruments and Methods in Physics Research Section B*, 56-57:740–43, 1991.

[133] K.M. Hubbard, J.R. Tesmer, M. Nastasi, and M. Bozoian. Measured deviations from Rutherford backscattering cross sections using Li-ion beams. *Nuclear Instruments and Methods in Physics Research Section B*, 58:121–126, 1991.

[134] M. Nastasi. *Ion-Solid Interactions: Fundamentals and Applications*. Cambridge University Press, 1996.

[135] W.H. Bragg and W L. Bragg. The reflection of X-rays by crystals. *Proceedings of the Royal Society of London. Series A, Containing Papers of a Mathematical and Physical Character*, 88:428–438, 1913.

[136] S.-H. Jen, S.M. George, R.S. McLean, and P.F. Carcia. Alucone interlayers to minimize stress caused by thermal expansion mismatch between Al_2O_3 films and teflon substrates. *ACS Applied Materials & Interfaces*, 5:1165–1173, 2013.

[137] M.-W. Moon, E.-K. Her, K.H. Oh, K.-R. Lee, and A. Vaziri. Sculpting on polymers using focused ion beam. *Surface and Coatings Technology*, 202:5319–5324, 2008.

[138] Y.-R. Kim, P. Chen, M.J. Aziz, D. Branton, and J.J. Vlassak. Focused ion beam induced deflections of freestanding thin films. *Journal of Applied Physics*, 100:104322, 2006.

[139] L. Bois, J. Maquet, F. Babonneau, H. Mutin, and D. Bahloul. Structural characterization of sol-gel derived oxycarbide glasses. 1. Study of the pyrolysis process. *Chemistry of Materials*, 6:796–802, 1994.

[140] P. Innocenzi. Infrared spectroscopy of sol–gel derived silica-based films: A spectra–microstructure overview. *Journal of Non-Crystalline Solids*, 316:309–319, 2003.

[141] R.M. Almeida and C.G. Pantano. Structural investigation of silica gel films by infrared spectroscopy. *Journal of Applied Physics*, 68:4225–4232, 1990.

[142] H. Yoshino, K. Kamiya, and H. Nasu. IR study on the structural evolution of sol-gel derived SiO_2 gels in the early stage of conversion to glasses. *Journal of Non-Crystalline Solids*, 126:68–78, 1990.

[143] M. Mayer. SIMNRA, a simulation program for the analysis of NRA, RBS and ERDA. *American Institute of Physics Conference Proceedings*, 475:541–544, 1999.

[144] A. Gurbich. IBANDL (the Ion Beam Analysis Nuclear Data Library). https://www-nds.iaea.org/exfor/ibandl.htm, 2015.

[145] T. Gerhard, W. Faschinger, and G. Landwehr. Depth-sensitive X-ray diffraction using extremely asymmetrical reflections by variation of the wavelength. *Semiconductor Science and Technology*, 13:583589, 1998.

[146] S. A. Shojaee. Ph.D. dissertation in progress, Oklahoma State University, Stillwater OK, In preparation.

[147] M. Hopcroft, W.D. Nix, and T.W. Kenny. What is the Young's modulus of silicon? *Journal of Microelectromechanical Systems*, 19:229–238, 2010.

[148] C.H.M. Maree, A.M. Vredenberg, and F.H.P.M. Habraken. Mechanism of MeV ion induced hydrogen depletion from organic layers. *Materials Chemistry and Physics*, 46:198–205, 1996.

[149] M.E. Adel, O. Amir, and R. Kalish. Ion-beam-induced hydrogen release from a-C:H: A bulk molecular recombination model. *Journal of Applied Physics*, 66:3248–3251, 1989.

[150] M.P. De Jong, A.J.H. Maas, L.J. Van Ijzendoorn, S.S. Klein, and M.J.A. De Voigt. A model for ion-irradiation induced hydrogen loss from organic materials. *Journal of Applied Physics*, 82:1058–1064, 1997.

[151] V. Picq, J.M. Ramillon, and E. Balanzat. Swift heavy ions on polymers: Hydrocarbon gas release. *Nuclear Instruments and Methods in Physics Research Section B*, 146:496–503, 1998.

[152] H. Dong and T. Bell. State-of-the-art overview: ion beam surface modification of polymers towards improving tribological properties. *Surface and Coatings Technology*, 111:29–40, 1999.

[153] E.H. Lee, G.R. Rao, and L.K. Mansur. LET effect on cross-linking and scission mechanisms of PMMA during irradiation. *Radiation Physics and Chemistry*, 55:293–305, 1999.

[154] Eal H. Lee. Ion-beam modification of polymeric materials – fundamental principles and applications. *Nuclear Instruments and Methods in Physics Research Section B: Beam Interactions with Materials and Atoms*, 151:29–41, 1999.

[155] G.R. Rao, E.H. Lee, R. Bhattacharya, and A.W. McCormick. Improved wear properties of high energy ion-implanted polycarbonate. *Journal of Materials Research*, 10:190–201, 1995.

[156] E.H. Lee, G.R. Rao, M.B. Lewis, and L.K. Mansur. Effects of electronic and recoil processes in polymers during ion implantation. *Journal of Materials Research*, 9:1043–1050, 1994.

[157] Z. Hashin and S. Shtrikman. A variational approach to the theory of the elastic behaviour of polycrystals. *Journal of the Mechanics and Physics of Solids*, 10:343–352, 1962.

[158] P. Vashishta, R.K. Kalia, A. Nakano, and J.P. Rino. Interaction potential for silicon carbide: A molecular dynamics study of elastic constants and vibrational density of states for crystalline and amorphous silicon carbide. *Journal of Applied Physics*, 101:103515, 2007.

[159] V.I. Ivashchenko, P.E.A. Turchi, and V.I. Shevchenko. Simulations of the mechanical properties of crystalline, nanocrystalline, and amorphous SiC and Si. *Physical Review B*, 75:085209, 2007.

[160] M.A. E.l. Khakani, M. Chaker, A. Jean, S. Boily, J.C. Kieffer, M.E. O'hern, M.F. Ravet, and F. Rousseaux. Hardness and Young's modulus of amorphous a-SiC thin films determined by nanoindentation and bulge tests. *Journal of Materials Research*, 9:96–103, 1994.

[161] P. Du, I-K. Lin, Y. Yan, and X. Zhang. Residual stress in sputtered silicon oxycarbide thin films. *MRS Proceedings*, 1299:10, 2011.

[162] S.J. Widgeon, S. Sen, G. Mera, E. Ionescu, R. Riedel, and A. Navrotsky. ^{29}Si and ^{13}C solid-state NMR spectroscopic study of nanometer-scale structure and mass fractal characteristics of amorphous polymer derived silicon oxycarbide ceramics. *Chemistry of Materials*, 22:6221–6228, 2010.

[163] H. Bréquel, J. Parmentier, S. Walter, R. Badheka, G. Trimmel, S. Masse, J. Latournerie, P. Dempsey, C. Turquat, and A. Desmartin-Chomel. Systematic structural characterization of the high-temperature behavior of nearly stoichiometric silicon oxycarbide glasses. *Chemistry of Materials*, 16:2585–2598, 2004.

[164] G.D. Sorarù, Q. Liu, L.V. Interrante, and T. Apple. Role of precursor molecular structure on the microstructure and high temperature stability of silicon oxycarbide glasses derived from methylene-bridged polycarbosilanes. *Chemistry of Materials*, 10:4047–4054, 1998.

Appendix A

MOLECULAR STRUCTURES

A.1 TEOS

Name: Tetraethylorthosilane or Tetraethoxysilane

CAS number: 78-10-4

Formula: $Si(OC_2H_5)_4$

Structure: Figure A.1

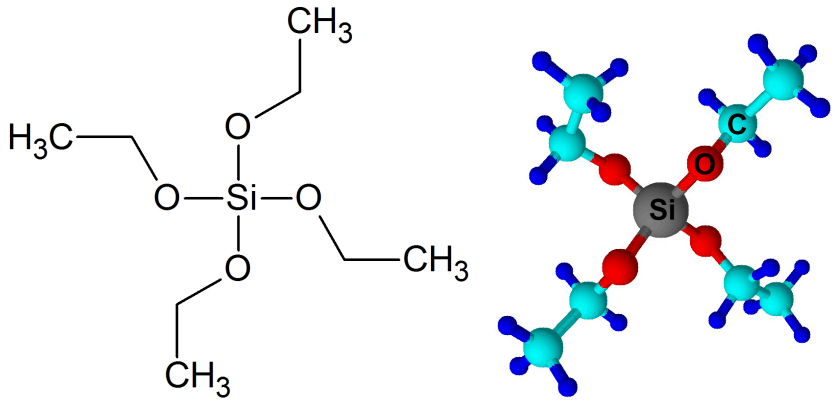

Figure A.1: TEOS (Tetraethylorthosilane or Tetraethoxysilane) molecular structure.

A.2 MTES

Name: Methyltriethoxysilane

CAS number: 2031-67-6

Formula: $(CH_3)Si(OC_2H_5)_3$

Structure: Figure A.2

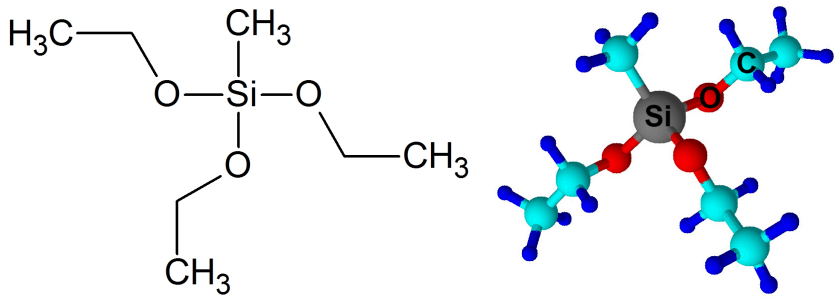

Figure A.2: MTES (Methyltriethoxysilane) molecular structure.

A.3 PVP

Name: Polyvinylpyrrolidone

CAS number: 9003-39-8

Formula: $(C_6H_9NO)_n$

Structure: Figure A.3

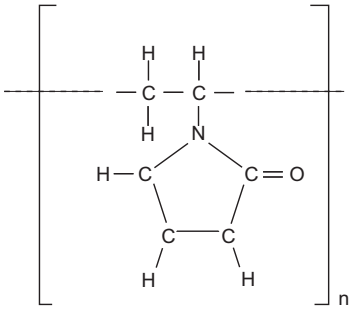

Figure A.3: PVP (Polyvinylpyrrolidone) molecular structure.

Appendix B

DIFFERENTIAL SCATTERING CROSS SECTION

B.1 ^{28}Si(α, α)Si^{28}

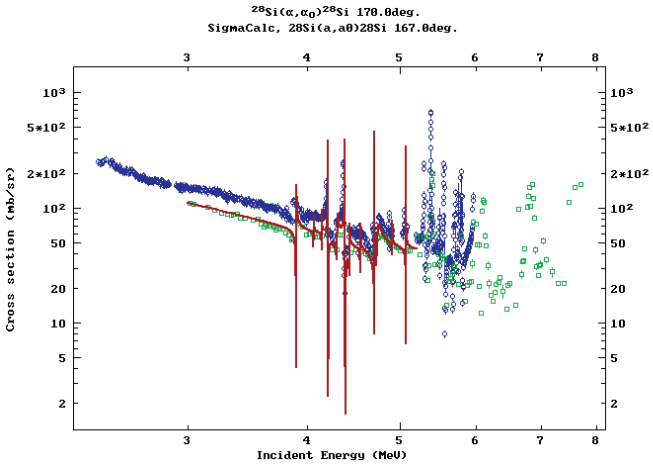

Figure B.1: Differential Scattering Cross Section of ^{28}Si(α, α)Si^{28}.

B.2 $^{16}\mathbf{O}(\alpha, \alpha)\mathbf{O}^{16}$

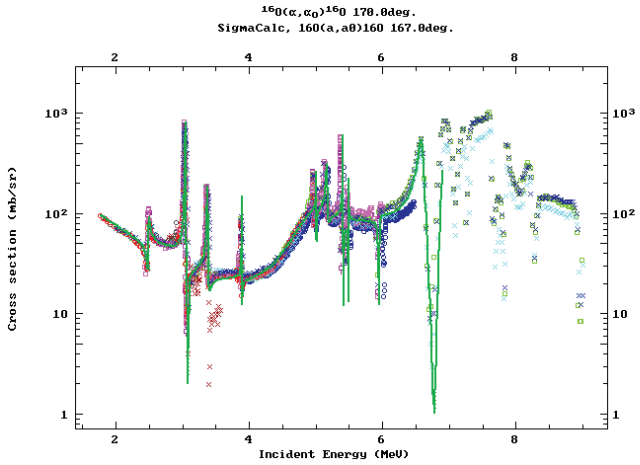

Figure B.2: Differential Scattering Cross Section of $^{16}\mathrm{O}(\alpha, \alpha)\mathrm{O}^{16}$.

B.3 $^{14}\mathbf{N}(\alpha, \alpha)\mathbf{N}^{14}$

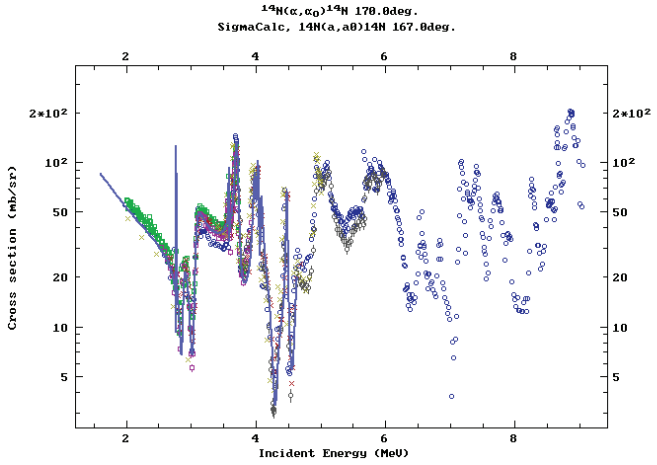

Figure B.3: Differential Scattering Cross Section of $^{14}\mathrm{N}(\alpha, \alpha)\mathrm{N}^{14}$.

B.4 $^{12}C(\alpha, \alpha)C^{12}$

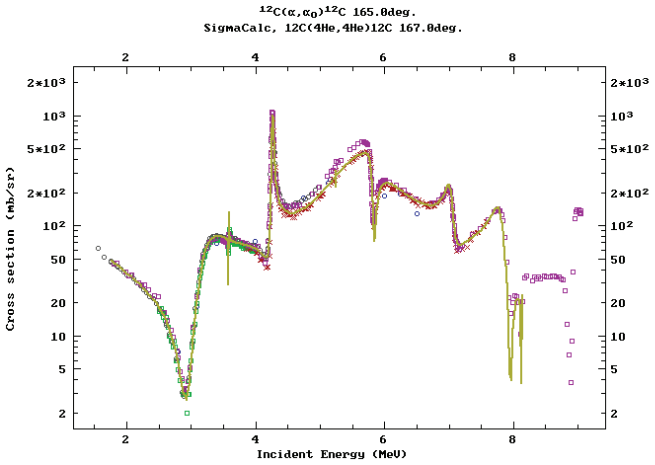

Figure B.4: Differential Scattering Cross Section of $^{12}C(\alpha, \alpha)C^{12}$.

VITA

Yongli Qi

Candidate for the Degree of

Doctor of Philosophy

Thesis: EFFECTS OF ION IRRADIATION ON THE MECHANICAL PROPERTIES AND STRUCTURAL EVOLUTION OF SOL-GEL DERIVED HYBRID SILICATE THIN FILMS

Major Field: Mechanical and Aerospacing Engineering

Biographical:

Personal Data: Born in Shouguang, China on September 23, 1982, the son of Yurong Qi and Hanzhen Gao

Education: Graduated from Shouguang First High School, Shouguang, China in June 2001; Bachelor of Science in Precision Engineering, Tianjin, China in June 2005; Master of Science in Precision Engineering, Tianjin, China in June 2007. Completed the requirements for the Doctor of Philosophy degree with a major in Mechanical Engineering at Oklahoma State University in July, 2015.

Experience: Employed by Oklahoma State University, Stillwater, Department of Mechanical and Aerospace Engineering as graduate research assistant - 2008 to present.

Professional Memberships: Student member of the American Society of Mechanical Engineers.